

# A winter study case, comparing snowfall observations with the operational forecast model MEPS

Franziska Hellmuth



Thesis submitted for the degree of  
Master in Meteorology  
60 credits

Department of Geoscience  
Faculty of Mathematics and Natural Sciences

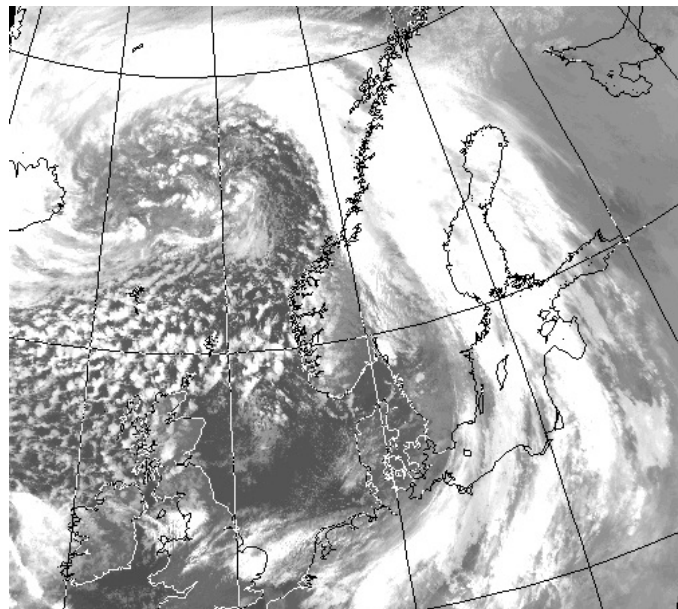
UNIVERSITY OF OSLO

Spring 2018



# **A winter study case, comparing snowfall observations with the operational forecast model MEPS**

Franziska Hellmuth



Satellite image of the extreme extratropical cyclone on 24 December 2016 at the coast of Norway. Image obtained from the Dundee Satellite Receiving Station <http://www.sat.dundee.ac.uk>.

© 2018 Franziska Hellmuth

A winter study case, comparing snowfall observations with the operational forecast model  
MEPS

<http://www.duo.uio.no/>

Printed: Reprocentralen, University of Oslo

## ABSTRACT

This abstract needs to be updated.



# TABLE OF CONTENTS

<b>LIST OF ABBREVIATIONS</b>	<b>III</b>
<b>CHAPTER 1: INTRODUCTION</b>	<b>1</b>
1.1 Background . . . . .	4
<b>CHAPTER 2: SITE, INSTRUMENTATION, DATA, AND METHODOLOGY</b>	<b>8</b>
2.1 Haukeliseter site . . . . .	8
2.2 Climate at Haukeliseter . . . . .	10
2.3 Instruments . . . . .	11
2.3.1 Double Fence Snow gauge . . . . .	13
2.3.2 MRR - Micro Rain Radar . . . . .	15
2.3.3 PIP - Precipitation Imaging Package . . . . .	17
2.3.4 MASC - Multi-Angular Snowfall Camera . . . . .	18
2.4 Optimal Estimation Retrieval Algorithm . . . . .	18
2.4.1 Snowfall retrieval scheme . . . . .	18
2.4.2 Environmental masks for the optimal estimation retrieval . . . . .	22
2.5 Operational weather forecast model - MEPS . . . . .	24
2.5.1 MetCoOP Ensemble Prediction System - MEPS . . . . .	24
2.5.2 Meso-NH and the ICE3 scheme . . . . .	26
2.5.3 Adjustment of ICE3 inside AROME-MetCoOp . . . . .	29
2.6 Numerical data transformation . . . . .	29
2.6.1 Layer thickness in MEPS . . . . .	29
2.6.2 Snow water content . . . . .	30
2.6.3 Snow water path . . . . .	31
2.6.4 Ensemble mean and Coefficient of Variation . . . . .	31
2.6.5 Mean error and mean absolute error . . . . .	32
2.6.6 Percent difference and average difference . . . . .	32

<b>I Results and Discussion</b>	<b>33</b>
<b>CHAPTER 3: ANALYSIS OF THE CHRISTMAS STORM 2016</b>	<b>34</b>
3.1 Extreme weather . . . . .	35
3.2 Dynamic Tropopause map . . . . .	36
3.3 Thickness, Sea Level Pressure, Total Precipitable Water, and wind at 250 hPa	38
3.4 Integrated Vapour Transport . . . . .	38
3.5 Observations at the weather mast . . . . .	41
3.6 Large scale circulation . . . . .	42
<b>CHAPTER 4: HAUKELISETER: OBSERVATION AND MEPS COMPARISON</b>	<b>51</b>
4.1 Meteorological Investigation of the Christmas storm 2016 . . . . .	52
4.1.1 Surface comparison . . . . .	52
4.2 Snowfall comparison . . . . .	68
4.2.1 Sensitivity of the optimal estimation retrieval . . . . .	68
4.2.2 Comparison of surface observations . . . . .	70
4.2.3 MEPS forecast and surface observation comparison . . . . .	74
4.2.4 Comparison of snow water content in the vertical . . . . .	85
4.2.5 Orographic influence on precipitation . . . . .	100
<b>CHAPTER 5: SUMMARY AND OUTLOOK</b>	<b>107</b>
5.1 Outlook . . . . .	110
<b>REFERENCES</b>	<b>112</b>
<b>APPENDIX A: FORWARD MODEL</b>	<b>123</b>
A.1 Scattering Model . . . . .	123
<b>APPENDIX B: RESULTS</b>	<b>126</b>
B.1 Hourly averages ensemble member zero and one . . . . .	126
B.2 Vertical SWC - all ensemble member . . . . .	129

## LIST OF ABBREVIATIONS

<b>ACC</b>	Accretion
<b>AGG</b>	Aggregation
<b>AR</b>	Atmospheric River
<b>AROME</b>	Applications of Research to Operations at Mesoscale
<b>AUT</b>	Autoconversion
<b>BER</b>	Bergeron-Findeisen process
<b>C3VP</b>	Canadian CloudSat-CALIPSO Validation Project
<b>CFR</b>	Contact Freezing of Raindrops
<b>CPR</b>	Cloud Profiling Radar
<b>CV</b>	Coefficient of Variation
<b>CVM</b>	Conversion-melting
<b>DDA</b>	Discrete Dipole Approximation
<b>DEP</b>	Deposition
<b>DRY</b>	Dry processes
<b>DT</b>	Dynamic Tropopause
<b>ECMWF</b>	European Centre for Medium-Range Weather Forecasts

<b>EPS</b>	Ensemble Prediction System
<b>FMI</b>	Finnish Meteorological Institute
<b>HEN</b>	Heterogeneous Nucleation
<b>HON</b>	Homogeneous Nucleation
<b>IVT</b>	Integrated Vapour Transport
<b>LWC</b>	Liquid Water Content
<b>MASC</b>	Multi-Angular Snowfall Camera
<b>MEPS</b>	MetCoOp Ensemble Prediction System
<b>Meso-NH</b>	Mesoscale Non-Hydrostatic model
<b>Met-Norway</b>	Norwegian Meteorological Institute
<b>MetCoOp</b>	Meteorological Co-operation on Operational NWP
<b>MLT</b>	Melting
<b>MRR</b>	Micro Rain Radar
<b>MSLP</b>	Mean Sea Level Pressure
<b>NSF</b>	National Science Foundation
<b>NWP</b>	Numerical Weather Prediction
<b>PIP</b>	Precipitation Imaging Package
<b>PSD</b>	Particle Size distribution
<b>RIM</b>	Riming
<b>SMHI</b>	Swedish Meteorological and Hydrological Institute
<b>SWC</b>	Snow Water Content

<b>SWP</b>	Snow Water Path
<b>WCB</b>	Warm Conveyor Belt
<b>WET</b>	Wet processes
<b>WMO</b>	World Meteorological Organization



# CHAPTER 1: INTRODUCTION

Global warming is predicted to cause an increased frequency of extreme weather events and heat waves, droughts, heavy rains or extremely high winds [Hansen et al., 2014]. Weather and climate extremes can have serious effects on human society and infrastructure, as well as on ecosystems and wildlife. Severe weather events are mostly in the focus of media reports with respect to global warming [Meehl et al., 2000]. Understanding and predicting the impact of extreme weather events is one of the grand challenges of current climate research [Field et al., 2014, Stocker et al., 2013].

This work focuses on the extreme weather event during Christmas 2016, and the snowfall measurements and model forecasts taken at the measurement site Haukeliseter in Southern Norway. The 2016 extreme Christmas storm, named 'Urd' by the Norwegian Meteorological Institute (Met-Norway), and had a large impact on Eastern, Southern, and Western Norway [Olsen and Granerød, 2017]. Storms with high wind speed and precipitation amount are expected to occur approximately every five years. The financial costs associated with the 2016 Christmas storm are estimated to about 180 million Norwegian kroner. 'Urd' led to major traffic problems for cars, trains, ferries and air planes. Most mountain crossings were kept closed during Christmas 2016 [Olsen and Granerød, 2017]. An increase in temperature and therefore a change of frozen to liquid precipitation followed an increase in avalanche danger. In addition, 40 emergency power stations failed during the extreme event affecting around 70.000 households (Figure 1.0.1). Since people are affected by extreme weather it is important to accurately measure and forecast severe storms. The use of accurate observations will lead to better performing weather forecast models, which rely heavily on observations [Joos and Wernli, 2012].

Since winter 2010, Haukeliseter has been a WMO measuring station with single and double fence precipitation instruments. In the winter of 2016/2017, three additional state of the

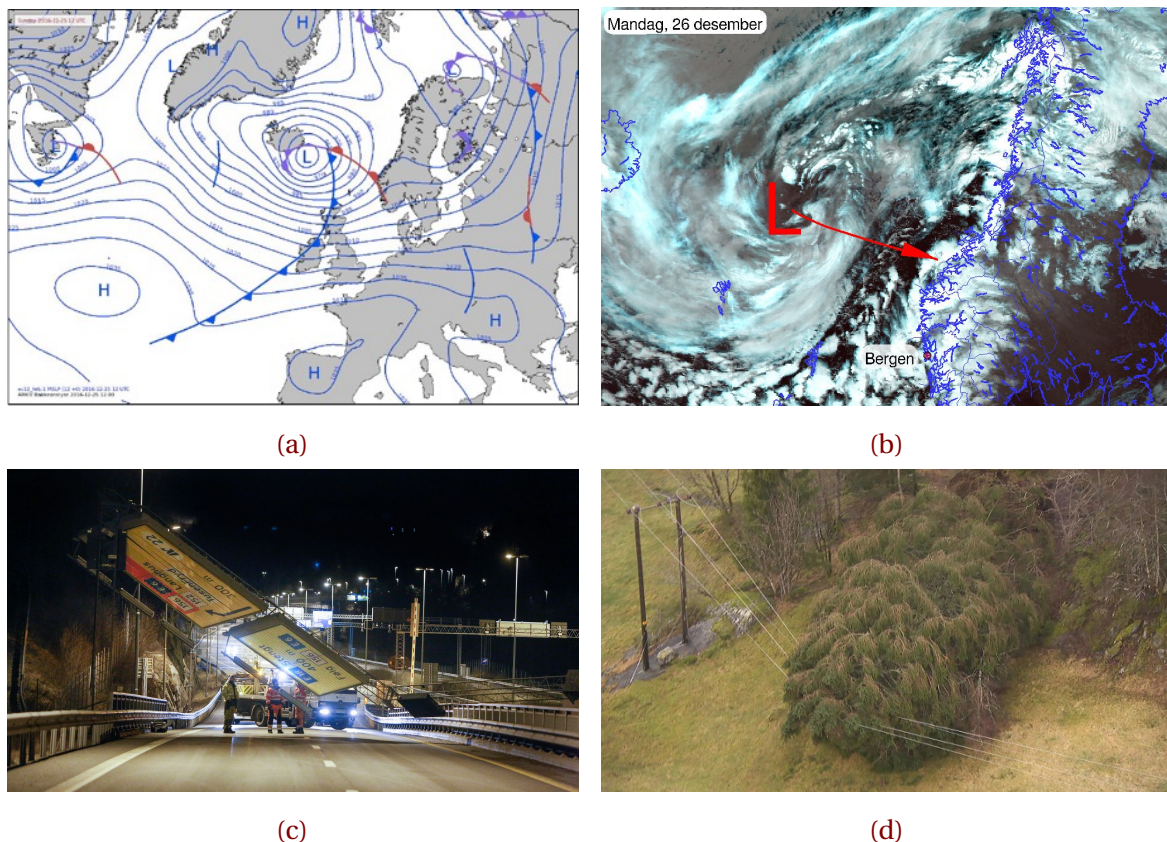


**Figure 1.0.1:** Weather situation during the extreme Christmas storm and impact on the infrastructure. In **a**: Weather situation Sunday 25 December 2016 at 12 UTC from the extreme weather report on Urd [Olsen and Granerød, 2017]. **b**: Tweet from Meteorologene [2016] on 26 December 2016 at 9:34 am: Here comes #Urd! The low pressure centre will hit Møre og Romsdal, but the strongest wind comes south of Stad. #SørNorge. **c** and **d** show the consequences related to the high wind speeds during Christmas 2016. **c**: This traffic sign, ten meter long and four meter high was blown down during the storm, [Ruud et al., 2016]. **d**: Trouble maker: The extreme weather during Christmas created problems for the local infrastructure. 80.000 households were without electricity during the storm, [Farestveit, 2016].

art radar and snowflake microphysical instruments were deployed, which will be used to estimate the vertical profile of snow water content in the atmosphere. Joos and Wernli [2012] showed in a sensitivity study of the microphysical scheme in a regional model for storm development, whether or not the location of the precipitation is correctly simulated. Key was the precipitation profile, which determines the vertical profile

of latent heating. Latent heating leads to potential vorticity generation or destruction followed by a storm amplification or decrease, respectively. Vertical pointing radar reflectivity measurements are rare but can be an improvement to understand the microphysical structure in storms. Radar reflectivities were measured using the 24 GHz Micro Rain Radar (MRR) at Haukeliseter. For this thesis, snowflake characteristics were estimated using a Multi-Angle Snowflake Camera [MASC; [Garrett et al., 2012](#)] and a Precipitation Imaging Package [PIP; [Newman et al., 2009](#)]. An optimal-estimation retrieval algorithm was developed that could estimate snowfall rates consistent with each MRR, MASC, and PIP measurement. This method of estimating snowfall is much like the study from [Cooper et al. \[2017\]](#) for Barrow, Alaska. The main difference between the studies of [Cooper et al. \[2017\]](#) and this thesis here is that a 24 GHz MRR is used instead of a 94 GHz Ka-band ARM (The Atmospheric Radiation Measurement) zenith radar. Additionally, the double fence measurements will provide a boundary condition to ensure that retrieved surface snowfall accumulations are close to the truth. Such agreement will in turn provide confidence in the retrieved snow water contents in the vertical column.

The Meteorological Cooperation on Operational Numerical Weather Prediction (MetCoOp) Ensemble Prediction forecast (MEPS) has been operational at Met-Norway, since 2016. The ensemble prediction system uses the previous deterministic AROME-MetCoOp, a version of the Météo-France Applications of Research to Operations at MEsoscale (AROME). In addition to the deterministic forecast, nine perturbed ensemble members are initialised in MEPS. The newly developed ensemble prediction systems from Met-Norway is used to analyse the extreme winter storm during Christmas 2016.

The thesis is investigating in the thesis if the ensemble prediction system is able to forecast the variation of an extreme winter event such as 'Urd' and if the forecast model is able to predict large scale phenomena as well as local frozen precipitation. Furthermore, the use of an ensemble prediction system will give the possibility to compare the variation of snowfall precipitation at the surface and in the vertical. Observations will help to compare MEPS model forecast to examine the following research questions: Does the regional model cover local affects associated with the topography surrounding the measurement site? Are large scale synoptic phenomena be resolved by MEPS? How well does the model predict the surface snowfall at the Haukeliseter measurement site? **Is there a difference between estimated surface accumulation for different optimal estimation assumptions?**

The thesis is structured as following: The next section provides the background for the motivation of this thesis. Chapter 2 gives an overview of the measurement site Haukeliseter and its instrumentation, followed by the methodology on the optimal estimation retrieval as well as a description of the regional model MEPS, data transformation and the statistical analysis is presented in Section 2.6. The 2016 extreme Christmas event is analysed in Chapter 3. ?? will show the comparison between the double fence gauge measurement and the retrieved snowfall amount at the surface, analyse if large scale phenomena were predicted at Haukeliseter, and discuss overestimation of surface precipitation amount as well as the wind and snowfall related orographic influence. The final chapter summarises the results and gives an outlook for research.

## 1.1 BACKGROUND

It has long been known that measuring precipitation, especially in the form of snow, is difficult. Winter precipitation measurement show biases of more than 100 % between different gauge observation networks and different regions [Kochendorfer et al., 2017]. The local climate changes from station to station leading to different habit and size of frozen aggregates. Measurement uncertainties can be caused by the instrument itself, which varies with wind speed, gauge wind shielding, shape, size, phase, and fall velocity in hydrometeors [Kochendorfer et al., 2017, Wolff et al., 2015]. Uncertainties in precipitation measurements under windy conditions can affect water balance calculation and the calibration of remote sensing algorithms [Wolff et al., 2015].

Precipitation observations are important for hydrological, climate and weather research, as more than one-sixth of the world's population receives water from glaciers and seasonal snow packs [Barnett et al., 2005].

Since winds have an influence on frozen precipitation, a WMO (World Meteorological Organization) precipitation analysis between 1987 and 1993 recommended, that the double-fence inter-comparison reference should be used as a reference for snow measurements [Goodison et al., 1998]. An adjustment for unshielded and single-shielded precipitation gauges followed in 2010. The adjustment transfer function, for single fence gauges, represents a capture efficiency as a function of air temperature and wind speed to delimit the error of measured snowfall [Kochendorfer et al., 2017, Wolff et al., 2015].

The quantitative estimation of snowfall at the global scale from spaceborne measurements has occurred only recently. Initial retrieval approaches were based on passive microwave measurements [Noh et al., 2006, Skofronick-Jackson et al., 2004]. But since these passive measurements can only assess total integrated snow water path for a given column, such efforts were unable to provide much information on the vertical profiles of snow water. The launch of the CloudSat 94 GHz Cloud Profiling Radar (CPR) in 2006, however, provided the first opportunity to examine such vertical structure at a global scale. Several studies, such as Matrosov [2007] and Kulie and Bennartz [2009], have shown that the CPR can be used to estimate snowfall rate but that estimated snowfall values depend heavily upon assumed snowflake microphysical properties. So, for a given radar reflectivity, we can get large differences in estimated snow rate depending upon retrieval assumptions such as snowflake habit and particle size distribution (PSD). For the operational CloudSat snowfall retrieval scheme (2C-SNOW-PROFILE), Wood et al. [2015] developed snowflake particle models based upon video snow disdrometer observations from the Canadian CloudSat-CALIPSO Validation Project [C3VP, Hudak et al., 2006]. Scattering properties for these snow particle models were based upon the Discrete Dipole Approximation (DDA) method. It was hoped that the use of realistic snow properties in the retrievals would lead to reasonable estimates of snowfall in the retrieval. In addition, they derived an a priori relationship between particle size distribution parameters and temperature that they could use as an additional constraint for the snowfall scheme. Use of the flexible optimal-estimation retrieval framework allowed a means to develop a best estimate of snow properties that are consistent with both the CPR reflectivities and the a priori constraint.

They have also been used to estimate snowfall in remote locations such as the Antarctic and Arctic [Kulie et al., 2016, Palerme et al., 2014], that in turn, have been used to evaluate the representation of snowfall in climate models [Christensen et al., 2016, Palerme et al., 2017]. Similarly, these estimates have been used to assess the performance of ground-based radar schemes such as those based upon the operational weather radar system in Sweden [Norin et al., 2015]. Despite such progress, however, the CloudSat scheme can still lead to uncertainties in the retrievals of up to 140 % to 200 % [Wood, 2011] for individual storms.

Again, these uncertainties arise from the large variance in snowflake microphysical properties as observed in nature. In response, Cooper et al. [2017] explored the use of in-situ,

event specific observations of snowflake microphysical properties to improve radar-based retrievals of snowfall. This work was based upon observations from the Ka-band ARM Zenith Radar (KAZR) and Multi-Angle Snow Camera (MASC) deployed at the ARM Climate Facility Site at Barrow in Spring 2014. This ground-based 35 GHz retrieval scheme was modified from the space-borne 94 GHz CloudSat retrieval scheme developed by [Wood \[2011\]](#). But instead of using a temperature dependent a priori characterisation of PSD, [Cooper et al.](#) introduced the in-situ observations of particle size distribution through the a priori terms of the optimal-estimation framework.

Preliminary analyses suggest good performance for this retrieval scheme at Barrow. Estimates of snowfall from the [Cooper et al. \[2017\]](#) approach differed by 18 % relative to nearby National Weather Service snow gauge measurements for total accumulation over multiple snow events. However, given limited snowfall observed at Barrow during the MASC deployment, it was difficult to come to any definitive conclusions about retrieval performance. The NSF (National Science Foundation) funded field campaign with MRR, MASC, and PIP (Precipitation Imaging Package) deployment at Haukeliseter provides an ideal opportunity to further explore this retrieval approach. This study will continue to examine the sensitivity of retrieval surface snowfall rate to assumptions of habit, fall speed, and particle size distribution as in [Cooper et al. \[2017\]](#). But the work presented here will be different in that we also will examine the vertical profiles of snowfall through the atmospheric column.

With the increasing expansion of computational power, developments of high-resolution numerical weather forecasting models with  $\leq 4$  km scales can be able to represent small-scale phenomena, such as convective dynamics [[Gowan et al., 2018](#)]. This enhancement provides weather services the ability to improve short-term weather forecasts for convective events, which can seriously impact infrastructure and society [[Müller et al., 2017](#)]. Information on magnitudes and location of maximum temperature is of significant importance when warnings are published by meteorological services for severe weather events and for further use in downstream impact model, e.g. NVE's (Norwegian Water Resources and Energy Directorate) hydrological model for flooding and avalanche risk. The ability to use high-resolution models is also followed by various challenges, such as physical parametrisation schemes, accurate representation of topography, and data assimilation of high-resolution data [[Sun, 2005](#)].

The weather forecast in Scandinavia covers a wide range of phenomena and includes continental, maritime and polar conditions. Norway has a complicate coastline, gradients in land use, as well as complex topography, which can complicate local weather forecasting of temperature, wind and precipitation [Müller et al., 2017]. Colle et al. [2005], Garvert et al. [2005], Schwartz [2014], for example, have shown, that simulations of orographic precipitation can be improved in mountainous terrain for horizontal grid spacing below 4 km. Uncertainties on a convective scale can lead to a rapid error growth [Lorenz, 1969], hence high-resolution ensemble prediction makes it possible to estimate the forecast uncertainty by performing several model runs, each with different initial conditions.

The Christmas storm in 2016, might not have led to the same damages as some of the extreme weather events of recent years. As people and infrastructure are affected by extreme weather, it is necessary to further improve the accuracy of snow-ground observations to better verify numerical weather forecasts, hydrological and climate models [Joos and Wernli, 2012]. Changes in snow pack characteristics after extreme rain on snow events can lead to severe avalanches [Stimberis and Rubin, 2011] and to the formation of thick layers of ice in the snow pack or on ground [Hansen et al., 2011, Putkonen and Roe, 2003].

# CHAPTER 2: SITE, INSTRUMENTATION, DATA, AND METHODOLOGY

This chapter describes the site, instruments, the optimal estimation retrieval and the regional forecast model used to determine the vertical profile of snow water content for observed snow events. The determination of required parameters from the measuring instruments in relation to the optimal estimation retrieval will be explained. The purpose of this study is to compare the vertical observations from the Haukeliseter measurement site and the output from the operational forecast model at the Norwegian Meteorological Institute for the extreme weather event during Christmas 2016. The last section will give an insight on how the data was analysed to compare the different systems.

## 2.1 HAUKELISETER SITE

Haukeliseter, shown in Figure 2.1.1 is a mountain plateau 991 m above sea level, located in the Norwegian county 'Telemark' (59.8° N, 7.2° E, Figure 2.1.1). The station measures precipitation, temperature, snow depth and wind. It has served as a measurement site for snow accumulation since the winter of 2010/2011 [Wolff et al., 2010, 2013, 2015] and serves as WMO (World Meteorological Organization) station.

The study site is surrounded by mountain tops being 100 m to 500 m higher than the flat area. As seen in Figure 2.1.1c is Haukeliseter more open to the south and the south-west and the closest mountain top (situated to the NE) has an altitude of 1162 masl, [Wolff et al., 2015]. The mountains west to north exceed elevations of 1600 m.

A detailed setting of the measurement site is shown in Figure 2.3.1. The precipitation sensors are perpendicular to the predominant wind. Additional measurements of other

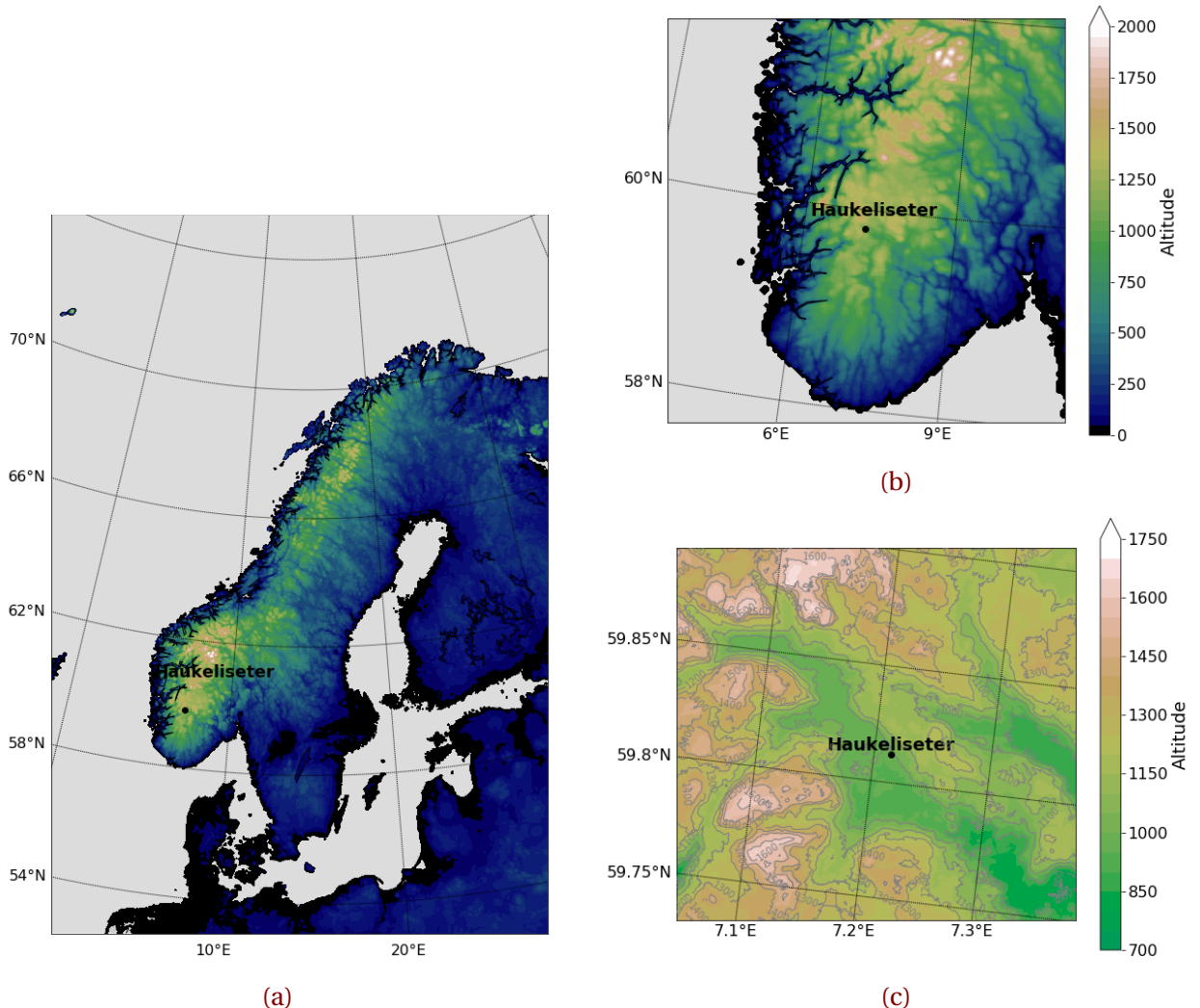


**Figure 2.1.1:** Model elevation map of Northern Europe (a) and Southern Norway (b), where the model domain of MEPS are presented in Lambert projection. The elevation corresponds to the legend of b. A topographic map of the measurement site is shown in c with DTM 10 Terrain Model (UTM33) from [Geonorge \[2018\]](#).

meteorological parameters such as temperature, wind, and pressure are used to connect the large-scale weather situation with the local measurements. The data is provided by [eklima \[2016\]](#), where the temperature is measured at double fence height. The hourly value of temperature is represented by the last minute value of the previous hour measurement. The 10 m wind is measured by an ultrasonic wind sensor from Gill, mounted at the tower

close to the double fence. Wind data is obtained from [eklima \[2016\]](#) and represents 10 min averages from the last 10 min of an hour.

## 2.2 CLIMATE AT HAUKELISETER

The general climate at Haukeliseter can be defined with the updated Köppen-Geiger climate types presented in [Peel et al. \[2007\]](#). Figure 8 in [Peel et al. \[2007\]](#) show, that Haukeliseter may lay in a transition zone and can be categorized as ET, a polar tundra climate type (hottest month temperature  $T_{hot} \geq 0^{\circ}\text{C}$ ) or as Dfc, a cold climate without dry season and cold summers. Haukeliseter presents a typical Norwegian climate condition. At the measurement site, frequent snow events combined with high wind speeds are observed during a six to seven month winter period. In addition, a snow amount of about two to three meter can be expected, where 50 % of the yearly precipitation is solid in the form of snow, graupel or mixed-phase precipitation [[Wolff et al., 2010, 2013, 2015](#)].

The mean wind direction (Figure 2.3.1) for solid precipitation is from the west/east with maximum wind speed above  $15 \text{ m s}^{-1}$ , observed during a 10-year winter period at a nearby station [[Wolff et al., 2010, 2015](#)]. In Figure 2.2.1, the green dashed line represents the average December temperature of  $-6^{\circ}\text{C}$  (30-yr period 1961 to 1990,[[eklima, 2016](#)]). December 2016 was warmer with an anomaly of +4.9 K above the climate mean. In 2016, the precipitation was 200 % more than the climate mean during December. This difference could be associated with the new installation of the double fence - Geonor gauge at Haukeliseter. In [Wolff et al. \[2015\]](#), Figure 5 shows that single fence precipitation gauges underestimate the amount of precipitation about 80 % during high wind speed events. Since the Double Fence construction was not in use before 2010/2011, which might have led to an observation of too little precipitation at Haukeliseter during winter and a followed incorrect climate statistic. The precipitation observed in the period of 21 to 27 December 2016 where 56.9 % of the total accumulated precipitation in December 2016. Furthermore, a maximum wind of  $22.3 \text{ m s}^{-1}$  was observed in this period, which can be associated with a slight storm (Section 3.5 and Table 3.1.1).

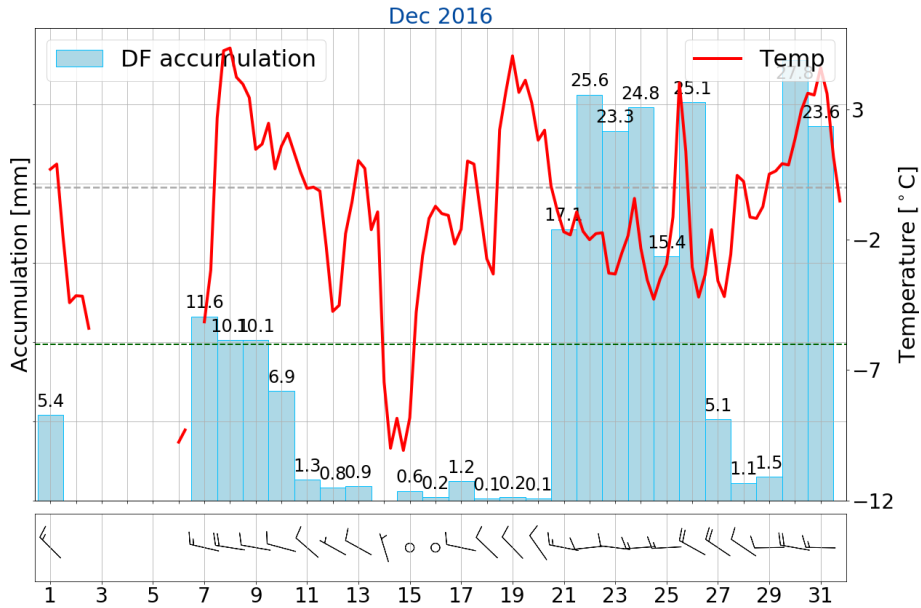


**Figure 2.2.1:** Observations at Haukeliseter weather mast during December 2016. The daily accumulation is presented in light blue [mm]; the six hour mean temperature in red, [ $^{\circ}\text{C}$ ], and daily maximum 10 m wind as barbs [ $\text{m s}^{-1}$ ]. Gray dashed line indicates the freezing temperature. The freezing temperature is indicated by the green dashed line and the monthly normal value ( $-6.0^{\circ}\text{C}$ ) by the green [eklima \[2016\]](#). Note, no data was available from 2 to 6 December 2016.

## 2.3 INSTRUMENTS

The WMO site Haukeliseter, operated by Met-Norway serve numerous meteorological measurements of temperature, wind speed and direction. 10 m wind and 4.5 m air temperature are measured at the tower close to the double fence (Section 2.3.1). The wind measurements are performed with an ultrasonic wind sensor from Gill (Wind observer II with extended heating). Air temperature is obtained with a pt100 element at gauge height and protected by standard Norwegian radiation screen [Wolff et al., 2015]. Pressure?

Further information about the WMO site and the instrument setting, can be found in Wolff et al. [2013, 2015].

A collaboration between the University of Utah, University of Wisconsin and Met-Norway made it possible to install three additional instruments at the measurement site during winter 2016/2017. A Micro Rain Radar (MRR) is used to obtain particle reflectivity and Doppler velocity aloft, thus providing the vertical structure of the storm. Additionally, a

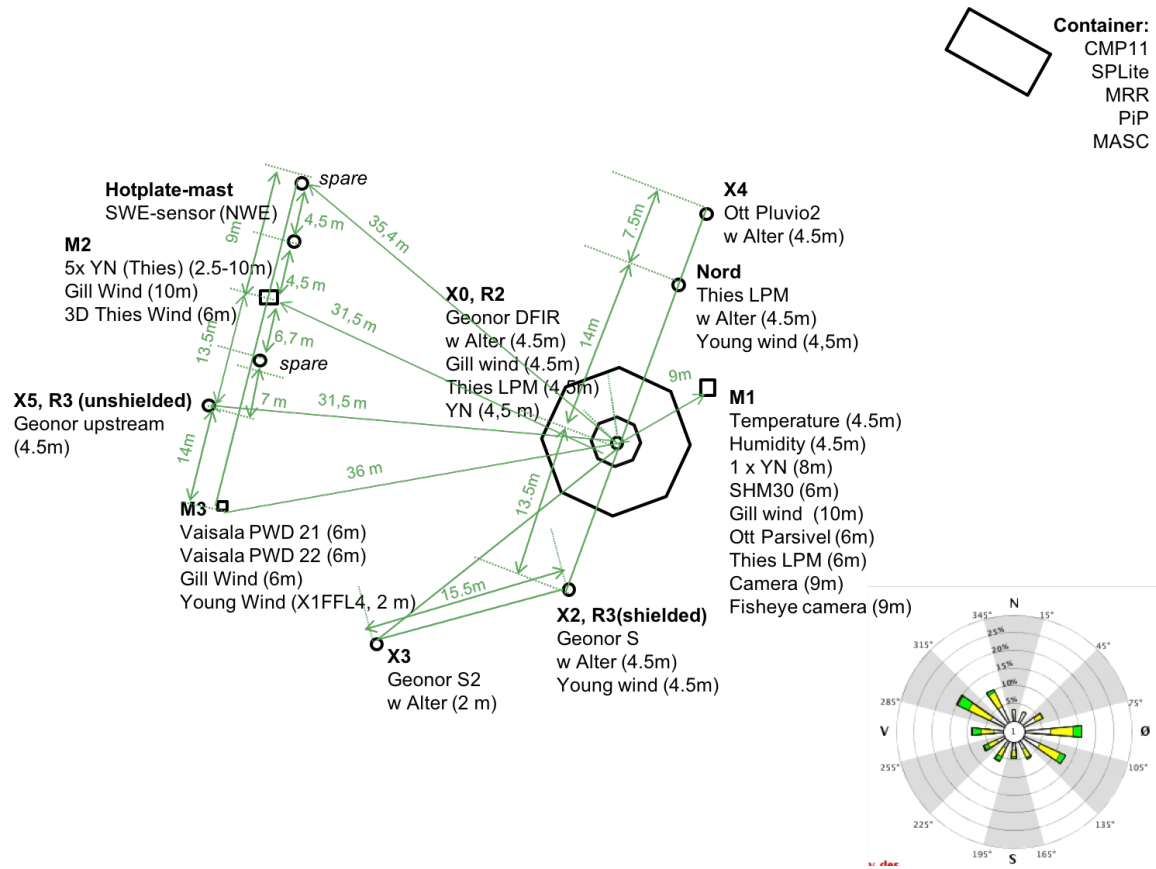


**Figure 2.3.1:** Instruments at the Haukeliseter measurement site during winter 2016/2017 [adapted from Wolff et al., 2015]. The windrose indicates the mean wind direction from either from west-north-west or east-south-east.

Multi-Angle Snowflake Camera (MASC) and a Precipitation Imaging Package (PIP) will be used to determine the snow habit, the snowfall particle size distribution, and the near-surface fall speed. Since many factors such as humidity and temperature contribute to snowflake geometry, the use of these instruments will provide knowledge of snowflake habits, particle size distributions, and fall speed crucial to reduce error in snowfall retrievals.

A sketch of the instrumentation setting is presented in Figure 2.3.1. The octagonal indicates the double fence. The container is north-east from the double fence having the MRR, MASC and PIP mounted at the top. **M1** in Figure 2.3.1 is the 10 m weather mast, providing

the hourly [eklima \[2016\]](#) temperature, pressure, and wind measurements. The mean wind direction from west-north west and east-south east are shown in the wind rose in Figure 2.3.1.

### 2.3.1 DOUBLE FENCE SNOW GAUGE

Since the winter 2010/2011 Haukeliseter is equipped with several precipitation gauges. The wind shielded gauges are placed perpendicular to the main wind direction (E/W wind).

The wind-induced under-catch of solid precipitation is determined by [Wolff et al. \[2015\]](#). The wind plays different roles in the amount of accumulation depending on the kind of precipitation. For temperatures below  $-2^{\circ}\text{C}$  the wind speed influences the falling snow. Where less precipitation can be observed at higher wind speeds or more precipitation can be measured if too much is blown into the gauge. The catch ratio between the standard Geonor precipitation gauge and the Double Fence - Geonor (Figure 2.3.2a) shows that only 80 % of solid precipitation is observed at wind speeds of  $2\text{ m s}^{-1}$  whereas only 40 % at  $5\text{ m s}^{-1}$ , Figure 5 in [Wolff et al. \[2015\]](#).

The precipitation gauge protected by an octagonal double fence (Figure 2.3.2a) is more accurate than the single fence and will be used as the reference to all surface accumulation measurements. The double fence creates an artificial calm wind and maximize the catch of precipitation, [\[Wolff et al., 2010, 2013, 2015\]](#). The wind inside the double fence is measured to be not much higher than  $5\text{ m s}^{-1}$  even if the winds out-

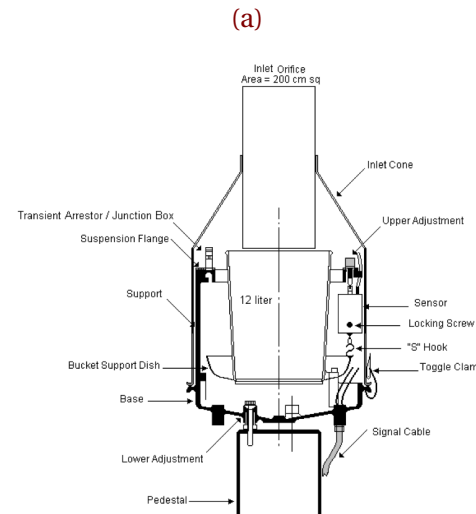


**Figure 2.3.2:** a: Double fence and unprotected precipitation gauges at Haukeliseter, from [Wolff et al. \[2015\]](#). The prevailing wind direction from east comes from the lower, left corner in the image and the west wind from the opposite site. b: Vertical cross section of T-200B precipitation gauge [[Geonor Inc., 2015](#)].

side exceed  $20 \text{ m s}^{-1}$  (occurred 26 December 2016). Alternatively, a bush gauge is a precipitation gauge surrounded by a large bush to create artificial calm winds to increase the catch ratio of frozen precipitation and is considered as the best available measurement for solid precipitation [Wolff, 2018]. Unfortunately there are only two bush gauges in the world, and because of local limitations a double fence construction is developed as reference for the Solid Precipitation Measurement intercomparison study during 1986 to 1993 [Goodison et al., 1998]. Wolff [2018] comparison between bush gauge and double fence precipitation measurements have shown, that the double fence will measure up to 10 % less precipitation for wind speeds up to  $9 \text{ m s}^{-1}$  outside the fence. As for now, no detailed comparison between bush gauge and double fence exists at thigh wind speeds. Extrapolation of measurement observations where double fence and bush gauge exist, let believe that the double fence will not underestimate more than 20 % during high wind speed events with frozen precipitation.

This shows the need of a combination of ground-based observations together with an optimal estimation retrieval to verify the accuracy of MEPS. Wolff et al. [2015] introduced an adjustment function for the Geonor double fence, so that different precipitation under certain wind speeds are presented correctly and can be used as confidential data. For now, it is presumed that the average under catch inside a double fence is 20 % for wind speeds between  $10 \text{ m s}^{-1}$  and  $20 \text{ m s}^{-1}$  and 10 % for wind speeds below  $9 \text{ m s}^{-1}$  [Wolff, 2018].

Inside the double fence is a precipitation-weighing gauge Geonor T-200B3 [3-wire transducers, 1000 mm, Geonor Inc., 2015] with an Alter wind screen to reduce wind turbulence around the gauge. At Haukeliseter the orifice height of the Geonor is 4.5 m above the ground because of an expected snow depth of two to three meter during a winter season and the likelihood of measuring drifting snow [Wolff et al., 2013, 2015].

A vertical cross section of the T-200B gauge is shown in Figure 2.3.2b. The precipitation particles fall through the  $200 \text{ cm}^2$  orifice protected with a heated collar, into a cylindric bucket filled with frost protection. The bucket is placed on top of a Bucket Support Dish [Figure 2.3.2b, Geonor Inc., 2015]. This dish is connected with three wire sensors having an eigenfrequency changing with the weight inside the bucket. A formula provided by Geonor Inc. [2015] calculates the amount of precipitation with the frequency of each sensor. The three sensors provide a reduction of an error in connection with an unlevel installation. Met-Norway average the values of all three sensors and provide hourly data at eklima.

### 2.3.2 MRR - MICRO RAIN RADAR

Radars are very useful to observe the vertical profile of the atmosphere. The instrument detects mesoscale features and makes it possible to visualise the vertical structure of storms [Markowski and Richardson, 2011].

The principle of radar measurements is based on an electromagnetic wave, which is emitted from the radar transmitter and interacts with the hydrometeors along the beam. A fraction of the pulse energy is reflected back to the receiver of the radar. The quantity of scattering depends on the shape and structure of the reflected particle. Vertical profiles of reflectivity give information about the diameter of the target object.

The Micro Rain Radar (Figure 2.3.3) measures profiles of Doppler spectra [METEK, 2010]. The Doppler spectrum describes the movement of the particle. The vertical pointing Doppler radar measures the returning energy from each interval and enables the detection of the Doppler spectrum [L'Ecuyer, 2017]. The MRR has a frequency of 24 GHz and a temporal and spatial resolution of 60 s and 100 m, respectively. The radar height range from 100 m (because of ground clutter) to 3.000 m [METEK, 2010].

MRR radar reflectivity ( $Z$ ) is transformed from  $1 \text{ mm}^6/\text{m}^3$  to dBZ, by the following relationship;

$$Ze = 10 \log_{10} \left( \frac{Z}{1 \text{ mm}^6/\text{m}^3} \right) \quad [\text{dBZ}] \quad (2.3.1)$$

A transformation to rainfall rates can be performed by the  $Z-R$  (reflectivity - rainfall) relationship. The rainfall rate in each layer can be estimated by the use of typical fall speeds and the Marshall-Palmer particle size distribution for liquid particles [Rinehart, 2010], Equation (2.3.2)

$$Z = 200R^{\frac{8}{5}} \quad [\text{mm}^6\text{m}^{-3}]$$

$$R = \left( \frac{10^{\frac{Ze}{10}}}{200} \right)^{\frac{8}{5}} \quad [\text{mmh}^{-1}] \quad (2.3.2)$$



**Figure 2.3.3:** Micro Rain Radar at the measurement site in Kiruna.

the radar. The quantity of scattering depends on the shape and structure of the reflected particle. Vertical profiles of reflectivity give information about the diameter of the target object.

The Z-R relationship with the Marshall-Palmer assumption (Equation (2.3.2)) applied is represented in Table 2.3.1. Z-snowfall relationships are developed but are difficult to apply due to the variation of size and density of the particles [L'Ecuyer, 2017].

After the transformation to dBZ the reflectivity is averaged for every 200 m thick layers, where only values above 300 m taken into account, e.g. a reflectivity at 400 m represents the mean value of reflectivity between 300 m and 500 m.

**Table 2.3.1:** Typical reflectivity values for 94 GHz radar, according to Doviak and Zrnic [1993], obtained from measurements, models, and observations. The rainfall rate  $R$  is calculated with Equation (2.3.2).

	<b>Ze</b> [dBZ]	<b>R</b> [mm h <sup>-1</sup> ]
<b>Drizzle</b>	<25	1.3
<b>Rain</b>	25 to 60	1.3 to 205.0
<b>Snow</b>		
dry, low density	<35	5.6
Crystal; dry, high density	<25	1.3
wet, melting	<45	23.7
<b>Graupel</b>		
dry	40 to 50	11.5 to 48.6
wet	40 to 55	11.5 to 99.9
<b>Hail</b>		
small; <2 cm, wet	50 to 60	48.6 to 205.0
large; >2 cm, wet	55 to 70	99.9 to 864.7
<b>Rain &amp; Hail</b>	50 to 70	48.6 to 864.7

### 2.3.3 PIP - PRECIPITATION IMAGING PACKAGE

The Precipitation Imaging Package (PIP) is a video disdrometer that is a modification of the Snowflake Video Imager presented by [Newman et al. \[2009\]](#). It consists of a halogen flood lamp and a video system that samples at 60 Hz (Figure 2.3.4). Both lamp and lens have a distance of approximately 3 m that follows a field of view: 32 mm by 24 mm.

In front of the halogen lamp there is a frosted window, so that the background light is uniform over all time. A falling particle appears as a 2-D shadow in the video image. Particle size distribution (PSD) and fall speed of precipitation can be determined from the black and white images provided by the system. The instrument also can give first order estimates of snowflake particle habit when in focus in the images. [Newman et al. \[2009\]](#) describes the details of the algorithm applied to the system to get information about the snow-particle habit. The winds have almost no effect on the result of the video distrometer [[Newman et al., 2009](#)]. To reduce eventual wind effects, the distrometer was oriented perpendicular to the mean wind.



Figure 2.3.4: Precipitation Imaging Package.

### 2.3.4 MASC - MULTI-ANGULAR SNOWFALL CAMERA

The Multi-Angular Snowfall Camera (MASC) takes high-resolution images of hydrometeors in free fall and measures the fall-speed simultaneously.

The MASC consists of three cameras, three flashes, and two near-infrared sensors, pointing at a ring centre (Figure 2.3.5). A hydrometeor has to pass through the ring in a certain way to trigger the near-infrared sensors. At the same time the three cameras take a picture of the falling particle. Since the cameras take pictures from three different angles, the particles size, shape, and orientation can be specified from an algorithm applied to the image, described in [Garrett et al. \[2012\]](#). Furthermore, the form and heritage of the hydrometeor, such as collision-coalescence, riming, capture nucleation, or aggregation, can be estimated.

The near-infrared sensor, that is used to trigger the cameras and the lights quantifies the fall-speed of the hydrometeors, by measuring the time the particle needs to pass the distance between the upper and lower trigger.

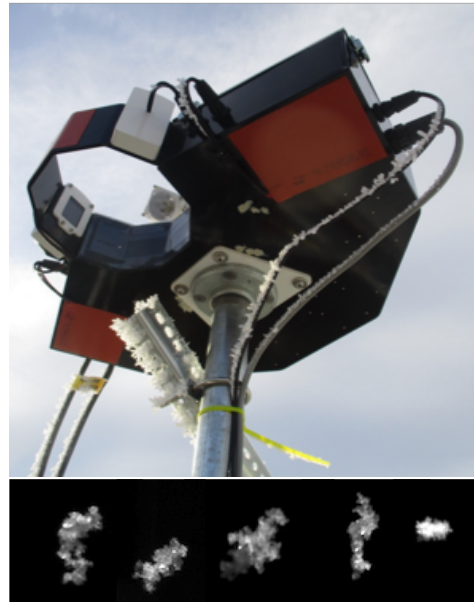


**Figure 2.3.5:** MASC and images taken by instrument during the Christmas storm 2016.

## 2.4 OPTIMAL ESTIMATION RETRIEVAL ALGORITHM

The purpose of this study is to apply an optimal-estimation snowfall retrieval on ground based measurements to estimate the surface accumulation and vertical snow water content for an extreme event during Christmas 2016. These will later be used to compare to 48 h MEPS model forecasts to see if the model was able to predict synoptical features and precipitation related to the extreme event 'Urd' in 2016.

### 2.4.1 SNOWFALL RETRIEVAL SCHEME

The optimal-estimation snowfall retrieval scheme was modified for the Barrow instrumentation described in [Cooper et al. \[2017\]](#) to the 24 GHz MRR, MASC, and PIP located at Haukeliseter. This scheme was then used to derive surface snowfall rates and vertical profiles of snow water content using different combinations of retrieval assumptions based upon in-situ observations. Here a discussion of the optimal-estimation framework is presented so that the reader can understand exactly how the different measurements in the retrieval scheme were incorporated. The differences in the forward and inverse problem are reviewed in the beginning. Both, forward and inverse problem underlie the basic methodologies of remote sensing.

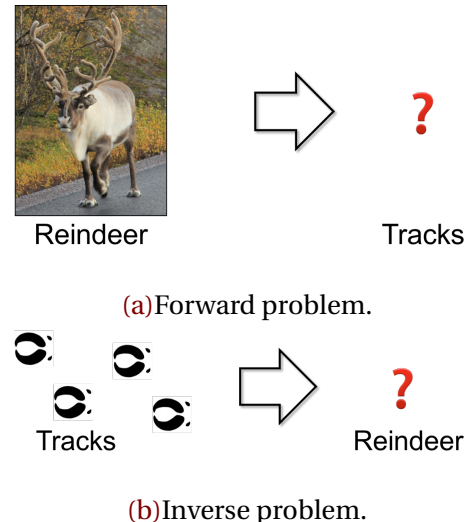


**Figure 2.4.1:** **a:** Relationship between parameter of interest (reindeer) and the unknown parameter of measurements (tracks). **b:** Inverse problem when the parameter of measurements is known but the parameter of interest is not [[Stephens, 1994](#)].

The general concepts of forward and inverse problems are illustrated in Figure 2.4.1. The forward problem describes the relationship between the physical parameters of interest and the measurements (Figure 2.4.1a). In Figure 2.4.1b, the physical parameter is the reindeer and the measurements are its tracks. In the here presented thesis snowfall scheme, the physical parameters are the vertical profiles of snow water content (SWC) and the measurements are the MRR reflectivities. The inverse problem represents the opposite goal. The physical entity (reindeer and SWC) must be inferred from the measurements (reindeer tracks or MRR reflectivities).

The optimal-estimation framework is used to solve the inverse problem for the thesis work. But it is more complex than the direct inversion as represented in Figure 2.4.1b. Instead of inverting directly for the parameter of interest (SWC) from the measurements [dBze], the scheme includes additional information based upon an 'a priori' understanding of the physics of the retrieval problem. Thus, it represents a weighted balance between what

the data can tell about the state and what is already known about it. For the CloudSat retrieval scheme, this a priori information came from a parametrisation relating particle size distribution (PSD) to temperature. For the Barrow and Haukeliseter schemes, the a priori information could also come from the in-situ observations of snowflake microphysics. These constraints also add numerical stability to the inversion process when there are either calibration errors in the measurements or uncertainties in the forward model that relates the physical parameter to measurement space. Details of the radar forward model are discussed at the end of this section.

The optimal estimation method is based on Gaussian statistics. It solves for snowfall properties of interest or retrieval vector,  $\mathbf{x}$ , by minimizing the scalar cost function,  $\Phi$ , as in Equation (2.4.1).

$$\begin{aligned}\Phi(\mathbf{x}, \mathbf{y}, \mathbf{a}) = & (\mathbf{y} - F(\mathbf{x}))^T \mathbf{S}_y^{-1} (\mathbf{y} - F(\mathbf{x})) \\ & + (\mathbf{x} - \mathbf{a})^T \mathbf{S}_a^{-1} (\mathbf{x} - \mathbf{a})\end{aligned}\quad (2.4.1)$$

Specifically, or this thesis retrieval scheme,  $\mathbf{x}$  represents the PSD parameters of slope and number intercept of an assumed exponential size distribution for each radar range bin as in Equation (2.4.2).  $\mathbf{y}$  is the vector of MRR reflectivities. The vector  $\mathbf{a}$  is the a priori guess for slope parameter and number in each range bin.  $F(\mathbf{x})$  represents the forward model that translates snow properties into reflectivity space. Minimizing the cost function therefore seeks to reduce the difference between the observations,  $\mathbf{y}$ , and simulated observations,  $F(\mathbf{x})$  and between the a priori guess ( $\mathbf{a}$ ) and the retrieval vector ( $\mathbf{x}$ ).

$$n(r) = N_0 \exp(-\lambda r) \quad [\text{m}^{-3} \text{ mm}^{-1}] \quad (2.4.2)$$

The  $\mathbf{S}_y$  and  $\mathbf{S}_a$  terms, in Equation (2.4.1), represent the forward model and measurement error covariance matrix and the a priori error covariance matrix, respectively. The relative differences between  $\mathbf{S}_a$  and  $\mathbf{S}_y$  weight the importance of the observations and the a priori considerations in determining our best estimate of PSD properties.

Newtonian iteration is used until the value of the cost function converges and our best estimate of snowfall properties are found. The optimal-estimation scheme also provides error diagnostics through the retrieval error covariance matrix,  $\mathbf{S}_x$ , as in Equation (2.4.3).

$$\mathbf{S}_x = \left( \mathbf{S}_a^{-1} + \mathbf{K}^T \mathbf{S}_y^{-1} \mathbf{K} \right)^{-1} \quad (2.4.3)$$

The Jacobian matrix,  $\mathbf{K}$ , represents the sensitivity matrix of the perturbed result of the forward model. The true state  $\mathbf{x}$  is perturbed by 0.2 % and thus  $\mathbf{K}$  represents the relation between simulated values to the true state and how sensitive the simulated values are to small changes when starting a new retrieval cycle. The closer  $\mathbf{K}$  is diagonal, the more is  $\mathbf{x}$  determined by the real observed and a priori values. If the limit of the partial derivative is close to unity, the retrieved value  $\mathbf{x}$  is its true state [Wood, 2011].

In practical application for this multiple layer retrieval scheme, log-transformed particle size distribution parameters of slope and number intercept were used due to the large expected range of these variables. The state vector,  $\mathbf{x}$ , is defined in Equation (2.4.4).

$$\mathbf{x} = \begin{bmatrix} \log(\lambda)_0 \\ \vdots \\ \log(\lambda)_{\text{nlayer}} \\ \log(N_0)_0 \\ \vdots \\ \log(N_0)_{\text{nlayer}} \end{bmatrix} \quad \text{nlayer} = 14 \quad (2.4.4)$$

The usage of a priori terms were explored both from in-situ microphysical observations and from the PSD-temperature relationship developed for the CloudSat scheme as in Equations (2.4.5) and (2.4.6). Temperatures in °C at Haukeliseter were taken from site measurements with an assumption of a moist adiabatic lapse rate for the observed snow events. The log transformed slope and number intercept values were taken from Wood [2011].

$$\log(\lambda) = -0.03053 \cdot T_{ap} - 0.08258 \quad [\log(\text{mm}^{-1})] \quad (2.4.5)$$

$$\log(N_0) = -0.07193 \cdot T_{ap} + 2.665 \quad [\log(\text{m}^{-3} \text{mm}^{-1})] \quad (2.4.6)$$

The log-transformed equations are useful, since the results from C3VP were similar to other observations. The study showed, that  $N_0$  ranges over several order of magnitude as well as  $\lambda$  was non-Gaussian for the snow events Wood [2011]. The diagonal matrix elements in  $\mathbf{S}_a$  (Equations (2.4.1) and (2.4.3)) are equal to 0.133 and 0.95 for the particle slope parameter and the number intercept, respectively, as from Eq. 7.35 and 7.36 in Wood [2011]. The diagonal matrix elements for  $\mathbf{S}_y$  are 2.5<sup>2</sup> in Equations (2.4.1) and (2.4.3).

After the best estimate of PSD parameters are found, the snow water content in each layer is calculated using the snow particle mass-dimension relationships as in Appendix A.1.

$$\text{SWC} = \int_{r_{min}}^{r_{max}} m(r)n(r)dr \quad [\text{gm}^{-3}] \quad (2.4.7)$$

$r$  is the particle maximum dimension and  $m(r)$  the related mass.

This thesis work considered the database of particle models developed for the CloudSat mission, e.g. different types of aggregates, sector plates, and columns. Scattering properties for these snowflakes were calculated for the 24 GHz frequency using discrete dipole approximation (DDA). Observations from the MASC of snowflake habit were used to guide particle selection. Snow water content, in turn, was translated into a snowfall rate using fallspeed observations (MASC, PIP, or MRR Doppler velocity) or climatological analyses. Surface snowfall rate is estimated using the SWC from the lowest non-noise reflectivity and radar bin.

The forward model that calculates simulated 24 GHz MRR reflectivities from PSD parameters was modified from that used in the CloudSat 94 GHz operational snowfall product (2C-SNOW-PROFILE). Backscatter from frozen hydrometeors in each radar bin is summed up as in Equation (2.4.8) form which reflectivity factor, Z, can be found (Equation (2.4.9)).

$$\eta_{bk} = \int_{r_{min}}^{r_{max}} n(r)\sigma_{bk}dr \quad [\text{m}^{-1}] \quad (2.4.8)$$

$$Ze^{ss,na} = \frac{\Lambda^4}{\|K_w\|^2 \pi^5} \eta_{bk} \quad [\text{mm}^6 \text{m}^{-3}] \quad (2.4.9)$$

where,  $\Lambda$  is the wavelength of the radar;  $\|K_w\|^2$  is the complex refractive index of water. Radar backscatter values were estimated using discrete dipole approximation for the CloudSat particle models at 24 GHz. Unlike the 94 GHz spaceborne CloudSat mission, multiple scattering and attenuation can be neglected for 24 GHz MRR and the short path length retrievals as viewed from the ground perspective.

## 2.4.2 ENVIRONMENTAL MASKS FOR THE OPTIMAL ESTIMATION RETRIEVAL

Different steps and assumptions are done in the here presented snowfall retrieval, to achieve vertical profiles of snowfall from MRR. The snowfall rate at the surface can be

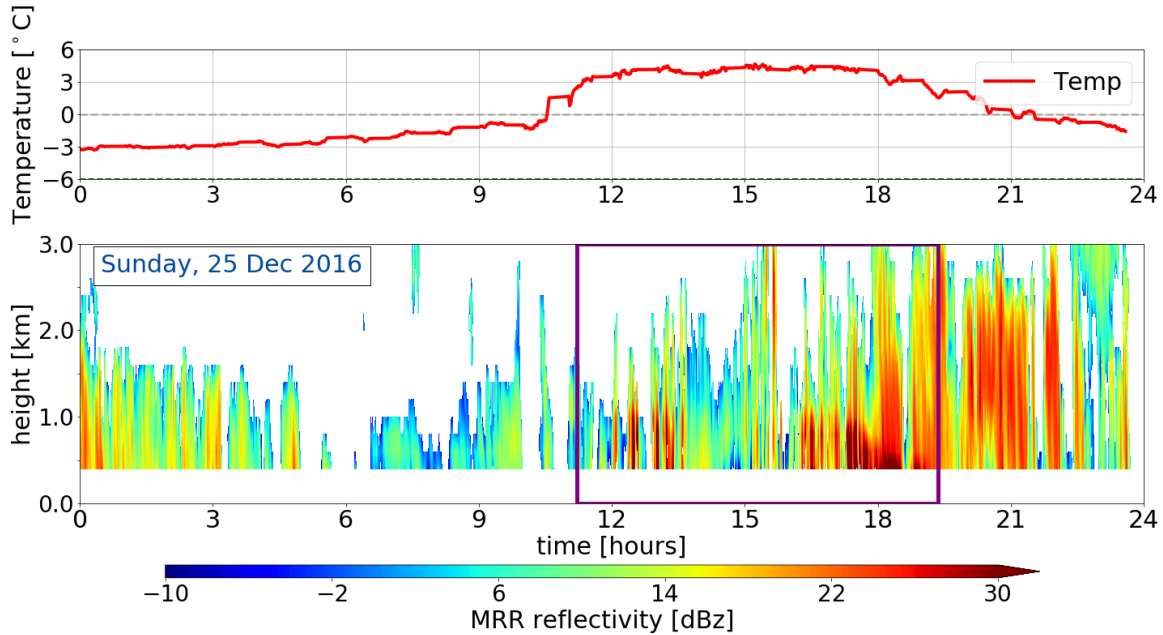


**Figure 2.4.2:** A priori temperature dependence within the optimal estimation retrieval for an all day precipitation event on 25 December 2016. The upper panel shows the surface a priori guess,  $T_{ap}$ , measured at the Haukeliseter site. The lower panel presents the reflectivity measure by the MRR. Additionally, indicates the purple frame the time, where the MRR reflectivity was larger than  $-10 \text{ dBZ}$  and surface temperatures less than  $2^\circ\text{C}$

estimated from one of the lower levels. The optimal estimation retrieval is only performed for profiles, which are likely to have observed snow.

This value was chosen as sensitivity studies [e.g. Wood et al., 2013] that a days worth of such reflectivities would produce only a trace of snow. Such a value therefore guarantees that a significant snow event is not missed and that any storms with lower dBZ values would not produce meaningful precipitation.

The Haukeliseter measurement site is equipped with a weather mast, measuring the air temperature every minute at two-meter height (compare Figure 2.4.2, upper panel). Since the MRR measures above 300 m and temperature measurements exists only at the surface, a priori temperature ( $T_{ap}$ ) at the surface is assumed to be similar to the observed near-surface air temperature. The use of a moist adiabatic lapse rate of  $dT/dz = 5 \text{ K km}^{-1}$  gives  $T_{ap}$  in each layer. Snow existence at temperature measurements up to a threshold of  $+2^\circ\text{C}$  are assumed. Liu G. [2008] validated this threshold, by analysing present weather reports

to find the distinction between liquid and solid precipitation.

The purple line in the lower panel of Figure 2.4.2 represents the time frame during 25 December 2016, where the MRR reflectivity is less than  $-15 \text{ dBZ}$ , and a priori temperature passes the  $2^\circ\text{C}$  limit at the surface.

## 2.5 OPERATIONAL WEATHER FORECAST MODEL - MEPS

MEPS (MetCoOp Ensemble Prediction System) was newly operational at Met-Norway when the extreme weather occurred in Norway. Comparing model data with actual observations helps to verify the agreement between model prediction and ground-based measurements.

AROME-MetCoOp was operational from March 2014 until November 2016, when it was replaced with an ensemble prediction system (EPS) based on AROME-MetCoOp. MEPS is used as weather forecast at the Norwegian Meteorological Institute, the Swedish Meteorological and Hydrological Institute (SMHI) and the Finnish Meteorological Institute (FMI), [Køltzow, 2017, Müller et al., 2017].

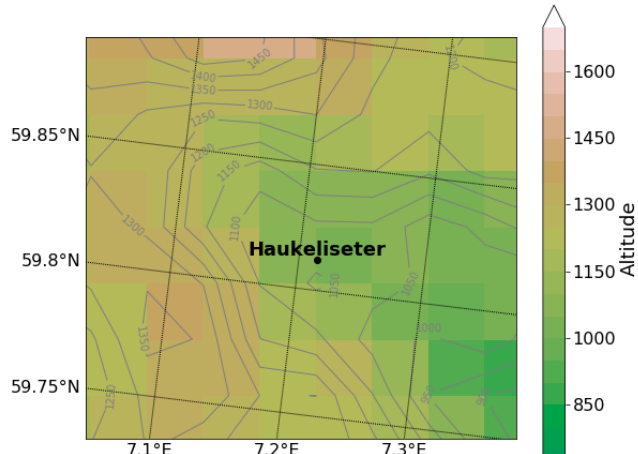
**Include the difference between AROME-MetCoOp and MEPS**

### 2.5.1 METCOOP ENSEMBLE PREDICTION SYSTEM - MEPS

In principle, MEPS is a short-term weather forecast consisting of a ten ensemble member forecast system with 66 h prediction time and a horizontal resolution of 2.5 km and 65 vertical levels. One of the members is the deterministic forecast where the other nine present the perturbed state of the deterministic forecast. The initialisation of each member is performed at 0 UTC, 6 UTC, 12 UTC and 18 UTC [MetCoOp Wiki, 2017].

Forecast data saved for the deterministic and first ensemble member have a time resolution of one hour for 66 h. The other eight members have values every three hours for up to 48 h forecast time.

Figure 2.1.1a shows the MEPS model domain and its elevation as it was operational for December 2016. It covers



the Nordic Countries including open water such as the Atlantic Ocean, the North and the Baltic Sea. A representation of the horizontal resolution zoomed on the Haukeliseter site is shown in Figure 2.5.1. Haukeliseter is surrounded by a complex terrain with mountains up to 1500 m to the west and the north and the more open terrain to the south-east.

The centre of the model is approximately at 63.5° N, 15° E. The horizontal grid points are projected on a Lambert projection to receive the same area size of each grid cell. The regional model MEPS receives initial and boundary conditions from ECMWF-IFS (European Centre for Medium-Range Weather Forecasts Integrated Forecasting System) before it can produce forecasts [Müller et al., 2017]. The horizontal resolution of the parent ECMWF grid is 9 km [Homleid and Tveter, 2016]. The ECMWF-IFS forecasts are used 6 h prior to the actual cycle in MEPS. Since initial conditions such as observations have uncertainties as well as the model has mistrust, and the own climatology needs to be approached, a model has to stabilize before the simulations can be trusted. The spin-up time varies depending on the quality of the initial and boundary conditions.

Vertical hybrid coordinates are terrain-following and are mass-based, [Müller et al., 2017]. How the vertical hybrid coordinates are transformed into layer thickness or height is described in Section 2.6.1. Furthermore, MEPS underlies non-hydrostatic dynamics, Met-CoOp Wiki [2017].

The representation of snow is covered by a modification of the three-class ice parametrization (ICE3) scheme. Where liquid-phase processes are separated from slow ice-phase processes and described in Section 2.5.2. To model the snow cover an one-layer atmosphere model scheme is implemented. This includes three variables such as: snow water equivalent (SWE), snow density, and snow albedo [Müller et al., 2017].

As synoptic observations are included in the model the snow-depth predictions underlay a special performance. Observations of snow-depth are only available at 6 UTC and 18 UTC, therefore is the snow analysis only performed twice daily [Homleid and Tveter, 2016,

Müller et al., 2017].

### 2.5.2 MESO-NH AND THE ICE3 SCHEME

The physical parametrization within AROME is based on the French research communities' mesoscale non-hydrostatic atmosphere model (Meso-NH). The microphysical scheme in the Meso-NH atmospheric simulation system is based on the ICE3 scheme. The purpose of the scheme is to model as correctly as possible the ice phase in the atmosphere [Pinty and Jabouille, 1998]. McCumber et al. [1991] concluded from their case study, that at least three different ice categories are necessary to cover most precipitation but that applications might be case specific. According to the Meteo France [2009] documentation, the ice phase microphysical scheme must include:

$\mathbf{r}_i$ : pristine ice phase

$\mathbf{r}_s$ : snowflake type from lightly rimed large ice crystals or dry clusters, and

$\mathbf{r}_g$ : heavily rimed crystals, such as graupel, frozen drops or hail

Within the ICE3 scheme no distinction between hail and graupel exists and therefore is the physical discrimination in the growth mode of graupel and hail is neglected.

To achieve snow water content within MEPS the total number concentration, slope parameter, mass diameter and the particle size distribution have to be determined. According to Caniaux et al. [1994] follows the particle size distribution the Marshall-Palmer distribution similar to Equation (2.4.2). The goal is to use a varying number concentration  $N_0$  dependent on the ice category. The study has shown that  $N_0$  can be assumed with

$$N_0 = C\lambda^x \quad (2.5.1)$$

$$\log_{10} C = -3.55x + 3.89$$

where  $C$  and  $x$  depend on the ice category and represent the relation between each other in Equation (2.5.1).

The ice water content for primary ice, snowflakes and rimed crystals is then be assumed to be similar to Equation (2.4.7), but the integration limits range from zero to infinity and mass, and particle size distribution are dependent on the diameter of the particle. The

mass diameter and particle size distribution (Equations (2.5.2) and (2.5.3)) are represented depending on the ice category shown in Table 2.5.1

$$m(D) = aD^b \quad (2.5.2)$$

$$n(D) = N_0 g(D) \quad (2.5.3)$$

and  $g(D)$  to be the generalised Gamma function

$$g(D) = \frac{\alpha}{\Gamma(\nu)} \lambda^{\alpha\nu} D^{\alpha\nu-1} \exp(-(\lambda D)^\alpha) \quad (2.5.4)$$

with  $\alpha$ ,  $\nu$  the shape and tail dispersion parameters and  $\Gamma(\nu)$  the gamma function.

After following the above equations including Equation (2.4.7) the slope parameter  $\lambda$  can be generated with  $G(B)$  the gamma function.

$$\lambda = \left( \frac{\text{SWC}}{aCG(b)} \right)^{\frac{1}{x-b}} \quad (2.5.5)$$

**Table 2.5.1:** Characterization parameters from primary ice ( $r_i$ ), snowflakes ( $r_s$ ) and rimed crystals ( $r_g$ ). Values are based on the references in [Meteo France \[2009\]](#) and in [Pinty and Jabouille \[1998\]](#).

	$r_i$	$r_s$	$r_g$
$\alpha, \nu$	3.3	1.1	1.1
$a$	0.82	0.02	196
$b$	2.5	1.9	2.8
$c$	800	5.1	124
$d$	1.0	0.27	0.66
$C$		5	$5 \times 10^5$
$x$		1	-0.5

[Meteo France \[2009\]](#) documentation suggests starting the microphysics in the ICE3 scheme with 'slow' processes such as homogeneous and heterogeneous nucleation (HON, HEN), vapour deposition of snow and graupel particles (DEP), aggregation (AGG) and auto conversion (AUT), for ice processes right side in Figure 2.5.2. The second step is to initiate the

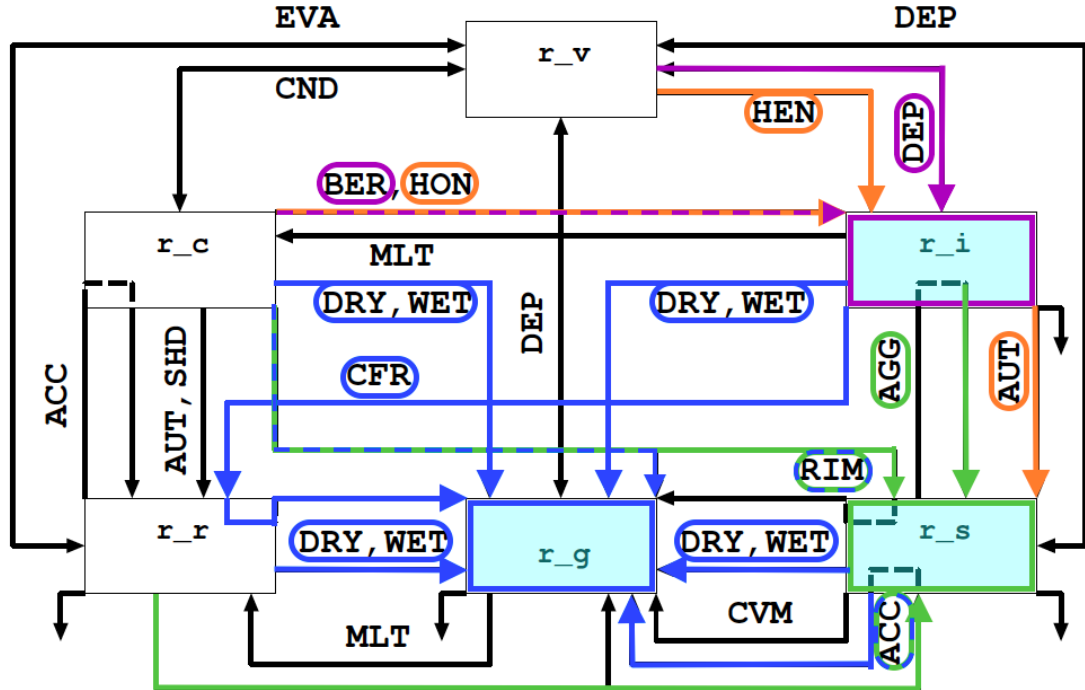


**Figure 2.5.2:** Microphysical processes for mixed phase clouds in the ICE3 scheme adapted from Meteo France [2009]. In orange the initiation processes for primary ice  $r_i$  and snowflakes  $r_s$ . The growing processes of  $r_i$  is shown in purple and for  $r_s$  in green. Graupel particles,  $r_g$ , grow from existent particles and the processes are shown in blue.

warm processes left side in Figure 2.5.2. Then include the aggregation and conversion-melting (CVM) for snowflakes and contact freezing of raindrops (CFR). Add AGG and melting for graupel (MLT), and then the melting from pristine ice and the Wegener-Bergeron-Findeisen (BER) effect and lastly the sedimentation terms.

Figure 2.5.2 shows the summary of the microphysical processes for mixed phase clouds. The study focuses mostly on solid precipitation particles and therefore only the initiation and growth of pristine ice crystals  $r_i$ , snowflakes  $r_s$ , and rimed crystals  $r_g$  is presented.

Following Pinty and Jabouille [1998] and Figure 2.5.2 it can be seen how AROME performs the ice production. Orange lines in Figure 2.5.2 show the initiation of pristine ice crystals and snowflakes. In purple the growth mechanisms of  $r_i$  (BER, DEP). Green lines demonstrate the expansion of the snowflakes (RIM, AGG, ACC). Graupel ( $r_g$ ) forms as an effect of heavy riming (RIM), by collision of larger raindrops with snowflakes (ACC), by

WET/DRY growth or by contact freezing of raindrops (CFR). All graupel growth processes are indicated by blue lines in Figure 2.5.2, were hail formation is included.

### 2.5.3 ADJUSTMENT OF ICE3 INSIDE AROME-METCoOP

Since the ICE3 scheme showed some weaknesses for the winter month, Müller et al. [2017] introduced some modifications. During cold conditions the ICE3-scheme showed too low temperature at two meter, too much ice fog and all year long was the occurrence of cirrus overestimated. After implementing the modifications described in Müller et al. [2017] the two meter temperature bias was reduced as well as an improvement of low-level clouds was shown. A negative aspect of these adjustments was that the occurrence of fog increased.

## 2.6 NUMERICAL DATA TRANSFORMATION

The following section will describe how the different variables where processed to achieve a comparison between the retrieved values and the forecast model output.

### 2.6.1 LAYER THICKNESS IN MEPS

To compare the measurements from the surface with the MEPS data, the closest grid point to Haukeliseter, is used.

MEPS has a vertical resolution in hybrid sigma pressure coordinates, were one is at the surface and decreases with height. To calculate the actual vertical pressure in Pa, a formula is provided in the OPeNDAP Dataset of `meps_full_2_5km_*.nc` by the Norwegian Meteorological Institute [2016].

$$p(n, k, j, i) = a_p(k) + b(k) \cdot p_s(n, j, i) \quad [\text{Pa}]. \quad (2.6.1)$$

$p_s$  is the surface air pressure in Pa, and information about the variables  $a_p$ ,  $b$  are not given from the access form. [Find reference for sigma-hybrid coordinate transformation equation.](#)

The next step was to convert pressure-levels into actual heights by the use of the hypsometric equation. Here, the air temperature in model levels is used to calculate the mean

temperature of each layer.

$$\bar{T} = \frac{\frac{p_1}{p_2} \int_{p_1}^{p_2} T \partial \ln p}{\int_{p_1}^{p_2} \partial \ln p} \quad [\text{K}] \quad (2.6.2)$$

For the numerical integration, the Simpson rule was used, which is a build-in function in Python.

[Martin \[2006\]](#) presents steps of differentiating the hypsometric equation by using the virtual air temperature. But when the atmospheric mixing ratio is large, will the virtual temperature only be 1 % larger than the actual air temperature. Since the error is little calculations are done with the provided air temperature in model levels.

The thickness,  $\Delta z$ , of each layer is then be found by using the hypsometric equation from [Martin \[2006\]](#) and the previously calculated mean temperature (Equation (2.6.2)):

$$\Delta z = z_2 - z_1 = \frac{R_d \bar{T}}{g} \ln \left( \frac{p_1}{p_2} \right) \quad [\text{m}] \quad (2.6.3)$$

where  $R_d$  is gas constant for dry air with a value of  $287 \text{ J kg}^{-1} \text{ K}^{-1}$ , standard gravity  $g = 9.81 \text{ m s}^{-2}$ .  $p_1$  and  $p_2$  are the pressure levels at lower and higher levels, respectively ( $p_2 < p_1$ ). To gain the respective height of each pressure layer,  $\Delta z$  is summed.

## 2.6.2 SNOW WATER CONTENT

To get a valid comparison between the SWC from the optimal estimation retrieval and the results from MEPS, the SWC is averaged over each hour. Taking the model initialisation of MEPS at 0 UTC the model produces forecast values at 0, 1, 2, ..., 22, 23, ..., 66 UTC. To approach hourly mean values from the retrieval SWC an average over 30 min prior and 29 min after each full hour is performed. This leads to a match of the average value at the same time as from MEPS.

Since MEPS has a higher vertical resolution than the optimal estimation snowfall retrieval each vertical profile of SWC is averaged every 200 m. To accomplish the same vertical resolution only values above 100 m are used to start at the same range height as given from the MRR (Section 2.3.2).

Within the output from MEPS snow water content does not exist for each model layer.

Hence the calculation of the SWC is performed by using the three solid precipitation categories given in MEPS. Namely the instantaneous mixing ratio of snowfall ( $r_s$ ), graupel fall ( $r_g$ ) and the atmosphere cloud ice content ( $r_i$ ). The mixing ratios are represented in  $\text{kg kg}^{-1}$  and a transformation to  $\text{gm}^{-3}$  is performed. Densities in each model level ( $\rho_{ml}$ ) are calculated and then multiplied with the sum of the solid precipitation mixing ratio.

$$\rho_{ml} = \frac{p_{ml}}{R_d T} \quad [\text{kg m}^{-3}] \quad (2.6.4)$$

$$SWC_{ml} = \rho_{ml} \cdot (r_s + r_g + r_i)_{ml} \cdot 10^6 \quad [\text{gm}^{-3}]. \quad (2.6.5)$$

### 2.6.3 SNOW WATER PATH

The snow water path (SWP) is the vertically integrated value of the averaged SWC (Equations (2.4.7) and (2.6.5)), where the numerical Simpson's integration is applied.

$$\int_{h_0}^{h_1=3000\text{m}} SWC(h) dh \approx \frac{h_1 - h_0}{6} \left[ SWC(h_0) + SWC(h_1) + 4SWC\left(\frac{h_0 + h_1}{2}\right) \right] \quad [\text{gm}^{-2}] \quad (2.6.6)$$

The snow water path is a measure of the weight of ice particles per unit area. It indicates the total amount of ice in the atmosphere.

### 2.6.4 ENSEMBLE MEAN AND COEFFICIENT OF VARIATION

#### Check literature of meaning

The ensemble mean is the average of all ten ensemble members of MEPS.

$$\bar{x} = \frac{\sum_{i=1}^n x_i}{N} \quad (2.6.7)$$

which is the standard deviation of the ten ensemble members divided by the mean of all ensemble members. This coefficient gives the possibility to compare the SWC results for different days with different values. The coefficient of variation shows the variation around the center or control run. The standard deviation is defined as:

$$\sigma = \sqrt{\frac{\sum_{i=1}^n (x_i - \bar{x})^2}{N-1}} \quad (2.6.8)$$

which follows for the coefficient of variation:

$$CV = \frac{\sigma}{\bar{x}} \quad (2.6.9)$$

### 2.6.5 MEAN ERROR AND MEAN ABSOLUTE ERROR

The mean error for each ensemble member is calculated with:

$$ME = \frac{\sum_{i=1}^n MEPS_{ens} - DoFe_{obs}}{N} \quad (2.6.10)$$

where  $MEPS_{ens}$  represents the value of each ensemble member and  $DoFe_{obs}$  defines the observation from the double fence. For the mean absolute error follows then:

$$MAE = \frac{\sum_{i=1}^n |MEPS_{ens} - DoFe_{obs}|}{N} \quad (2.6.11)$$

### 2.6.6 PERCENT DIFFERENCE AND AVERAGE DIFFERENCE

The percentage difference presented in the results (Table 4.2.2 and add for MEPS) are calculated by:

$$\%Difference = \frac{SF - DoFe_{obs}}{DoFe_{obs}} \times 100 \quad (2.6.12)$$

$SF$  presents the snowfall from the retrieval or the MEPS ensemble forecast. The average is then taken from all % Difference values to see the difference of the Christmas storm 2016.

# CHAPTER 3: ANALYSIS OF THE CHRISTMAS STORM 2016

Extreme storm Urd was chosen for an in depth examination for a number of intriguing reasons: i) the MEPS forecasting system had recently become the operational model platform for Met-Norway, ii) the Haukerlister site is a WMO sanctioned weather station with single and double fence rain gauge measurements, iii) additional instruments were placed at the site for the winter 2016/2017 season allowing for the vertical profiling of snow properties and snowfall accumulation, and iv) the unique temporal evolution of the precipitation properties during the event.

A preliminary analysis identified periods of both good agreement of snow accumulation measurements by MEPS in comparison to the ground observations, as well as periods of overestimation by MEPS. The above factors make for an interesting study to assess and better understand the usefulness of the measurements in question.

The next sections will provide a definition of an extreme weather event, a description of the weather maps that were utilized, and a presentation of the synoptic scale evolution of the storm.

Prior to the analysis, each weather maps' purpose will be presented to understand the connections between them. All the weather maps are generated using data from ECMWF operational model Cycle 43r1. The analysis consists of 137 model levels and to reduce computational costs is it reduced to the *octahedral reduced Gaussian grid* and then interpolated to a N640 Gaussian grid.

Between the pole and the equator are 640 lines of latitude equally symmetric spaced. This follows 1280 latitude lines for each hemisphere. The resolution along the longitude is  $90^\circ/640$  lines with points getting closer with increasing latitude. This follows a total

number of grid points of  $8 \cdot 640^2$  [Dando, 2016].

### 3.1 EXTREME WEATHER

'Extreme weather' is a meteorological term, associated with the extent of a weather type. The Norwegian Meteorological Institute declares an extreme event, if strong winds, large amounts of precipitation and large temperature changes are expected before the event occurs. As well as a large avalanche risk is present and coastal areas are influenced by extremely high-water levels. Generally, an event is divided into four phases that it can be called extreme [Pedersen and Rommetveit, 2013].

**Phase A:** *Increased monitoring before the possible extreme weather.* The meteorologists give special attention to the weather situation. At this point it is not certain, that there will be an extreme weather event.

**Phase B:** *Short-term forecasts.* It is decided, that there will be an extreme event. The forecasts are more detailed, and updates will be published at least every six hours. The event will get a name.

**Phase C:** *The extreme weather is in progress.* The meteorologists send out weather announcements at least every six hours.

**Phase D:** *The extreme weather event is over. Clean-up and repairs are in progress.* When the extreme weather is over the public is notified and information about the upcoming weather and clearing work is given.

The Christmas storm was deemed an extrme event by the Met-Norway, named Urd [Olsen and Granerød, 2017]. The average wind along the coast of Western Norway reached hurricane strength (observed:  $40 \text{ m s}^{-1}$  to  $55 \text{ m s}^{-1}$ ). In South and Eastern Norway, west to north-west winds between  $25 \text{ m s}^{-1}$  to  $40 \text{ m s}^{-1}$  were measured. At Haukeliseter, 136.4 mm of precipitation were measured from 21 to 27 December 2016. The event was just above the limit of been called an extreme weather event.

To understand which damage a storm can have, Færaas et al. [2016] released a table to associate wind strength with damage (see Table 3.1.1).

**Table 3.1.1:** Damage related to wind speed, from Færaas et al. [2016].

slight storm	$20.8 \text{ ms}^{-1} - 24.4 \text{ ms}^{-1}$	Large trees sway and hiver. Roofs can blow down.
full storm	$24.5 \text{ ms}^{-1} - 28.4 \text{ ms}^{-1}$	Trees are pulled up with clutter. Big damages to houses.
strong storm	$28.5 \text{ ms}^{-1} - 32.6 \text{ ms}^{-1}$	Extensive damage.
hurricane	$>32.6 \text{ ms}^{-1}$	Unusually large destruction.

### 3.2 DYNAMIC TROPOPAUSE MAP

The dynamic tropopause maps (DT), presented herein are comprised of the potential temperature (shading) and wind barbs [ $\text{ms}^{-1}$ ] on the two PVU surface (one PV unit =  $10^{-6} \text{ m}^2 \text{s}^{-1} \text{Kkg}^{-1}$ ), and the 925–850 hPa averaged relative vorticity (black contours - every  $0.5 \times 10^{-4} \text{ s}^{-1}$  only positive values are plotted). An example is presented in ???. High (low) values of potential temperature represent and elevated (suppressed) tropopause. Regions with a large horizontal gradient of potential temperature indicate a steeply-sloping tropopause that is associated with an enhanced pressure gradient force and winds. The low-level averaged relative vorticity is plotted to provide a 3-dimensional (in the vertical) picture of the atmosphere. It is useful for identifying cyclone centres and attendant frontal boundaries.

The 925 –850 hPa layer-averaged surface relative vorticity is shown in black contours, every  $0.5 \times 10^{-4} \text{ s}^{-1}$ . It represents the rotation of a fluid. **Does the relative vorticity need more explanation?**

Along the Rossby-Wave-Guide **Define what I mean by Rossby-Wave-Guide**, troughs and ridges are seen which can be combined with the surface relative vorticity to understand the vertical dynamic interaction in the atmosphere. In case of a westward tilt between the surface cyclone and an upper level through an intensification of the surface cyclone is more likely to occur.

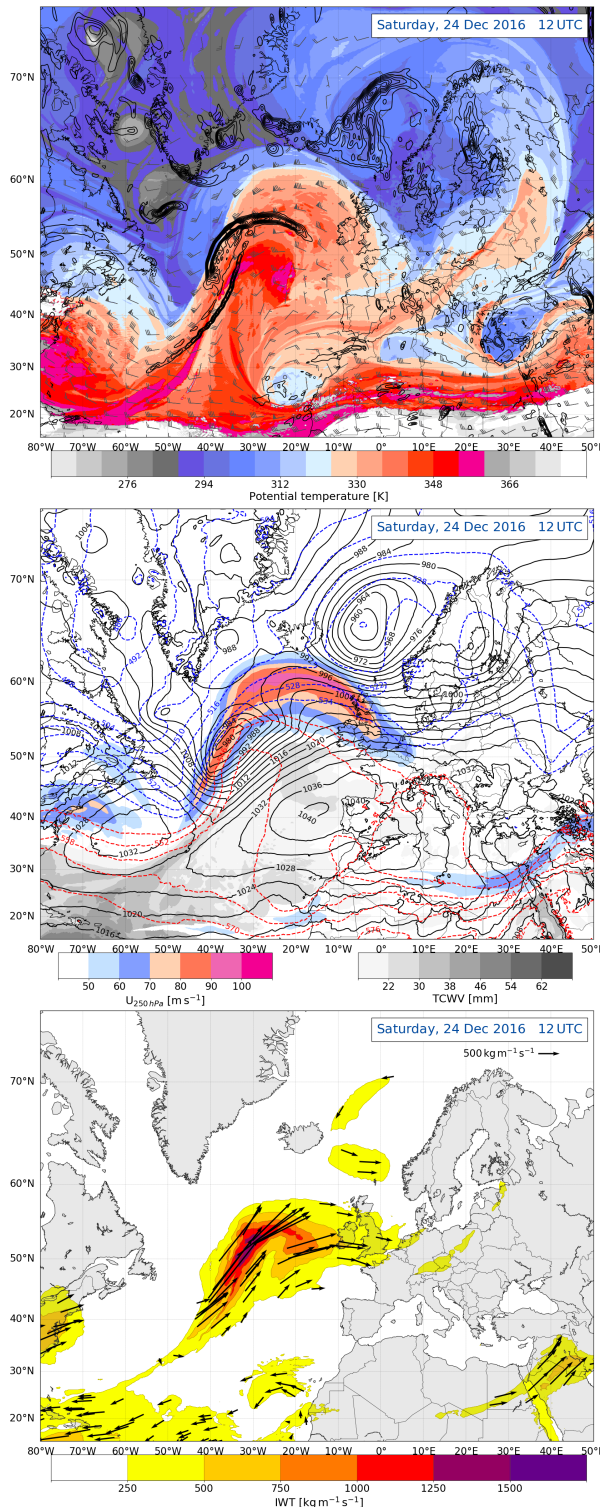


Figure 3.2.1: ECMWF analysis on 24 December 2016 at 12 UTC.

**a:** Dynamic tropopause analysis map at 2 PVU. Potential temperature [K] at the 2 PVU surface, shaded according to the colour bar. Total wind, barbs [ $\text{ms}^{-1}$ ], and 925 -- 850 hPa layer-averaged surface relative vorticity (black contours, every  $0.5 \times 10^{-4} \text{ s}^{-1}$ ).

**b:** Jet, thickness, mean sea level pressure, and moisture synoptic analysis. 250 hPa wind speed, shaded according to the colour bar, [ $\text{m s}^{-1}$ ]. 1000 – 500 hPa thickness, dashed contours every 6 dam, MSLP, black contours every 4 hPa, total column water vapour [mm], shaded according the grey scale.

**c:** Atmospheric river analysis map. IVT, shaded according to the colour bar [ $\text{kg m}^{-1} \text{s}^{-1}$ ]. Vectors, indicating the direction and magnitude of the IVT.

### 3.3 THICKNESS, SEA LEVEL PRESSURE, TOTAL PRECIPITABLE WATER, AND WIND AT 250 hPa

A complementary view of the 3-dimensional structure of the atmosphere is also presented: 250 hPa wind speed (color shading,  $\text{m s}^{-1}$ ), mean sea level pressure (black contours, hPa), 1000–500 hPa thickness (dashed contours) and the total precipitable water (black-white shading, mm). See Figure 3.2.0b for an example.

The dashed, coloured contours show the vertical thickness between the 1000 hPa and 500 hPa surface, every 6 dam. The thickness between two pressure levels can be interpreted via the hypsometric equation (Equation (2.6.3)), which equates the thickness to the mean temperature of the layer in question. In a relative sense, a larger thickness indicates a warmer air mass. In addition, strong horizontal gradients in the thickness field can be related to frontal boundaries. Specific to the discussion herein, the thickness field is also provides useful information regarding the form of precipitation (rain, snow).

Analysis of the mean sea level pressure can be used to identify cyclones and anticyclones at the surface as well as provide supplementary information regarding frontal boundaries. The total precipitable water is a measure of the column integrated moisture. The 250 hPa wind speeds are used to identify strong upper-level flow (i.e. the jet stream) and can be directly compared to the DT map. It represents an instantaneous measure of moisture in time and space, which can be useful when assessing the amount of moisture that may fall as precipitation in future time steps.

### 3.4 INTEGRATED VAPOUR TRANSPORT

Figure 3.2.0c shows coloured contours of the integrated vapour transport (IVT) in  $\text{kg m}^{-1} \text{s}^{-1}$ , where warmer colours indicate higher IVT. Stream vectors indicate the direction and intensity of the IVT flow. An atmospheric river is characterised if the integrated vapour transport shows values higher than  $250 \text{ kg m}^{-1} \text{s}^{-1}$  and a continuous region larger than 2000 km [Rutz et al., 2014].

An atmospheric river (AR) is a filament structure of intense moisture transport from the tropics to higher latitudes. Heavy precipitation can be associated with it, because the air is warm and moist. This can often be observed at mountain ranges at west coasts such as in

Norway [include reference here](#). Due to orographic lifting will the moisture be released and follow high amounts of precipitation.

The integrated vapour transport (IVT) was calculated from the ECMWF data as followed:

$$IVT = \frac{1}{g} \int_{p_{sfc}}^{100 \text{ hPa}} q \mathbf{V} dp \quad [\text{kg m}^{-1} \text{s}^{-1}] \quad (3.4.1)$$

where  $g$  is the standard gravity,  $q$  the specific humidity, and  $\mathbf{V}$  the total wind vector at each pressure level  $p$ . The numerical, trapezoidal integration is performed by using data from the surface pressure  $p_{sfc}$  to 850 hPa in 50 hPa intervals and from 700 hPa to 100 hPa in 100 hPa intervals.

Analysing integrated vapour transport maps is important, since extreme precipitation events in Norway are often influenced by moist, warm air advection from the tropics [Reference here!](#). Figure 3.4.1 show integrated vapour transport from the tropics to the midlatitudes, but it also presents that the occurrence of the atmospheric river was not the main factor, which led to intense precipitation during Christmas 2016. Since it showed not to be intense it will not be further discussed.

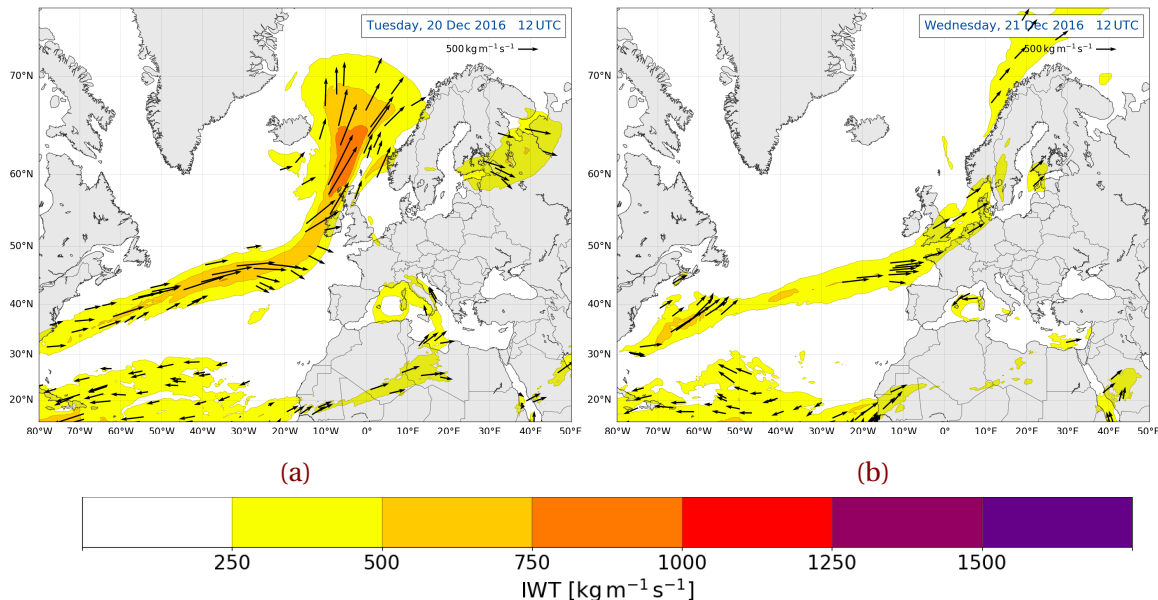


**Figure 3.4.1:** Atmospheric river analysis map, data from ECMWF. During 20 December 2016 to 27 December 2016. IVT, shaded according to the colour bar  $[\text{kg m}^{-1} \text{s}^{-1}]$ . Vectors, indicating the direction and magnitude of the IVT.

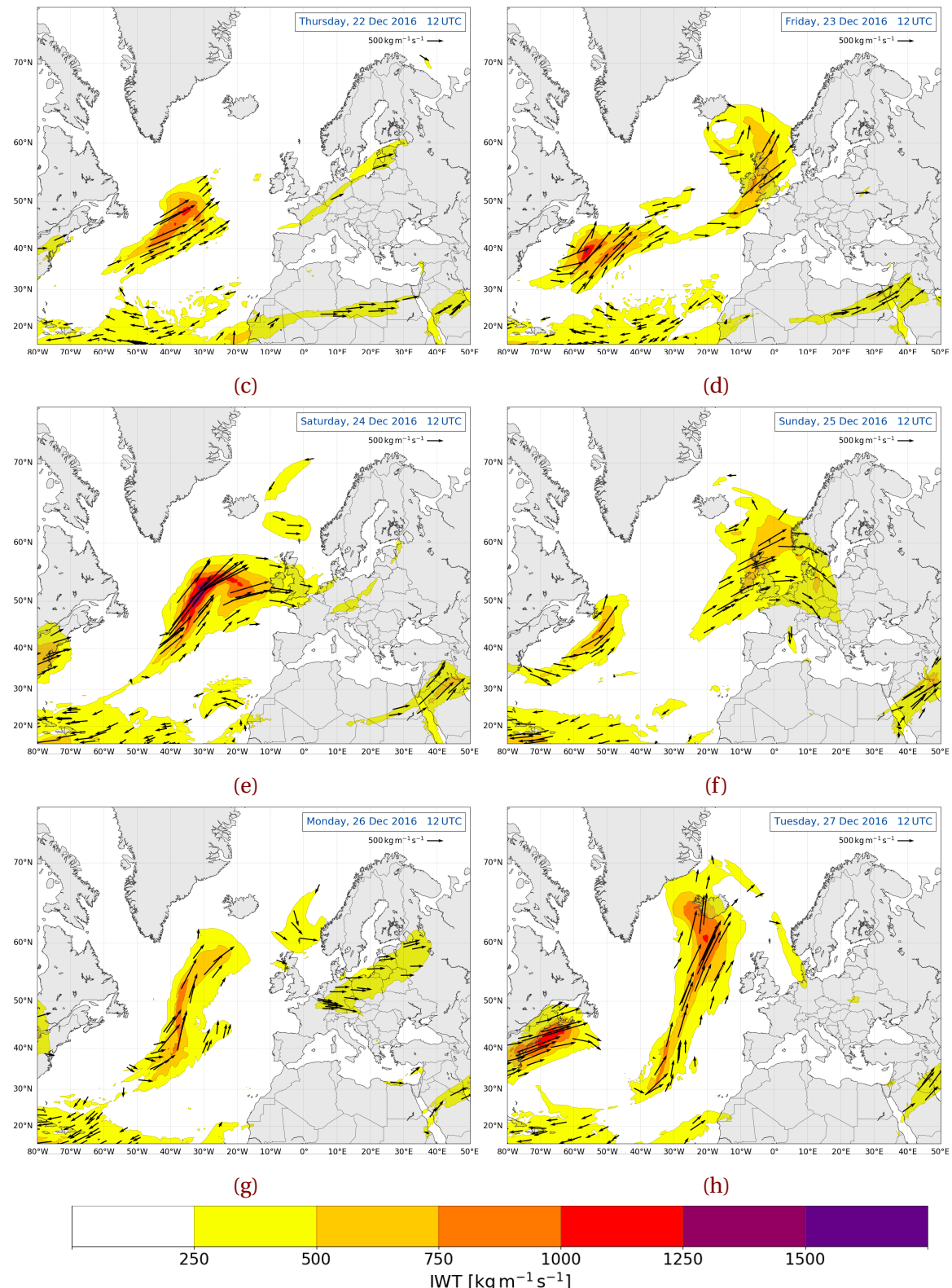
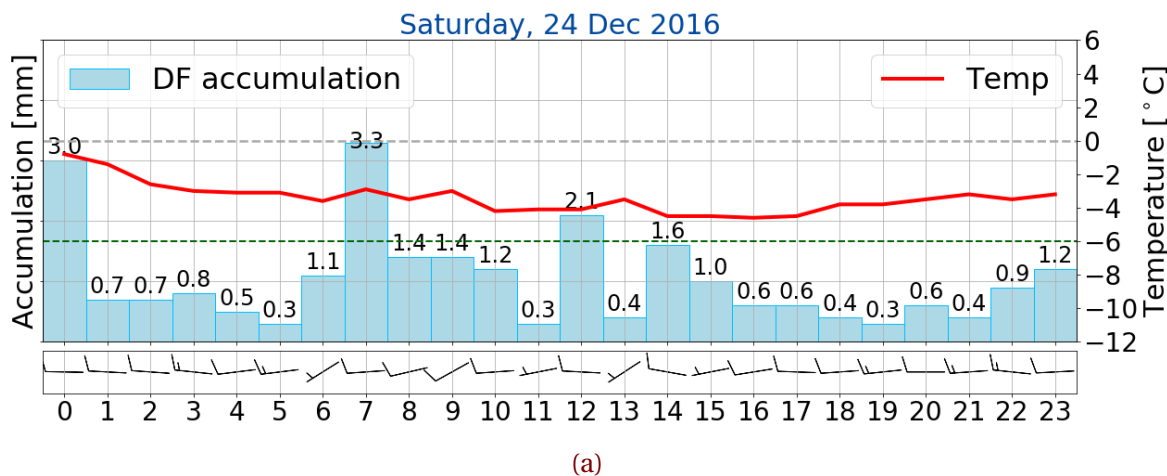


Figure 3.4.1: (Continued from previous page.)

### 3.5 OBSERVATIONS AT THE WEATHER MAST

If used here, then not in the weather situation, but keep the wind damage table. It is a primary goal of this work to relate the local weather observations from the WMO site at Haukeliseter to the synoptic scale structure and the additional measurements taken at Haukeliseter during the winter of 2016/2017.

Examples of the 60 min precipitation accumulation from the double fence rain gauge, 2 m air temperature, and wind observations are presented in Figure 3.5.1 to document the continuous precipitation at Haukeliseter during the extreme event. The temperature



(a)

Figure 3.5.1: Surface precipitation, temperature and wind observation from the weather mast at Haukeliseter on 24 December 2016. 60 min total accumulation [mm] in light blue as bar, temperature (red, [ $^{\circ}\text{C}$ ]), and wind as barbs [ $\text{m s}^{-1}$ ]. Gray dashed line indicates the freezing temperature and the green dashed line the 30-year climate mean temperature at  $-6^{\circ}\text{C}$ . Hourly processed data taken from [eklima \[2016\]](#).

evolution will be used to investigate possible changes in the type of precipitation. Snowfall is likely for temperatures up to  $2^{\circ}\text{C}$ . The intensity of the storm can be classified by the hourly averaged wind speed and direction as wind barbs in  $\text{m s}^{-1}$ . To understand which damage a storm can have, [Færaas et al. \[2016\]](#) released a table to associate wind strength with damage (see Table 3.1.1).

## 3.6 LARGE SCALE CIRCULATION

Some text to get a flow.

### 21 December 2016

The dynamic tropopause map in Figure 3.6.1b shows that Norway is influenced by a change of elevated tropopause to a suppressed tropopause during 20 December 2016 to 21 December 2016. Hence the potential vorticity changed from positive to negative at the tropopause and cold air stretches right over Norway. A good amount of moisture is transported from the low latitudes to high latitudes, influencing Norway's' west coast. This can be seen in the surface maps (Figure 3.6.1d) as well as in the atmospheric river maps (Figure 3.4.1b). The westerly flow in Figure 3.6.1d is conducive to orographic lifting. The precipitation was probably snow when having a look at the moisture content and the cold air. The change from warm air to cold air can also be observed in the time series of temperature in Figure 3.6.1f. And the westerly flow, combined with a good amount of vapour transport from the tropics led to orographic lifting and precipitation at the Haukeliseter site. At around 60° W a formation of a cyclone at the baroclinic zone can be implied.

### 22 December 2016

Twenty-four hours later the analysis shows from 22 December 2016 phasing between the surface relative vorticity and the baroclinic zone at 50° N in the DT. The centre of the surface low is directly located below the temperature gradient at the 2 PVU surface, hence this is good for synoptic lifting. Furthermore, the strongest baroclinicity is observed on the south west side of the surface low. The synoptic map of the geopotential thickness and the surface pressure show the beginning of the frontal boundaries in Figure 3.6.1h. At the same time shows the AR map, Figure 3.4.1c, large values just at the baroclinic zone, where the low pressure is beginning to form. **Help?! Does that lead to even more lifting in this area? Or does it just mean that the cyclone gets a good amount of moisture?!**. Norway is located in a cold area. The continues precipitation observed at Haukeliseter (Figure 3.6.1i) is associated with the westerly flow which is conducive to orographic lifting, and therefore

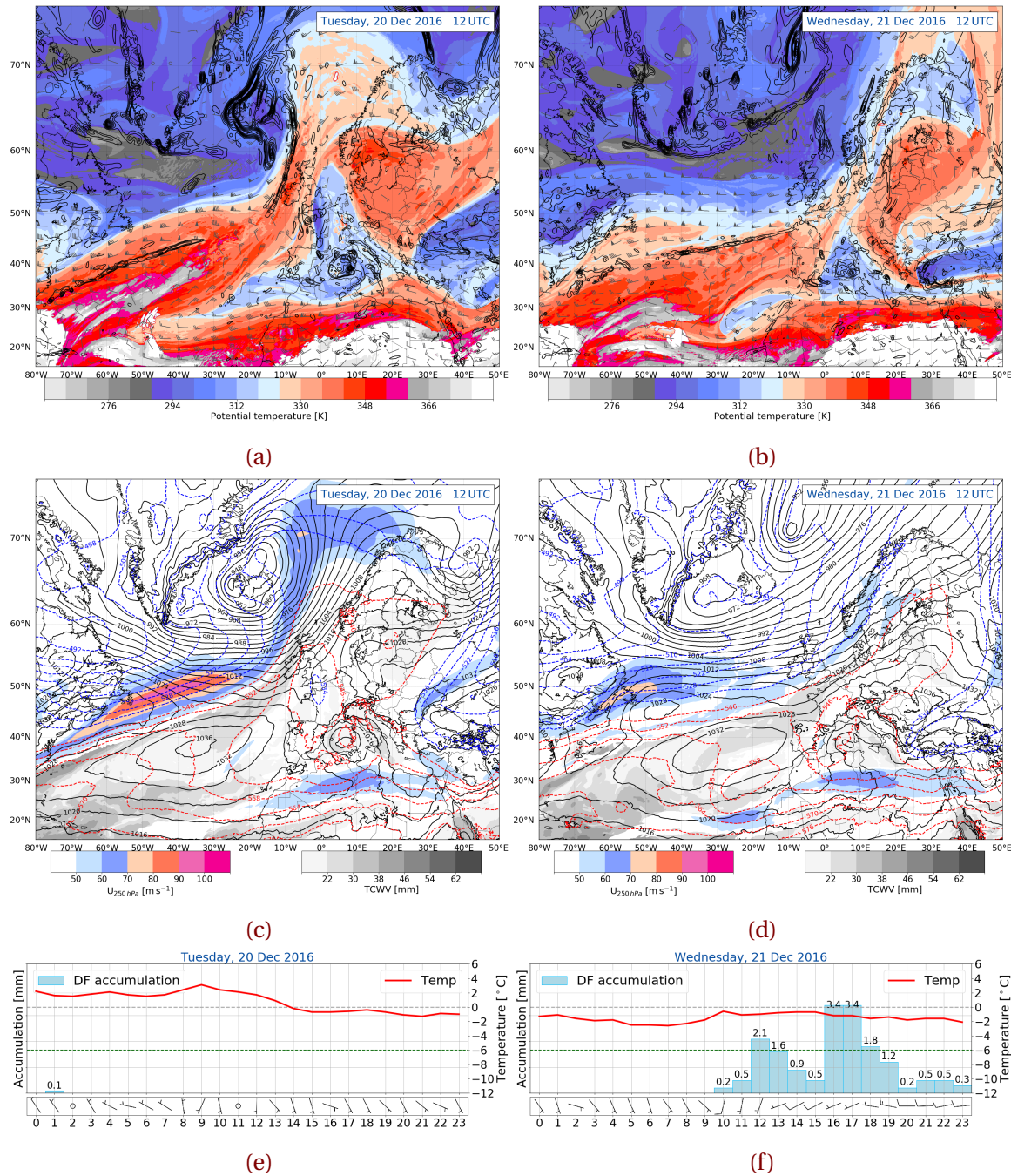


**Figure 3.6.1:** ECMWF analysis for dynamic tropopause as described in Section 3.2 and thickness map as evaluated in Section 3.3. Analysis is shown for 20 (a, c) and 21 December 2016 (b, d) at 12 UTC.

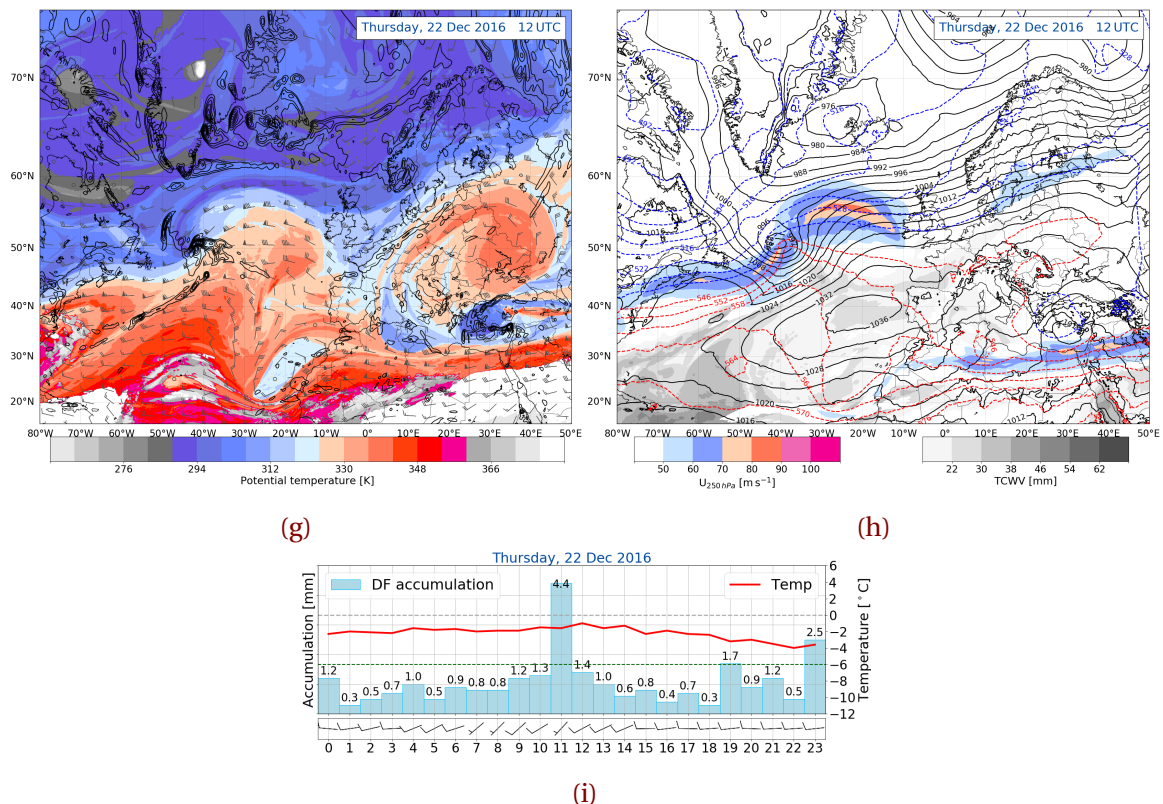


Figure 3.6.1: (Continued from previous page.) 22 December 2016 at 12 UTC.

moisture release.

### 23 December 2016

**Use the 12UTC and 18UTC analysis** The begin of the ridging on the 22 December 2016 is more pronounced 24 h later. The warmer air pushes away the cold air, which covered Norway. The low-pressure system moved north-east and lies south of Iceland. The occluded front of this system passes through Haukeliseter, which is why a temperature 'jump' observed at 14 UTC. After this, Southern Norway is influenced by the warm sector, monitored as a temperature increase. The AR, as well as the total column water vapour amount in Figure 3.4.1d and Figure 3.6.2c, respectively show the amount of moisture, transported from low latitudes.

At the same time forms a second cyclone at the baroclinic zone at 40° N. The atmospheric river map (Figure 3.4.1d) indicates a large amount of moisture at this latitude. Again, moist, warm air is conducive to intensify the surface cyclone. In addition, shows the DT map a phasing between the low-level vorticity and the upper level baroclinic zone.

### 24 December 2016

After the passage of the cold front over Norway, Scandinavia is within colder air (compare Figure 3.6.2f and Figure 3.6.2g for 24 December 2016). Over the Atlantic warmer air starts to push the colder air northward. **something something with the low-level vorticity and lifting; lifting at the right entrance region of the jet streak, and very high IVT.**

At Haukeliseter negative temperature up to  $-4^{\circ}\text{C}$  is observed, compare Figure 3.6.2h. The westerly flow is again conducive for orographic lifting and associated precipitation.

### 25 December 2016

**Use the 00UTC and 12UTC analysis** Twenty-four hours later the ridge is more pronounced and covers large parts of Norway. The surface low south-east of Iceland has built its frontal boundaries, which can be seen in the low-level vorticity of Figure 3.6.2i. The warm front lies west of Haukeliseter and starts to be observed at the measurement site (compare Figure 3.6.2m for 25 December 2016). Figure 3.4.1f indicating the integrated vapour transport shows that a lot of moisture is transported from the Atlantic, towards

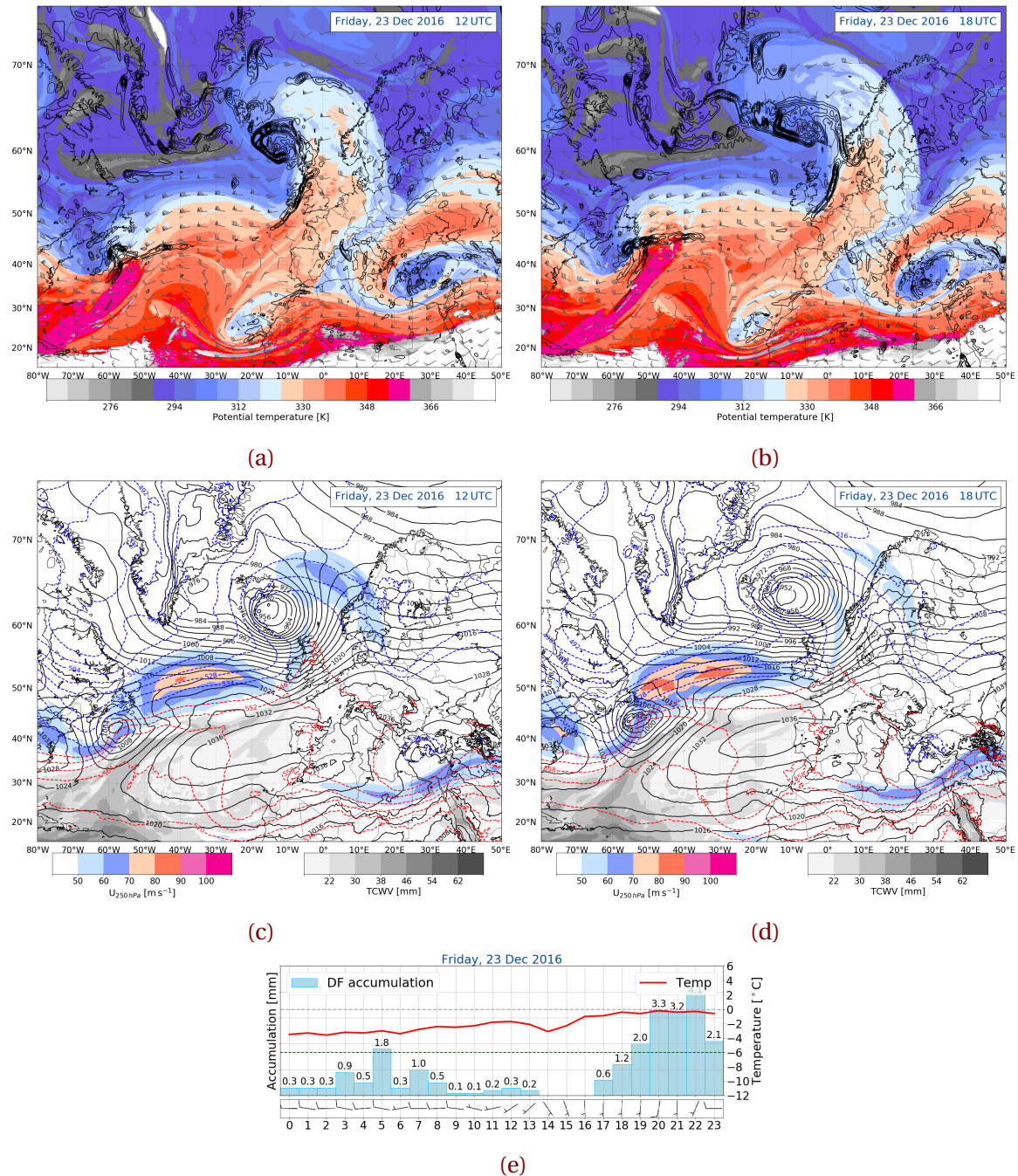


Figure 3.6.2: (Continued from previous page.) For 23 at 12 UTC (a, c) and at 18 UTC (b, d).

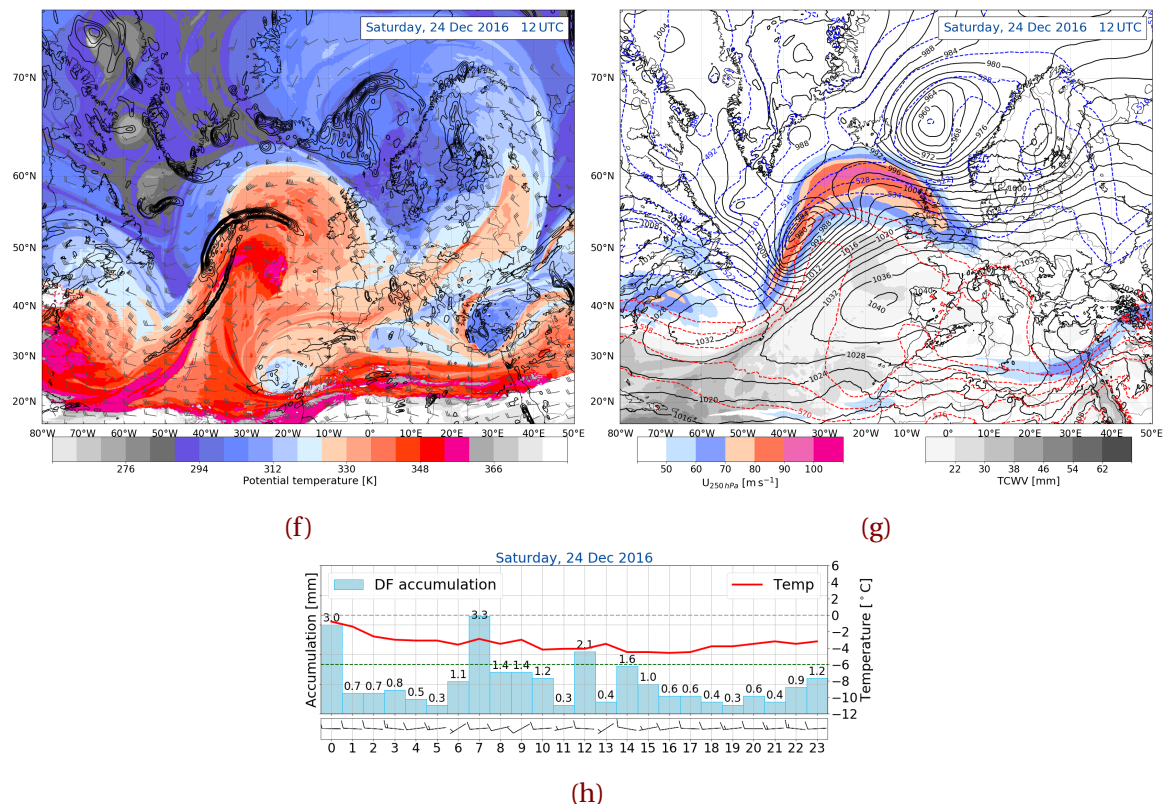


Figure 3.6.2: (Continued from previous page.) 24 December 2016 at 12 UTC.

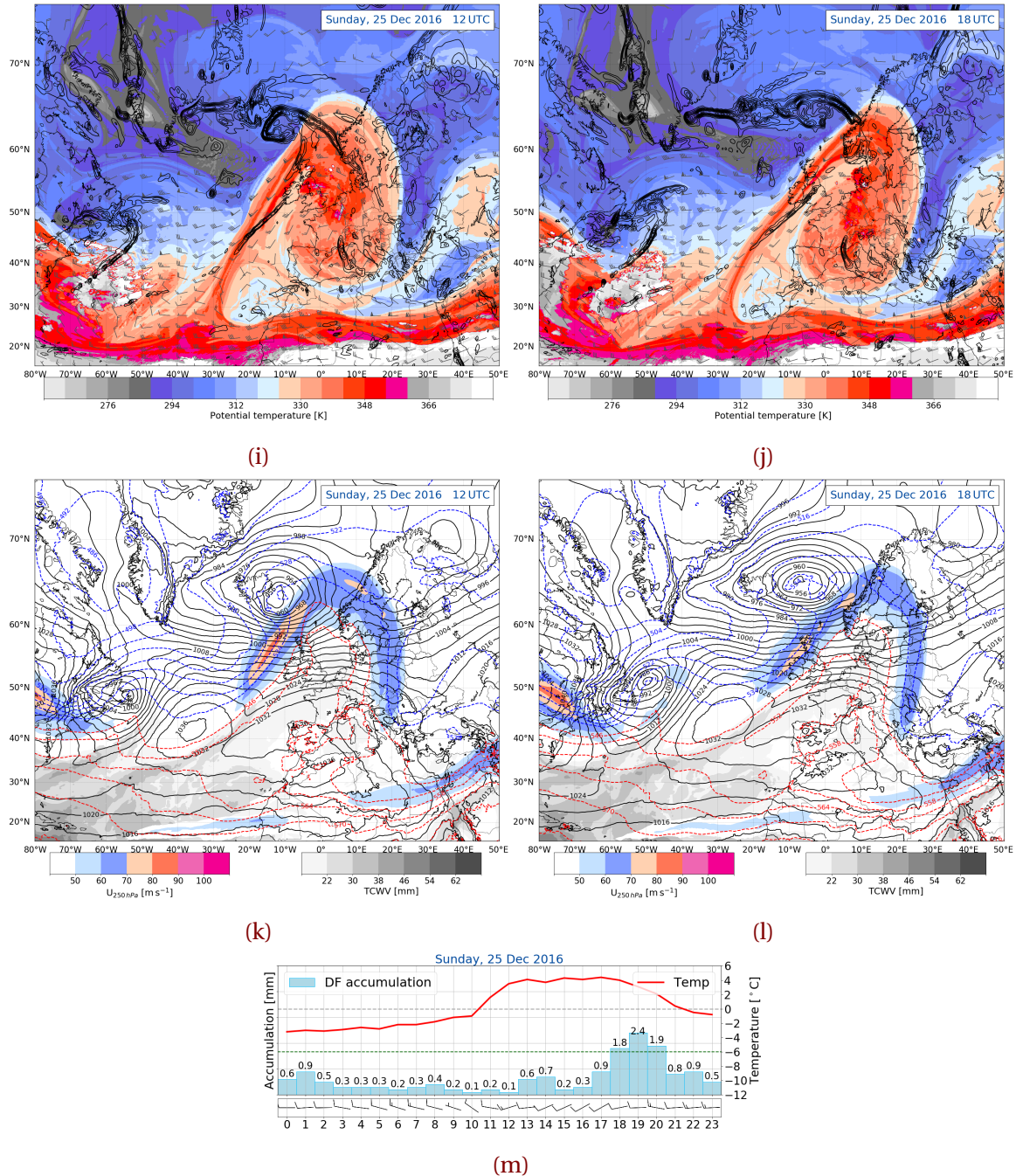


Figure 3.6.2: (Continued from previous page.) For 25 December 2016 at 12 UTC (i, k) and at 18 UTC (j, l).

Great Britain and south-western Norway. Together with the lifting at the surface boundary a sufficient amount of precipitation is observed.

Since the ridging brings moister (Figure 3.4.1f), warm air (Figure 3.6.2i) and Norway lies in a warm sector (Figure 3.6.2k) the assumption will be made, that the precipitation changed from solid to liquid.

### 26 December 2016

**Use the 12UTC and 18UTC analysis** Within the next twenty-four hours the cold front passed through (temperature change in Figure 3.6.2r for 25 December 2016 to 26 December 2016). Norway is covered in cold air (Figure 3.6.2n). The surface low-level indicates the occlusion of the cyclone and therefore a weakening. The wind is still from the west which is helpful for orographic lifting. The moisture content is still present but much weaker and smaller in extend. Since Norway is covered in cold air, the temperature is below zero and the precipitation had to be solid.

### 27 December 2016

The images of 27 December 2016 show that the storm passed and disappeared. Southern Norway lies in cold air (??), but on the right exit region of the jet ( $\rightarrow$  sinking motion of cold air), compare ???. A small amount of moisture is present (Figure 3.4.1h). Because of the wind change from west to north-west follows that orographic lifting is not present and the precipitation amount decreases at the end of the storm.

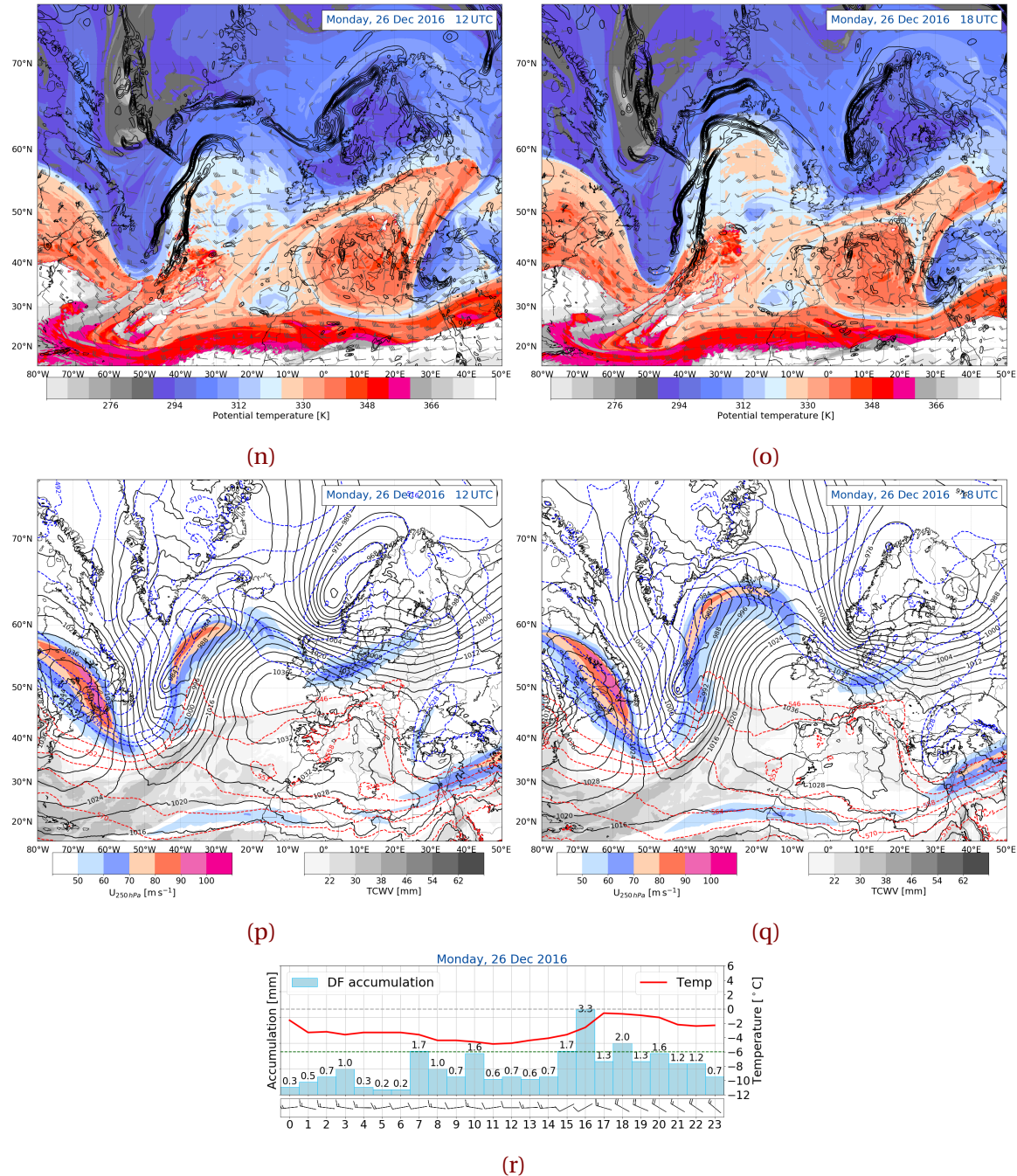


**Figure 3.6.2:** (Continued from previous page.) For 26 December 2016 at 12 UTC (n, p) and at 18 UTC (o, q).

# CHAPTER 4: HAUKELISETER: OBSERVATION AND MEPS COMPARISON

In this chapter the results of the surface observation, the optimal estimation retrieval and the regional mesoscale forecast model are presented. On the basis of the methodology described in Chapter 2 it should be evaluated if a regional mesoscale forecast model predicts the same synoptic patterns as observed at the measurement site. Also, vertical SWC forecasted by MEPS is being compared with the retrieved vertical SWC at Haukeliseter. Attention should be paid to the fact, that this study is unique. The motivation to compare regional model forecasts with vertical snowfall measurements resulted from a study by Joos and Wernli [2012]. They did sensitivity studies on the microphysical scheme of COSMO (COncsortium for Small-scale MODelling) and found that the storm development depends on the correct vertical placement of the precipitation inside a modeled storm. Vertical precipitation placement determines the vertical profile of latent heating, and hence the generation of potential vorticity which in return shows if a storm strengthens or weakens. Correct vertical precipitation observations can then help to correctly assess model vertical precipitation patterns.

This study will give a first insight into comparing snowfall model forecasts with observed snowfall, for one particular extreme event, the 2016 Christmas storm.

## 4.1 METEOROLOGICAL INVESTIGATION OF THE CHRISTMAS STORM 2016

One of the main factors, that made the Christmas 2016 storm so interesting is the fact that fronts passed over Norway during the six-day period. One aim of this thesis is to identify if large scale phenomena were observed at the measurement site and if MEPS predicted the same measured pressure, temperature, wind, and precipitation patterns during the extreme event.

### 4.1.1 SURFACE COMPARISON

The large scale weather situation was discussed in Section 3.6. It has shown, that two low pressure systems affecte Norway around Christmas 2016. Figure 4.1.1 display the observations and intialisations for pressure, temperature, wind, and precipitation on 21 to 27 December 2016.

A comparison between the surface observations at Haukeliseter and the ECMWF analysis of the dynamic tropopause and geopotential thickness maps show that frontal transitions occurred on three days during the 2016 Christmas storm, 23, 25, and 26 December 2016 (Section 3.6). These show in the measurements and MEPS ensemble forecasts on 23, 25, and 26 December 2016 (Figure 4.1.1).

Figure 4.1.1 shows the different parameters forecasts initialised at 0 UTC for 23, 25, and 26 December 2016, as well as the observations at the Haukeliseter measurement site. During all days the MEPS forecast seems to be able to predict similar pressure, temperature, wind, and precipitation as is observed. Overestimations are seen for wind speed and surface precipitation amount in Figure 4.1.1c, h, m, r, e, j, o, and t.

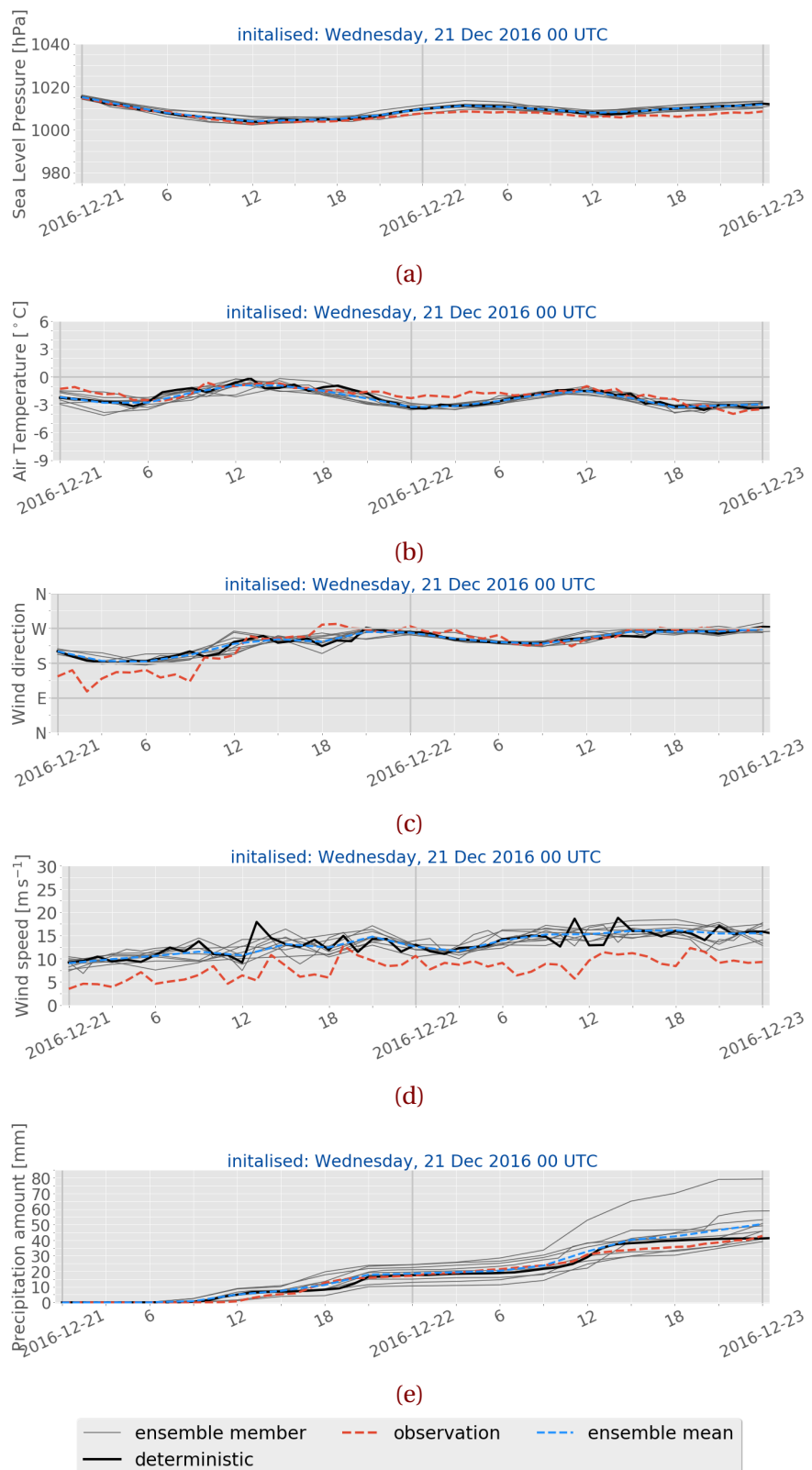


**Figure 4.1.1:** 48 h surface observations and MEPS ensemble forecasts initialised on 21 December 2016 at 0 UTC. Line representation according to the label. Upper to low panel: sea level pressure, 2 m air temperature, 10 m wind direction and speed, and precipitation amount. *Continued on next page.*

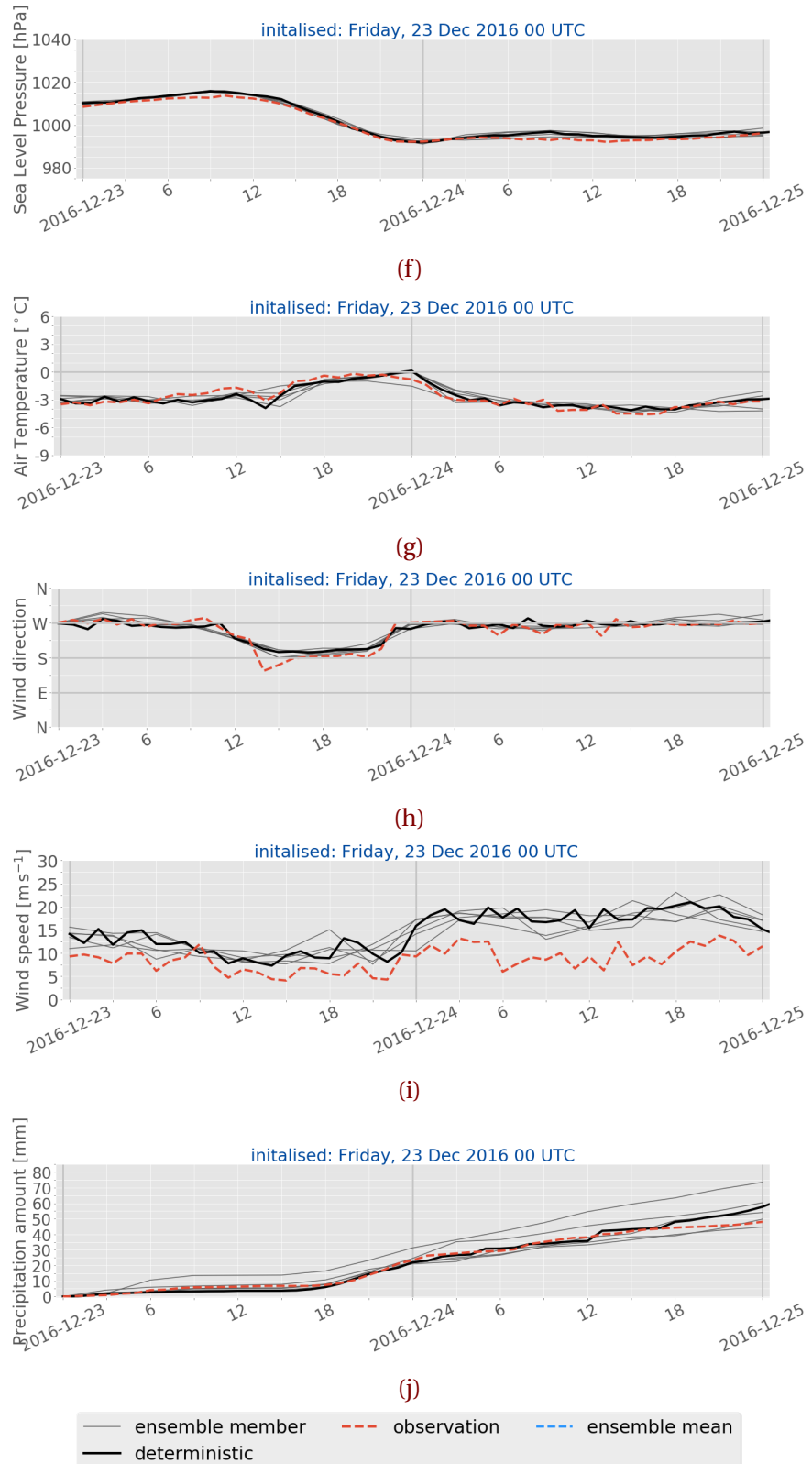


Figure 4.1.1: (Continued from previous page.) Initialisation on 23 December 2016 at 0 UTC.

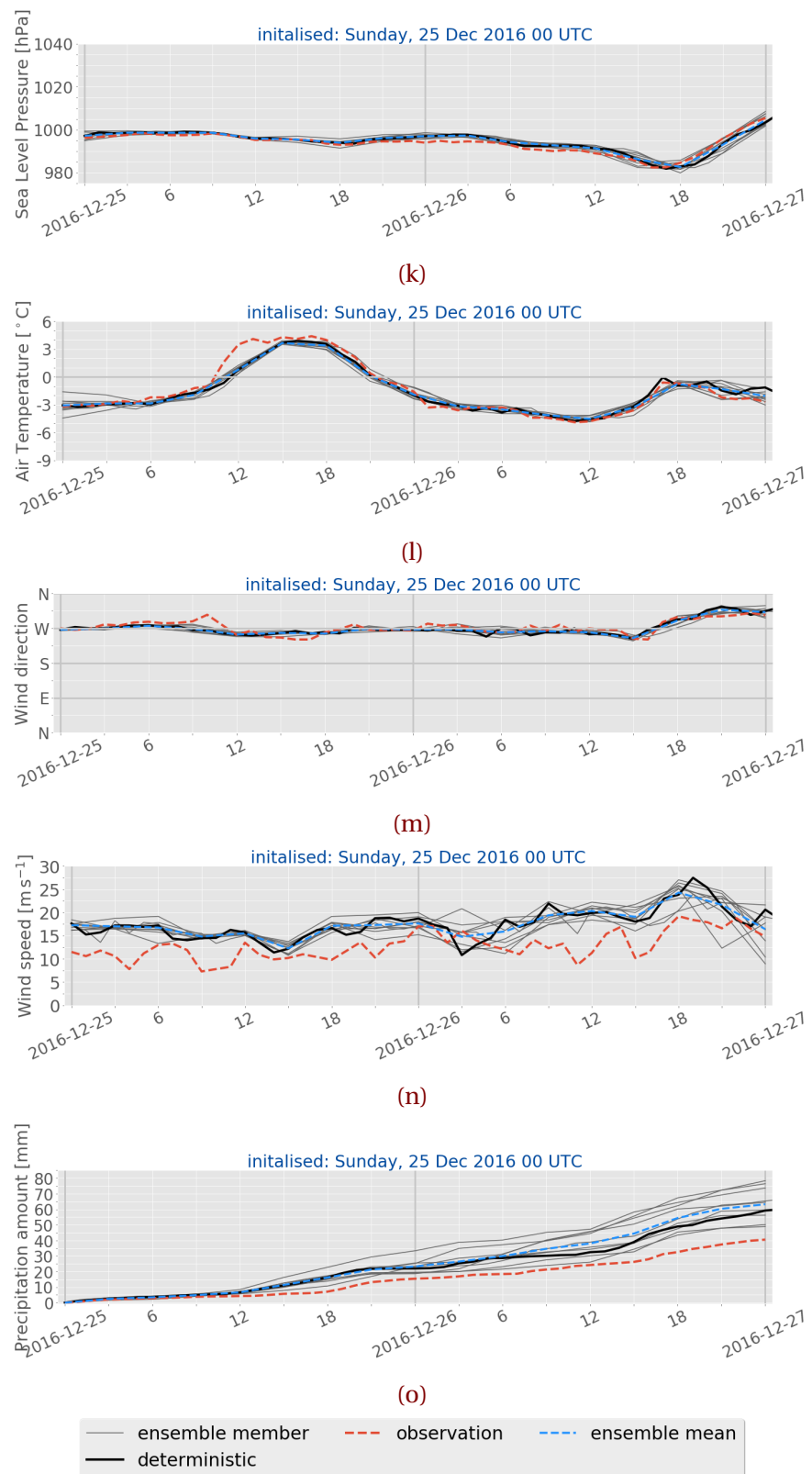


Figure 4.1.1: (Continued from previous page.) Initialisation on 25 December 2016 at 0 UTC.

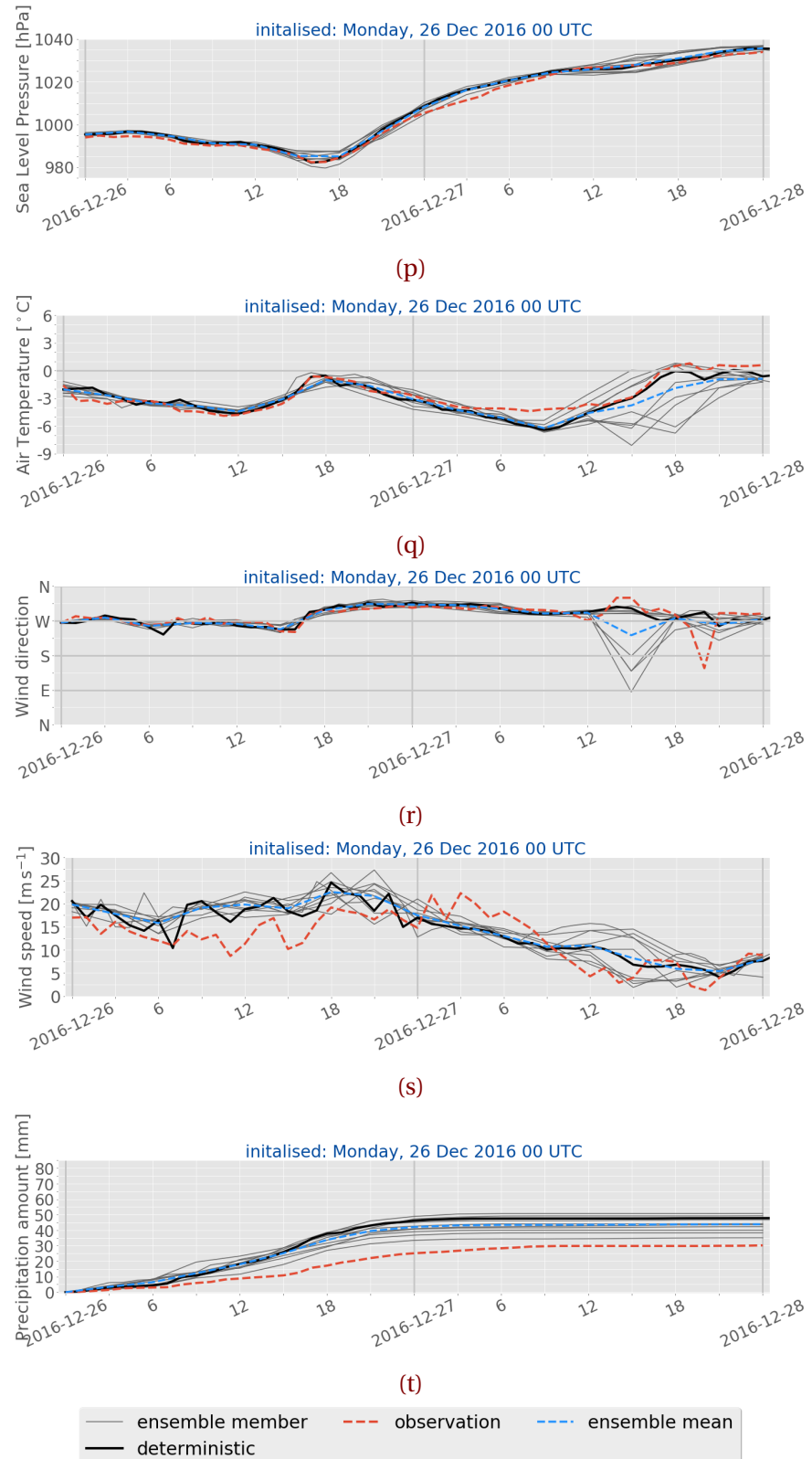
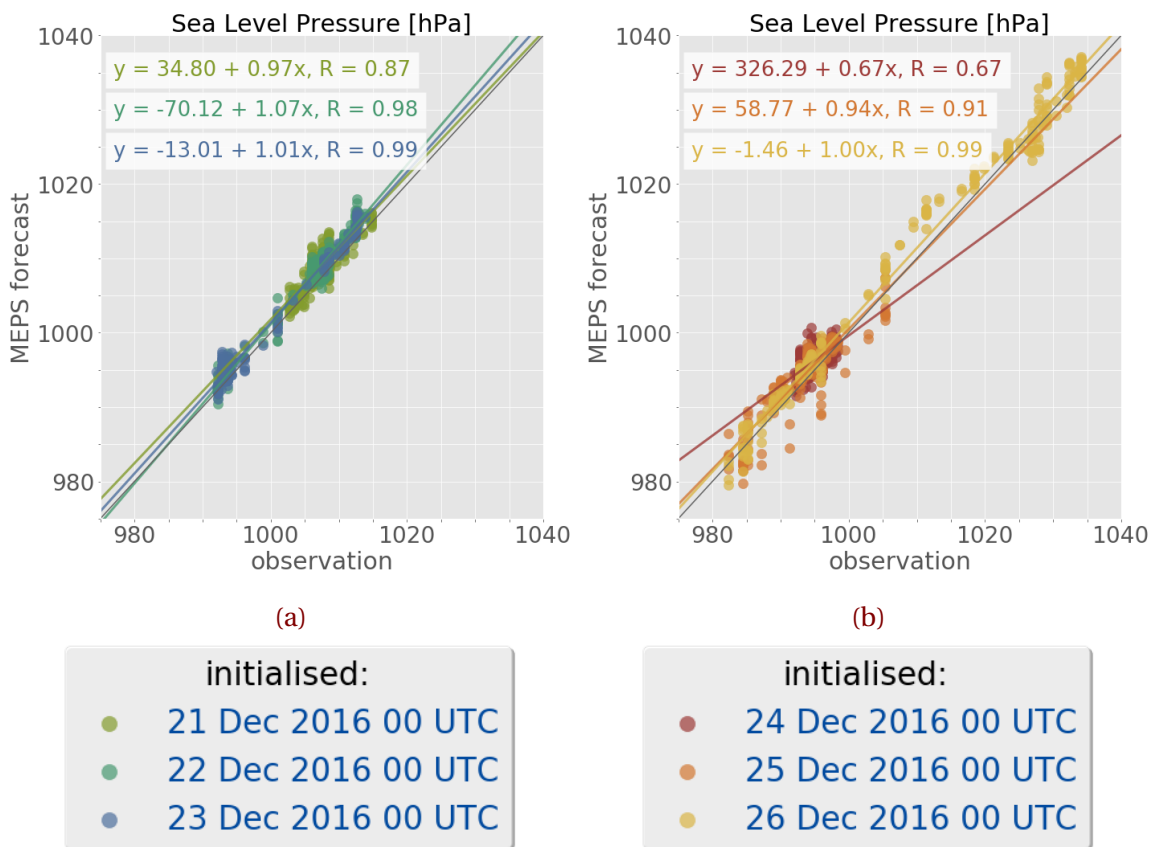


Figure 4.1.1: (Continued from previous page.) Initialisation on 26 December 2016 at 0 UTC.

include R-coefficient Figure 4.1.2 presents the correlation between the observations and the 48 h MEPS ensemble forecast. The relation for Haukeliseter observations and the MEPS forecast members is indicated with the regression calculated for each day. Sea level pressure has the best correlation of all variables. The scatter plots in Figure 4.1.2 show a good correlation for pressure and temperature. Wind direction (Figure 4.1.2f) displays good agreement for 24 to 26 December 2016, but the MEPS forecast imply a disagreement with southerly observed winds in Figure 4.1.2e, between 21 and 23 December 2016. Wind speed is overestimated throughout the event and will be further assessed in Section 4.2.5 (Figure 4.1.2g, h). Surface precipitation amount disagree more between 24 and 26 December 2016 than on 21 to 23 December 2016 (Figure 4.1.2i, j). Figure 4.1.2i suggests a better correlation below 20 mm, for 21 to 23 December 2016 than above. A detailed discussion about the precipitation overestimation at the surface is given in Section 4.2.3.

On 23 and 26 December 2016, pressure decreases and increases, as well as temperature increases, and wind changes are present. Since these changes show in the surface observations in Figures 4.1.1f to 4.1.1j and, Figures 4.1.1p to 4.1.1t, it is assumed that frontal boundaries passed through Haukelieseter. The 25 December 2016 shows an increase of temperature between 15 UTC and 17 UTC leading to the assumption of a warm air evolution in Figure 4.1.1l. The overall weather situation, described in Section 3.6, showed that a warm front as well as cold front influenced Norway, on 25 December 2016. Since pressure and wind do not indicate a change related to frontal development, it is assumed that only the warm air section between the warm and cold front is shown in the surface measurements at Haukeliseter (Figure 4.1.1l).

As described in Section 3.6 the ECMWF dynamic tropopause analysis (Figure 3.6.2a) shows more ridging at the DT level on 23 December 2016, than on the previous days. Warm air is advected closer over to Southern Norway (Figure 3.6.2a). The low-pressure system approaches in the course of the day south-east of Iceland and hence stronger west to south west wind are associated with the cyclone (Figure 3.6.2c). The MEPS forecast, initialised on 23 December 2016 at 0 UTC in Figure 4.1.1f follows the observations and shows the decrease in pressure after 12 UTC due to the shift of the occluded front with a constant pressure after the transition. Since warmer air is more advected to the north and the DT in Figure 3.6.2a shows a warm low-pressure core, an increase in temperature



**Figure 4.1.2:** Scatter plots for surface observations and ensemble forecasts initialised for 21 to 23 December 2016 (left column, **a, c, e, g, i**) and for 24 to 26 December 2016 (right column, **b, d, f, h, j**). The 48 h scatter values indicate each day, showing the 1 h and 3 h forecasts respectively for 48 h. *Continued on next page.*

is observed and predicted at the measurement site (Figure 4.1.1g). **Include L, H in the surface pressure images**

As the cyclone is advected to the north-east, closer into the Norwegian Sea, a wind change is seen in the ECMWF analysis (Figure 3.6.2c). First west wind and later south-west wind is associated with the low-pressure system. The MEPS forecast and observations in Figure 4.1.1h and i indicate a wind change from west to south with a slight decrease in wind speed.

On 23 December 2016, the evolution of the occlusion is also observed by an increase in precipitation. Before 18 UTC the surface accumulation shows light precipitation (Figure 4.1.1j). During the passage of the occlusion, the observed surface accumulation

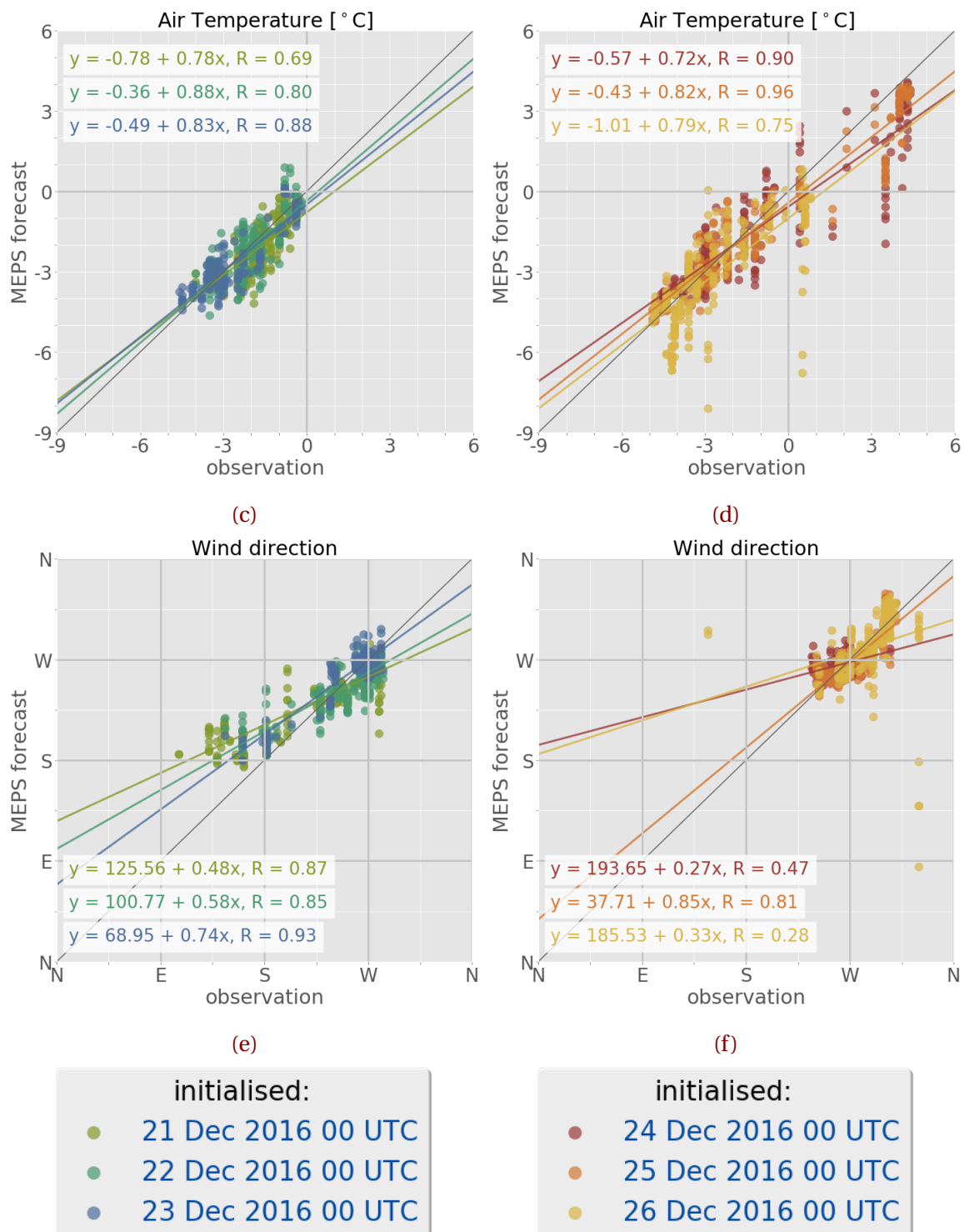


Figure 4.1.2: (Continued from previous page.) Upper panel 2 m air temperature, second panel 10 m wind direction.

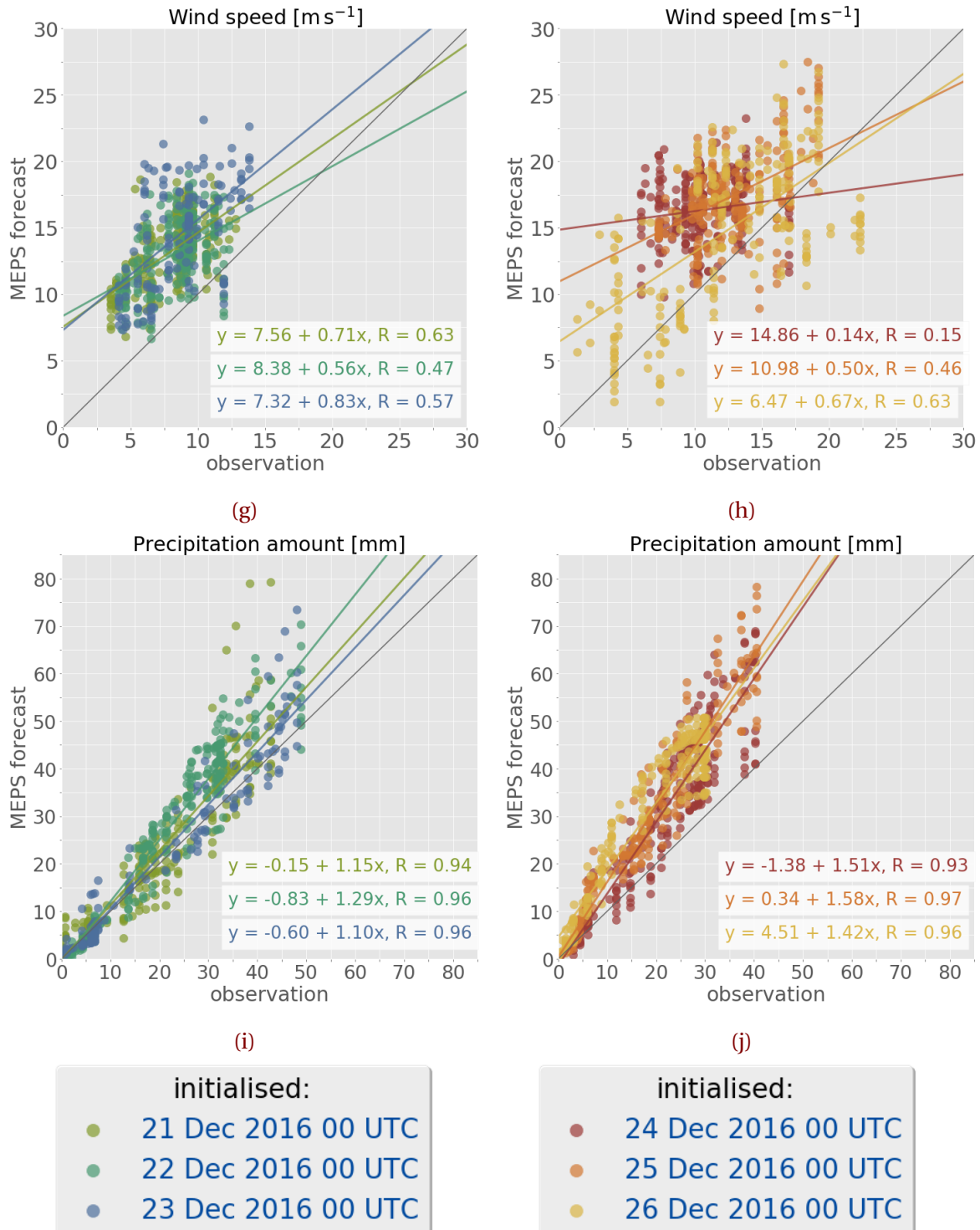


Figure 4.1.2: (Continued from previous page.) Upper panel 10 m wind speed, lower panel surface precipitation amount comparing double fence observations to 48 h MEPS forecasts.

increases which is associated to continuous, heavy precipitation shown in Figure 4.1.1j.

Similar patterns as on 23 December 2016 were seen for the evolution of the occluded front on 26 December 2016 in the ECMWF analysis Figure 3.6.2n and 3.6.2p. In this case the low-pressure system was located north of Møro and Romsdal in the Norwegian Sea. In the morning the cyclone is located east of Iceland and in the course of the day it moves closer to the coast of Norway (Figure 3.6.2o and 3.6.2q). Before landfall at 16 UTC, a pressure decrease occurs at Haukeliseter (Figure 4.1.1p). During the development of the occluded front, the sea level pressure reaches its lowest point of 985 hPa (Figure 4.1.1p) and increases afterwards during the dissipation of the 2016 Christmas storm.

Since the cyclone was surrounded by colder air (south of the low-pressure system in Figure 3.6.2n), first a drop and then an increase of temperature were observed and forecasted by MEPS (Figure 4.1.1q). An indication of the occlusion evolution is also visible in the 10 m wind observations and MEPS predictions in Figure 4.1.1r and s. On 26 December 2016 at 0 UTC, the low pressure system is east of Iceland (not shown), moving closer into the Norwegian Sea by 12 UTC (Figure 3.6.2n and 3.6.2p). Surface west winds are associated to the cyclone in the Norwegian Sea, and impinging on the West coast of Norway Figure 3.6.2p. The wind measurement and MEPS forecast in Figure 4.1.1r and 4.1.1s, show a gentle west breeze of up to  $17 \text{ ms}^{-1}$  at Haukeliseter before 12 UTC. The centre of the occluded front is located over Norway at 18 UTC, and the pronounced surface pressure gradient, in Figure 3.6.2q, indicate an increase in surface wind with a north-west wind direction. During this transition of the occlusion, the wind direction changes to north-west with higher observed wind speeds up to  $20 \text{ ms}^{-1}$  (Figure 4.1.1r and 4.1.1s).

Precipitation is continuing throughout the day, with light to moderate precipitation before the occlusion passage seen in Figure 4.1.1t. Heavy precipitation related to the occlusion, around 16 UTC, is followed by moderate to light deposition on 26 December 2016.

While on 23 and 26 December 2016 precipitation was associated with a transition respectively landfall of an occlusion, the 25 December 2016 was marked by the transition of a warm sector. The ECMWF analysis shows a ridging of warm air at the dynamic tropopause (Figure 3.6.2i). The cyclone core is south east of Iceland in Figure 3.6.2i with two associated frontal boundaries. While the warm front is approaching the west coast,



**Figure 4.1.3:** MASC images of falling water drops observed on 25 December 2016 at 17 UTC from three different angles. Not all parts of the liquid sphere are equally illuminated.

the cold front is north-west of Great Britain. In Figure 3.6.2k, the tail of the cold front moved into lower latitudes, following the slowdown of front, leading to a stationary frontal boundary. Furthermore, the mid-latitude jet is aligned with the surface frontal boundaries (??), while the Haukeliseter site is located below the the midlatitudal jet (??).

Neither pressure nor wind observations and forecasts in Figure 4.1.1k, m, and n, indicate the evolution of any frontal boundary. The only indication of a transition could be seen in the increase and then decrease of temperature at 11 UTC until 21 UTC (Figure 4.1.1l). In Figure 4.1.1m, a small wind change from west to north-west is observed by the wind mast at 10 UTC, which is not forecasted by MEPS, it rather estimated strong westerly winds.

Particle images taken by the MASC are available on 25 December 2016, during the transition of the warm sector in Figure 4.1.3. Without theses images taken around 17 UTC it would only be possible to verify that liquid precipitation occurred with the optical precipitation detectors at the Haukeliseter site. Together with the increase in surface temperature (Figure 4.1.1l) it can be concluded that the warm sector of the Christmas 2016 event passed by the measurement site. **KICKI: Should I include the DIANA analysis maps? But the meteorologist also use ECMWF to make them!**

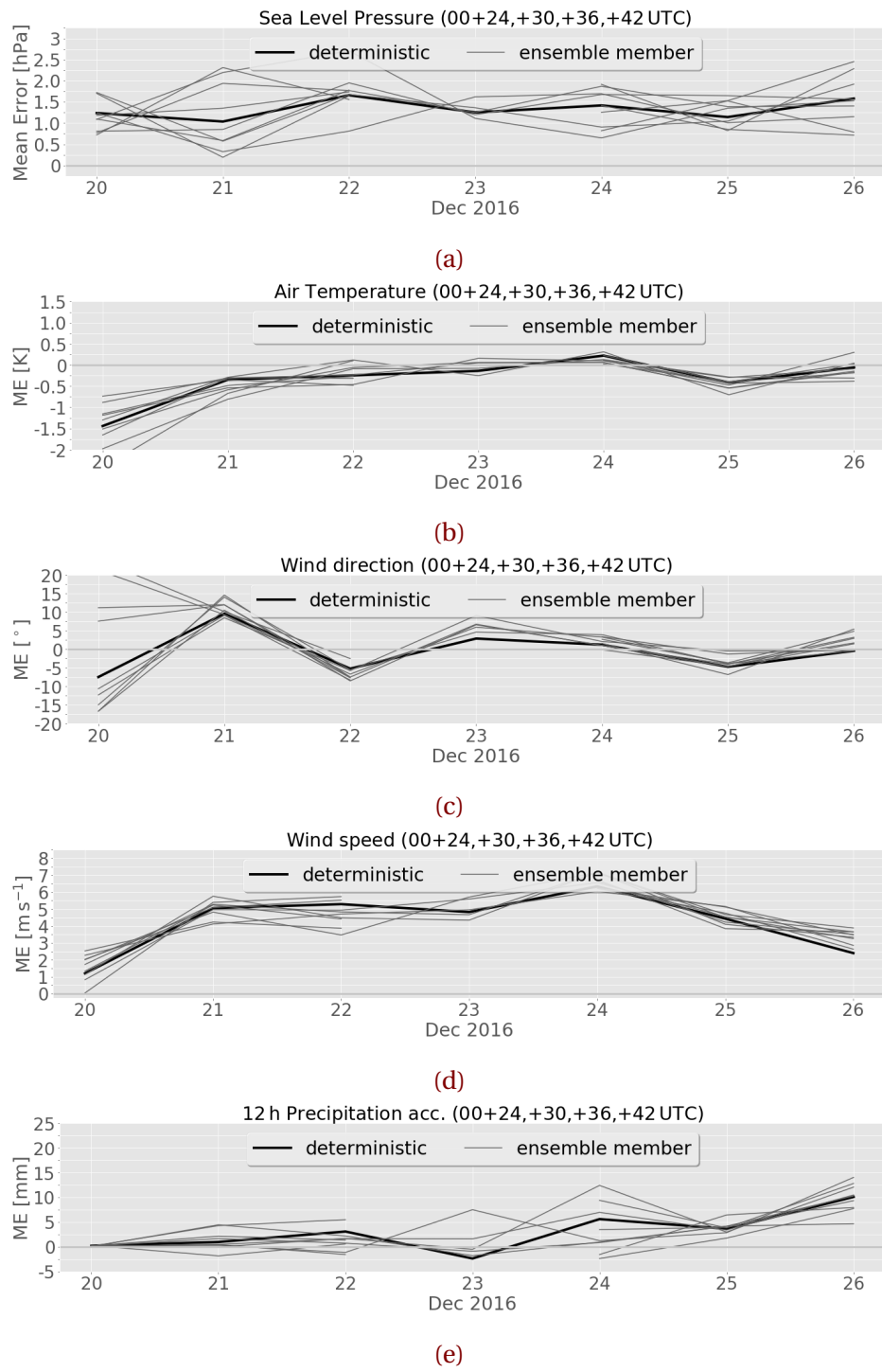
The comparison between the ECMWF analysis (Section 3.6) and the observations at the measurement site (Figure 4.1.1), led conclude that the ensemble member forecast system MEPS covers the prediction of large scale phenomena like occlusions and fronts, as well as liquid precipitation at the surface.

The scatter plots for observations and MEPS forecast show good correlation for most

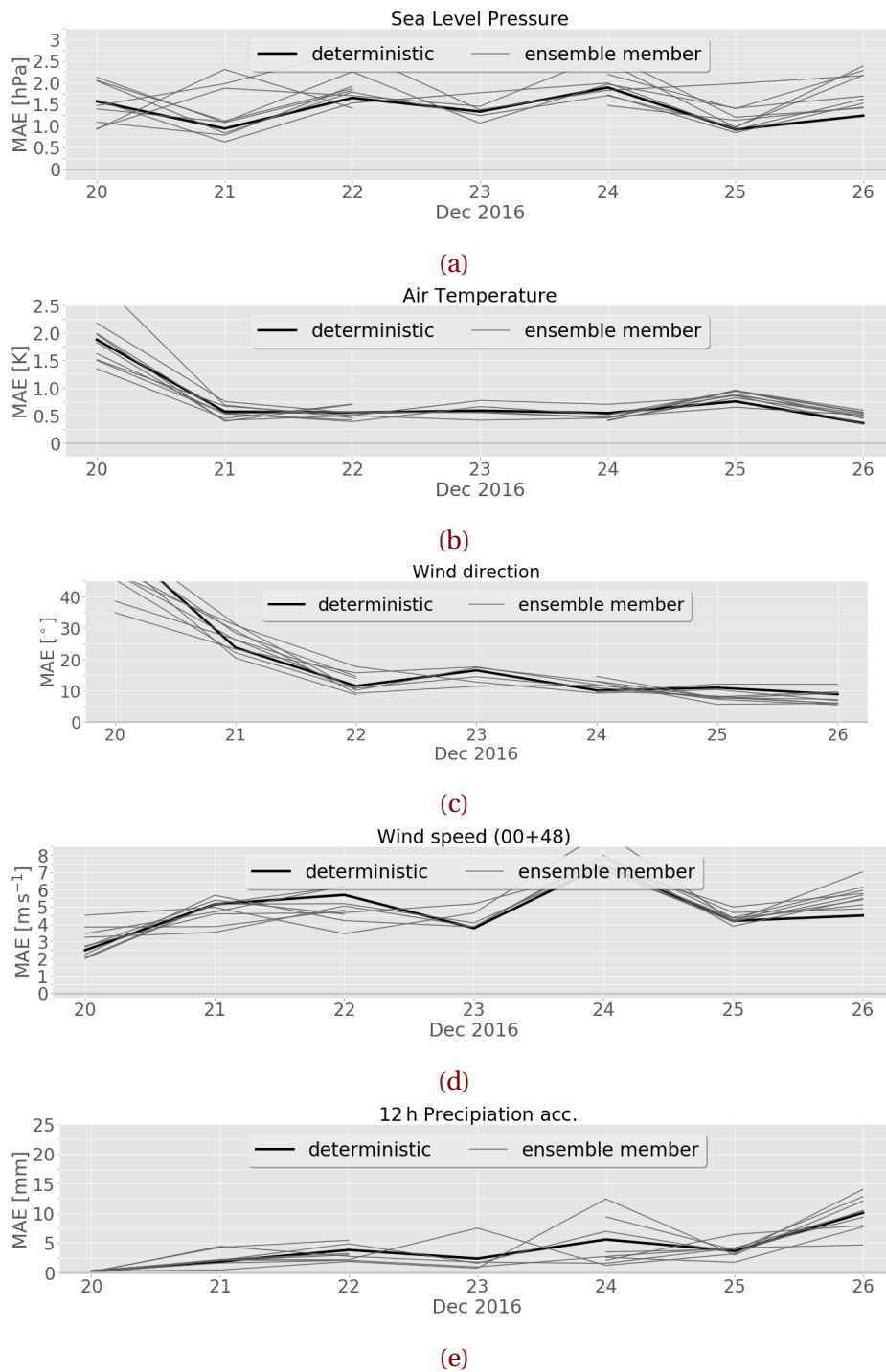
variables (Figures 4.1.2a to 4.1.2d, and f). The best agreement for pressure is reached on 26 December 2016 (Figure 4.1.1p), when the Christmas storm hit land and dissipated after the evolution of the occlusion at 16 UTC. Dahlgren [2013] showed an improvement of sea level pressure forecast for AROME, by including large scale boundary conditions for ECMWF into the regional model. The observation-model comparison by Dahlgren [2013] showed a decrease of pressure bias with lead time after 24 h with the use of pressure mixing. Since surface pressure is in good agreement with the observations, it is assumed that the warm front did not pass through Haukeliseter on 25 December 2016 and only the warm sector associated with the 2016 Christmas storm is observed. This shows a quite detailed forecast ability of MEPS, as from the ECMWF analysis, in Figure 3.6.2i, it is not quite clear if the warm front could have passed through. To be sure that the warm front did not pass through Haukeliseter, or whether it is a predictive error of MEPS, surface pressure, temperature and wind should be compared to the nearest grid point of the global forecast model ECMWF to verify this result.

Figure 4.1.2d displays a moderate correlation between observation and the 48 h MEPS ensemble member forecast system. In general, MEPS underestimates the observed 2 m air temperature, but MEPS estimated the surface temperature changes at the correct occurrence for 23, 25, and 26 December 2016.

Figure 4.1.4b shows warm and cold biases for 23 and 26 December 2016, respectively. On 25 December 2016, within the warm sector a cold bias was observed, underestimating the temperature when compared to the observation. The forecasts for 23, 25, and 26 December 2016 show calculated mean absolute error values (Equation (2.6.11)) of up to 0.61 K, 0.77 K and 1.44 K in Figure 4.1.5b. The previous operational deterministic forecast model AROME-MetCoOp showed a cold bias of 2 m temperature for the Norwegian mean, during winter 2013 with the introduction of AROME-Norway and later AROME-MetCoOp [Müller et al., 2017]. The mean error for the Norwegian model domain of AROME-MetCoOP estimated by Müller et al. [2017] is smaller than 1.8 K for the surface 2 m temperature in December 2014. The new ensemble forecast system MEPS shows a reduction of mean errors for the Christmas 2016 extreme event, when compared to the Norwegian mean of AROME-MetCoOp.



**Figure 4.1.4:** Mean error (a, b, c, d, e) of surface variables for all ten ensemble members at Haukeliseter, initialisations at 0 UTC, valid for 48 h. From top to bottom, sea level pressure (a), 2 m air temperature (b), 10 m wind direction (c), 10 m wind speed (d), precipitation accumulation for 12 h surface accumulation (e).



**Figure 4.1.5:** Mean absolute error (a, b, c, d, e) of surface variables for all ten ensemble members at Haukeliseter, initialisations at 0 UTC, valid for 48 h. From top to bottom, sea level pressure (a), 2 m air temperature (b), 10 m wind direction (c), 10 m wind speed (d), precipitation accumulation for 12 h surface accumulation (e).

During the Christmas storm 2016, high wind speeds were observed at the Haukeliseter site (Figure 4.1.1i, n and s). According to Müller et al. [2017] high wind speeds are significantly better simulated for AROME-MetCoOp compared to ECMWF's forecast for the model domain. Wind speed MEPS predictions in Figure 4.1.1i, n, and s displays still an overestimation of wind speeds throughout the event. Furthermore, the correlation of observations and wind speed in Figure 4.1.2g and h show an overestimation for stronger wind speeds on 24 to 26 December 2016 than for 21 to 23 December 2016. The mean absolute error for wind speed during the Christmas storm is ranging from  $3\text{ ms}^{-1}$  to  $7\text{ ms}^{-1}$  for 48 h lead time. During the three days of frontal transitions, the highest mean absolute error of  $6.5\text{ ms}^{-1}$  occurs for initialisations on 23 December 2016. The inaccuracy for wind speeds is an already known difficulty in the deterministic version of MEPS [Müller et al., 2017]. Müller et al. [2017] presented, that AROME-MetCoOp wind speed prediction generally agreed better with observations for wind speeds between  $3\text{ ms}^{-1}$  to  $13\text{ ms}^{-1}$  than ECMWF forecasts did, showing the advantage of a high-resolution weather model. Furthermore, with increasing wind speed the forecast accuracy for the Norwegian mean decreased with a mean absolute error below  $2\text{ ms}^{-1}$  for 6 h to 24 h lead times, in December 2014 in AROME-MetCoOp. Müller et al. [2017] study case showed a slight underestimation of ECMWF 10 m wind compared to the Norwegian AROME-MetCoOp forecast for February 2015. On 23 December 2016, the mean absolute error is more than three times as high as the monthly averaged value for the Norwegian forecast domain ( $2\text{ ms}^{-1}$  for 6 h to 24 h forecast time) from Müller et al. [2017]. The larger mean absolute error during the event is firstly related to the comparison of a long term study of Müller et al. [2017], secondly their mean absolute error monthly average for 6 h to 24 h lead times, and third to the location of Haukeliester.

Haukeliseter is a measurement site exposed to high wind speeds [Wolff et al., 2013, 2015]. The ensemble prediction system MEPS seems to still have issues forecasting the wind speed correctly in mountainous terrain. A detailed insight to the orographical wind influence will be assessed in Section 4.2.5.

Pressure, temperature, and wind changes for the occlusion transition on 26 December 2016 were already forecasted for initialisations on 25 December 2016 (Figure 4.1.1k, l, m, n), only wind speed and precipitation seem not to agree with the observations at Haukeliseter. The same is true for 25 December 2016, when the warm

sector passes through Haukeliseter.

Figure 4.1.1e, j, o, and t illustrate the surface precipitation amount observed and predicted by MEPS for Haukeliseter. MEPS overestimation is shown for precipitation when the cyclone intensifies and gets closer to Norway on 24, 25 and 26 December 2016. The surface observations and MEPS predictions in Figure 4.1.2i and j show an overestimate for 24, 25 and 26 December 2016, whereas on 21, 22, and 23 December 2016 the surface accumulation is balanced for predictions up to 30 mm. Any reasons for the overestimation of precipitation accumulation on the ground will be further analysed and discussed in Section 4.2.3. What could be still a weakness that the model overestimates the wind speed? In Müller et al. [2017]: change from ECOCLIMAP1 because the surface roughness was too low and followed high wind speeds? Is this still the case for MEPS? High wind speeds followed also from wrongly addressed 'permanent snow'. Do not use 'orographic drag' in AROME-MetCoOp, could that lead to the too high estimated wind? When 'canopy drag' was changed saw increase in SBL drag which followed a decrease in wind speed. But AROME-MetCoOp is able to forecast high wind speeds, while ECMWF is not.

Overall, for initialisations on 21 to 23 December 2016 (Figure 4.1.2a, c, e, g) the forecast is best for all variables. The large-scale weather pattern seems to be more predictable as long as the weather situation is not extreme. Figure 4.1.2b, d, f, h suggest as if MEPS has difficulties predicting the intensification and associated pressure decrease of the Christmas 2016 storm at Haukeliseter. The prediction of pressure fits well on all days (Figure 4.1.2a, b) compared to temperature, wind direction, wind speed, and precipitation (Figures 4.1.2c to 4.1.2j). The greatest difficulty has MEPS with the prediction of wind speed during the entire extreme event. The rainfall, however, fit well for 23 December 2016 (Figure 4.1.1j and 4.1.2i), but MEPS has problems predicting the accumulation of surface precipitation amount correctly for the extreme days of the 2016 Christmas storm, 24 to 26 December 2016 (Figure 4.1.1o, t and Figure 4.1.2j).

Figures 4.1.2a to 4.1.2d have shown good agreement of ensemble members. It is not expected that ensemble members agree they should just give a variability around the observations, that is why ensemble member prediction exists (Section 2.5). Based on the uncertainty in observations the solution space that is possible has to be understood. During extreme events the model is not adjusted to present the extreme event particularly

well.

## 4.2 SNOWFALL COMPARISON

Get some text to flow

### 4.2.1 SENSITIVITY OF THE OPTIMAL ESTIMATION RETRIEVAL

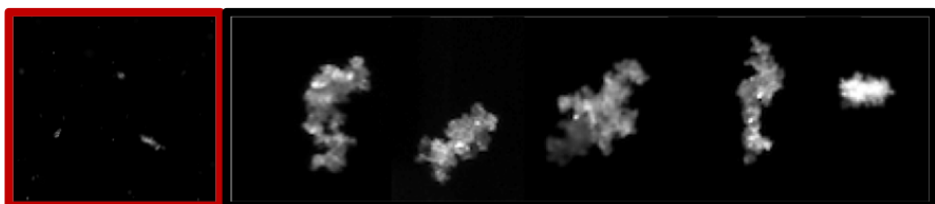


**Figure 4.2.1:** MASC observations during the Christmas storm 2016. Left (red frame), small ground up blowing snow particles. Five images on the right, rimed particles.

The optimal estimation retrieval scheme was applied to the six-day Christmas 2016 storm event. MASC images of snowfall during the event were used to guide the selection of the appropriate particle model and PSD input for the retrieval scheme. In this section, the sensitivity of retrieval results to these inputs is explored. Such an exercise should also allow an identification of those properties that yield the best match with Met-Norway snow gauge measurements at Haukeliseter.

The majority of the MASC images from Haukeliseter contained snow particles that looked like the left image Figure 4.2.1 (red frame). Such images suggest small ground-up blowing snow particles that are consistent with the high winds observed during the event. However, a careful examination of the MASC images also finds the presence of rimed aggregates such as those in the right five images (Figure 4.2.1). Pristine crystals such as plates and columns were not observed during the christmas 2016 event. As such, the use of two different aggregate particle models developed for the CloudSat mission were explored.

Figure 4.2.2 presents hourly measured snowfall accumulations on 22 December 2016 plotted against retrieved values for the two different aggregate assumptions. The 'B8' aggregate is a low reflectivity per unit mass aggregate that worked well for the cold, dry conditions observed at Barrow as described in [Cooper et al. \[2017\]](#). The 'B6' aggregate is a high

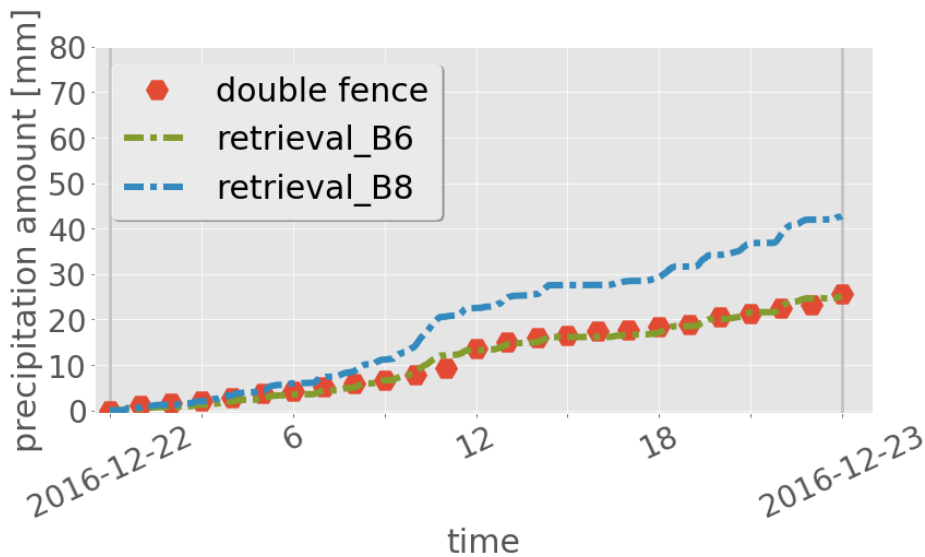


**Figure 4.2.2:** Hourly double fence snowfall accumulations [mm] plotted against retrieved values for the 22 December 2016 for different retrieval assumptions permutations. Double fence snowfall accumulation, red hexagons, retrieved precipitation amount for the here used study (B6), green, dash-dotted, and for small aggregates (B8), blue dashed.

reflectivity per unit mass particle. As such, the 'B6' aggregate would seem more physically consistent with the observed rimed particles and high water environment found in the coastal mountains at Haukeliseter. The presence of a water or rimed coating on the aggregates aloft would greatly enhance their effective reflectivity. Indeed, Figure 4.2.2 suggests that the reflective 'B6' aggregate agreed much better than the less reflective 'B8' aggregate with the snow gauge.

Table 4.2.1 presents the percentage differences between snow gauge and retrieved estimates found when using these particle model assumptions for 22 December 2016. Use of the 'B6' aggregate agreed within 5 % of the double fence observations (Table 4.2.1) for both 12 h and 24 h surface accumulations. Admittedly, use of the 'B6' aggregate produced slightly too little snowfall relative to the gauges for the remaining days of the event as discussed in Section 4.2.2. The use of the 'B8' aggregate, however, overestimated snowfall by at least 65 % for both the 12 h and 24 h surface accumulations (Table 4.2.1). Since this aggregate had low reflectivity per unit mass, it required significantly more SWC in the for-

**Table 4.2.1:** Observations (obs.) and retrieved (ret.) snowfall amounts for 22 December 2016 for different particle model assumptions. B6 indicating the here uses particle model (Appendix A.1) and B8 indicating the retrieved snowfall amounts for small particles.

Particle model	12 h accumulation				24 h accumulation			
	Snowfall		Difference		Snowfall		Difference	
	obs.	ret.			obs.	ret.		
	[mm]		[%]		[mm]		[%]	
B6	13.6	13.2	-3.0		23.1	25.1	-2.1	
B8	13.6	22.5	+65.5		23.1	42.7	+66.9	

ward model calculations to match MRR reflectivities. The retrieval therefore overestimates snowfall rate for these meteorological conditions.

The discussion here has focused on MASC estimates of habit instead of PSD or fall speed. The reason is that the MASC and PIP saw primarily blowing snow particles at the surface that likely were much smaller than the particles that the MRR remotely sensed aloft. The use of the PSD measured by the MASC or PIP in the retrieval therefore produced snowfall totals much greater than those measured by the double fence snow gauges. Essentially, it takes a much greater mass of small particles than large particles to match a given reflectivity. These results contrast with those found for low wind speed events at Haukeliseter where the use of MASC habit, PSD, and fall speed observations resulted in retrieved snowfall accumulations very close to Met-Norway double fence gauge observations. Regardless, for this high wind event, the [Wood \[2011\]](#) a priori temperature PSD relationship and a climatological average fallspeed of  $0.85 \text{ m s}^{-1}$  [private communication, [Schirle, 2018](#)] were employed.

#### 4.2.2 COMPARISON OF SURFACE OBSERVATIONS

To be able to compare the vertical predicted snow water content with the retrieved snow water content a verification of the surface accumulation is made. If the retrieved surface accumulation is confident in comparison to the double fence measurement, then the vertical measurements can be trusted.

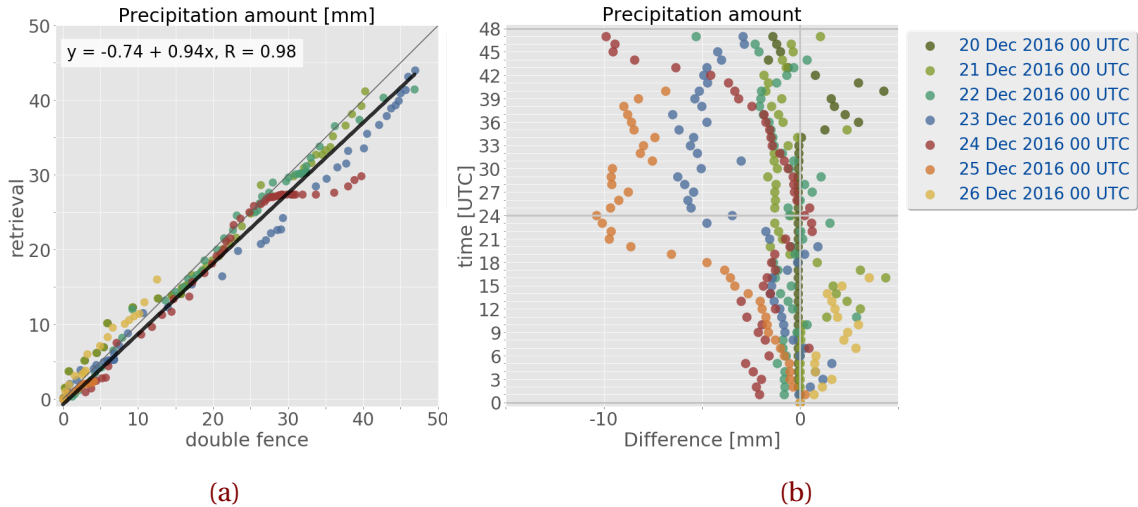
The correlation in Figure 4.2.3a demonstrates a good agreement between the 48 h accumulation measured by the double fence and the retrieved surface accumulation. The black line in Figure 4.2.3a presents a linear correlation with a regression coefficient of  $R = 0.97$ . In general, the retrieved surface snowfall accumulation is underestimated when compared to the double fence measurements, but not to a large degree.

Figure 4.2.3b shows the difference between retrieved accumulation and observed accumulation by the double fence. For the time period 20 to 24 December 2016, Figure 4.2.3b indicates an underestimation of retrieved snow accumulation of less than  $-5\text{ mm}$  for the first 24 h. Snow accumulation calculated on 23 December 2016 at 0 UTC show after 24 h an underestimation by the retrieval of up to  $-6.5\text{ mm}$ . On 24 December 2016, larger underestimation after 43 h is related to the observation of liquid precipitation on 25 December 2016 between 12 UTC to 21 UTC. On 25 December 2016 no fair comparison to the double fence measurement can be performed after 12 UTC because of the neglection of liquid precipitation when temperatures exceed  $2^\circ\text{C}$ .

For a 12 h accumulation follows for the Christmas storm (21 to 26 December 2016) an average difference of 85.5 % (Table 4.2.2). For longer, 24 h accumulation decreases the average difference to be  $-4.7\%$  (excluding values on 25 December 2016 after 12 UTC and on 26 December 2016 after 17 UTC because of attenuation at the MRR). The daily surface snowfall accumulation difference between retrieval and observation in Table 4.2.2 show almost always a well agreement to the double fence. The only well pronounced mismatch is seen on 21 December 2016, where it measures much more than the double fence gauge (+435.8 %).

Similar to this study, Cooper et al. [2017] used a CloudSat snow particle model, PSD and fall speed from MASC observations for five snow events at Barrow, Alaska. The comparison to the weather station revealed an difference between National Weather Service observations and retrieved accumulations of  $-18\%$  for five snow events.

Table 4.2.2 shows the difference for each individual day and the average difference for six and four days, depending on the accumulation of 12 h or 24 h. The choice of the correct PSD model, slope parameters and fall speed in the optimal estimation snowfall retrieval, shows a good agreement with the observations at Haukeliseter for the 2016 Christmas storm in contrast to the 200 % difference when only using the CloudSat snowfall algorithm (Section 2.4). It indicates also a reduction of the non-uniqueness of snow accumulation is



**Figure 4.2.3:** **a:** Surface precipitation amount comparison between the double fence observations and the retrieved surface accumulation of precipitation for 48 h. In black the linear correlation between the double fence observations and retrieved surface snow. **b:** Difference between the retrieved and the observed accumulation by the double fence. The colours represent the different starting days at 0 UTC for the 48 h accumulation.

reduced, when using a combination of ground-based observations instead of only Ze-S relationships.

It turns out that there is no relation between high and low precipitation events since the differences vary daily. [Cooper et al. \[2017\]](#) showed also different combinations of PSD assumptions and snow fall speed. For Barrow, best agreements between observations and retrieved snowfall were found by using the CloudSat particle model, slope parameters and snowfall speeds from the MASC. In the here presented study, the best assumption for surface snowfall accumulation was found by using a particle model for rimed aggregates (Section 2.4 and 4.2.1) such as in Figure 4.2.1.

On 20 and 21 December 2016, the difference error is large ( $-97.8\%$  and  $435.8\%$ , respectively). This is probably related to an observation of precipitation at the double fence, even though no precipitation was observed. On 20 December 2016, observation at the double fence might be related to some particles stirred up by wind into the orifice of the gauge. Since no manual observations are done at the Haukeliseter site, is it difficult to say if blowing snow occurred or if it was snowing. This introduces additional errors

**Table 4.2.2:** Comparison of observed (obs.) and retrieved (ret.) snowfall amounts for the Christmas storm 2016. Difference refers to the difference of the retrieved and observed snow accumulation after 12 h and 24 h. The average difference is the value over all six/four days. Excluding values after 12 UTC on 25 December 2016 and after 17 UTC on 26 December 2016.

Day in 2016	12 h accumulation				24 h accumulation			
	Snowfall		Difference	Average difference	Snowfall		Difference	Average difference
	obs.	ret.			obs.	ret.		
	[mm]		[%]	[%]	[mm]		[%]	[%]
20 Dec	0.1	0.0	-97.8		0.1	0.0	-97.8	
21 Dec	0.7	3.8	+435.8		17.1	16.6	-2.7	
22 Dec	13.6	13.2	-3.0	-2.1	25.6	25.1	-2.1	-4.7
23 Dec	6.3	5.2	-16.8		23.3	19.8	-14.9	
24 Dec	14.7	13.4	-8.6		24.8	25.0	+0.8	
25 Dec	4.3	-	-		+15.4	-	-	
26 Dec	8.8	10.6	+20.1		25.1	-	-	

on the double fence measurements. From the vertical MRR reflectivity, in Section 4.2.4, Figure 4.2.6, it can be seen, that precipitation was not observed on 21 December 2016 before 9 UTC.

Even though it is assumed that the double fence is the correct measurement it still underlies some uncertainties, such as under-catch during high wind speeds [Wolff, 2018]. A better way to asses the accuracy of the retrieved surface snowfall accumulation could be to compare the results to measurements inside a bush gauge.

Wolff [2018] estimates the under-catchment of double fence gauge compared to bush gauge measurements to 10 %, for outside winds of  $9 \text{ m s}^{-1}$  (Section 2.3.1). If the double fence gauge underestimate snowfall under high wind condition, would follow that the optimal estimation retrieval results are more than 20 % too low to the true state.

Anyway, the low average difference value for 24 h accumulation, in Table 4.2.2 during the Christmas 2016 event (-4.7 %) follow a much lower average difference between retrieved and observed surface accumulation than at Barrow (36 %) and therefore a

very good agreement between observed and retrieved snow accumulation during 21 to 24 December 2016. In Section 4.2.4, the vertical SWC will be compared to the forecasted MEPS values for the 2016 Christmas storm. Despite the undercatchment of wind related snow precipitation, the double fence measurement give confidence for the retrieved profiles of snow water content. While snow water content is compared to the MEPS forecast, it should be kept in mind that retrieved snow accumulation is underestimated and therefore the vertical SWC may be too low.

#### 4.2.3 MEPS FORECAST AND SURFACE OBSERVATION COMPARISON

One approach of this study is to see if observed surface accumulation was correctly predicted by the newly operational regional weather forecast model MEPS (Section 2.5). Figure 4.2.4 shows observations at the double fence, retrieved snow accumulation, and MEPS forecast for 48 h. Hereafter, MEPS surface precipitation prediction forecast is compared to the double fence gauge observations at Haukeliseter. Accumulation measured by the double fence are presented as red hexagons. Minutely retrieved surface snowfall amount in dash-dotted green. Lines in black and grey show the deterministic and perturbed members for lead time of 48 h. The blue dashed line shows the ensemble mean of all ten members. The ensemble mean of precipitation amount is calculated every three hours, due to the three hourly time resolution of most of the perturbed member. When not all perturbed member data was available from [Norwegian Meteorological Institute \[2016\]](#), like on 23 December 2016 (Figure 4.2.4c), no ensemble mean is calculated. At the bottom of Figure 4.2.4 the associated 10 min average wind of the last hour from the 10 m weather mast at Haukeliseter is presented, to see if surface accumulation observations may be influenced by wind.

In general, Figures 4.2.4a to 4.2.4c show a better agreement between double fence observations and forecast for 48 h forecasts initialised on 21 to 23 December 2016 at 0 UTC. The double fence observation lie for 21, 22, and 23 December 2016 within the spread of the ensemble members (Figures 4.2.4a to 4.2.4c), covering the uncertainty within the measurements (Section 2.5). On the other hand, observations between 24 and 26 December 2016 are too low compared to the ensemble spread (Figures 4.2.4d to 4.2.4f). During 24 and 26 December 2016, the low-pressure system intensifies and gets closer to the Norwegian coast, and influence the local weather in Norway (Section 3.6).

Figure 4.2.4d, e, and f indicate a larger estimated surface precipitation amount for all ten ensemble members compared to observed values at the measurement site between 24 to 26 December 2016.

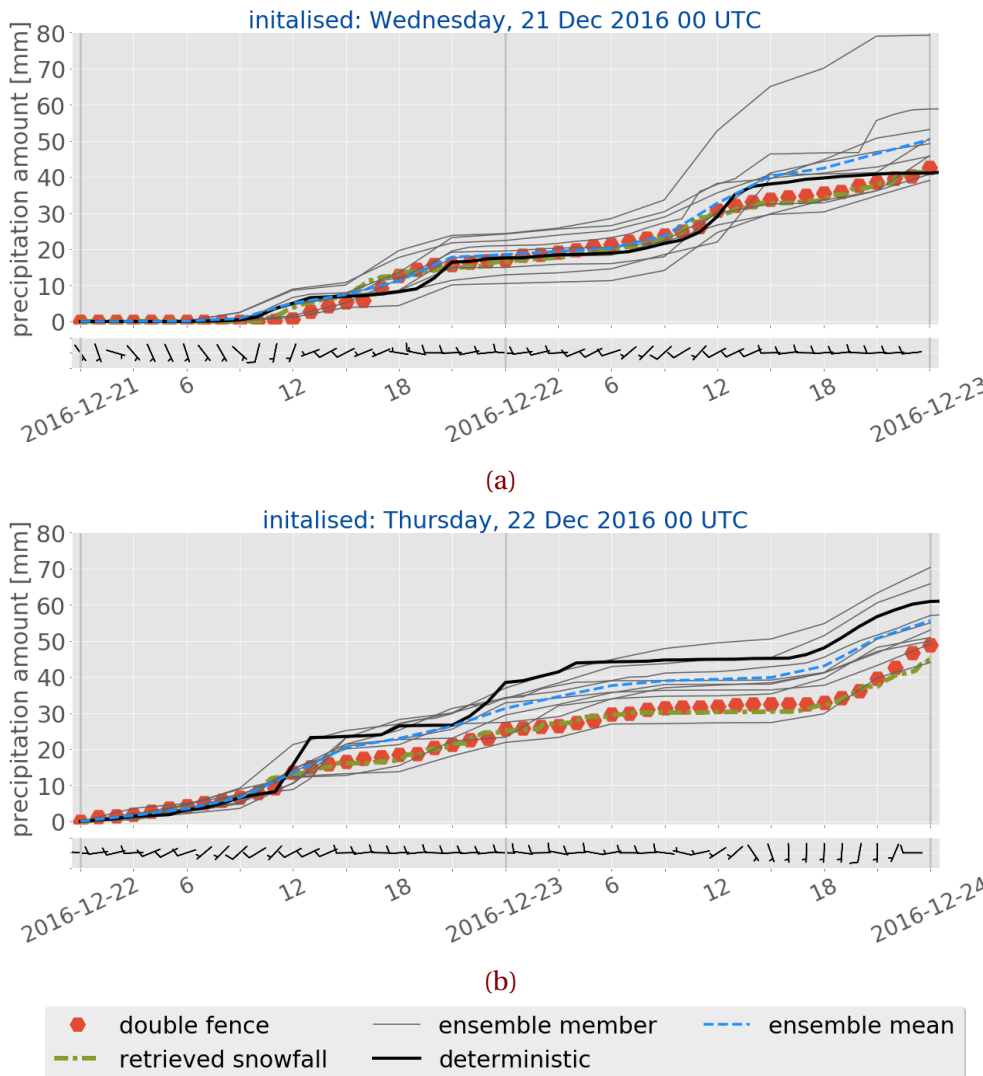


**Figure 4.2.4:** 48 h surface snowfall accumulation for 21 to 26 December 2016 (a to f). Representing the values from the double fence in red, hexagons; optimal estimation retrieval output at the first noise free level in dash-dotted green; MEPS ensemble member deterministic forecast, initialised at 0 UTC in black and its nine perturbed ensemble members in grey. The ensemble mean of all ten members is shown in dashed blue. Underneath is the associated last hour 10 min average wind from the weather mast at 10 m height. *Continued on next page.*

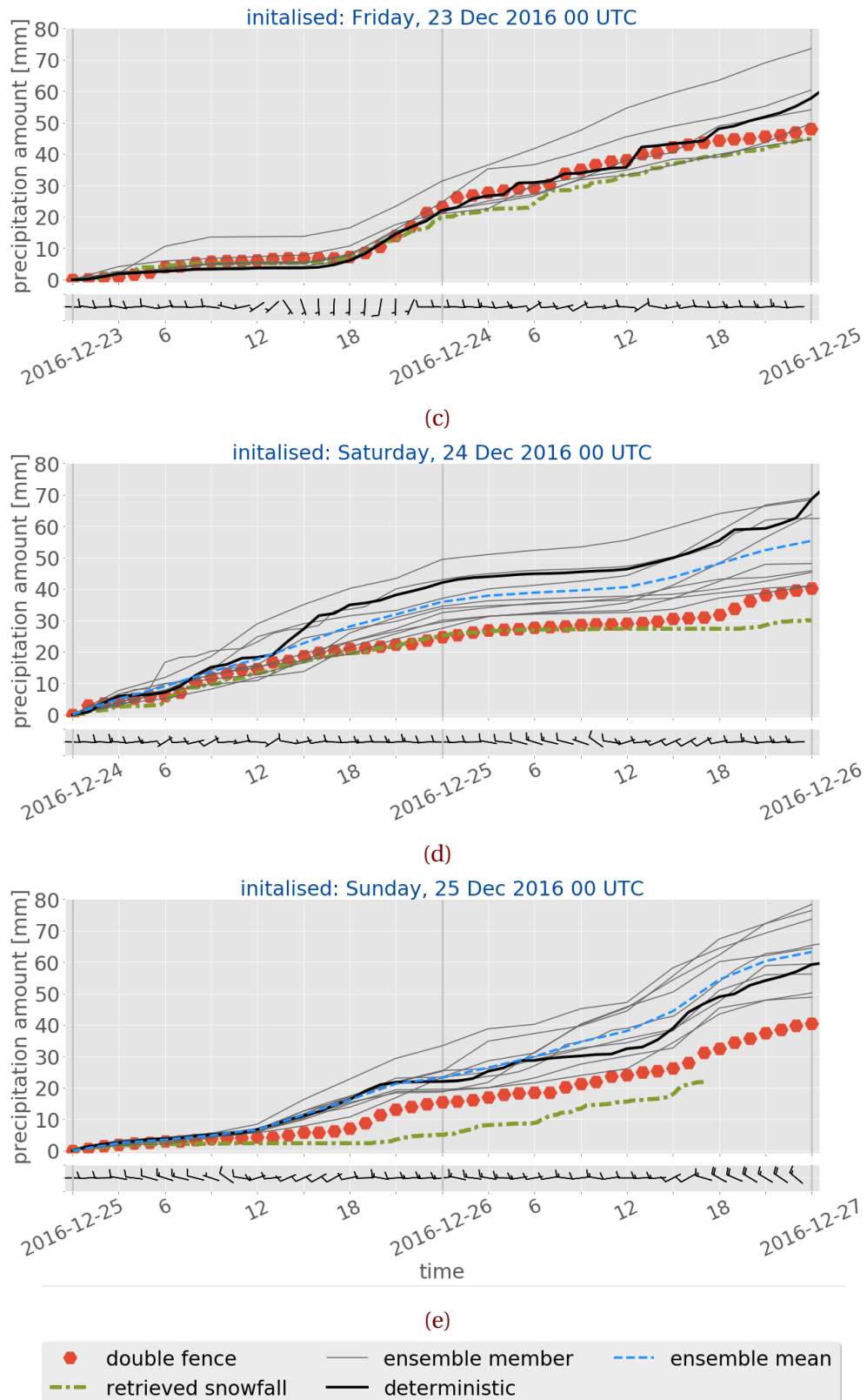
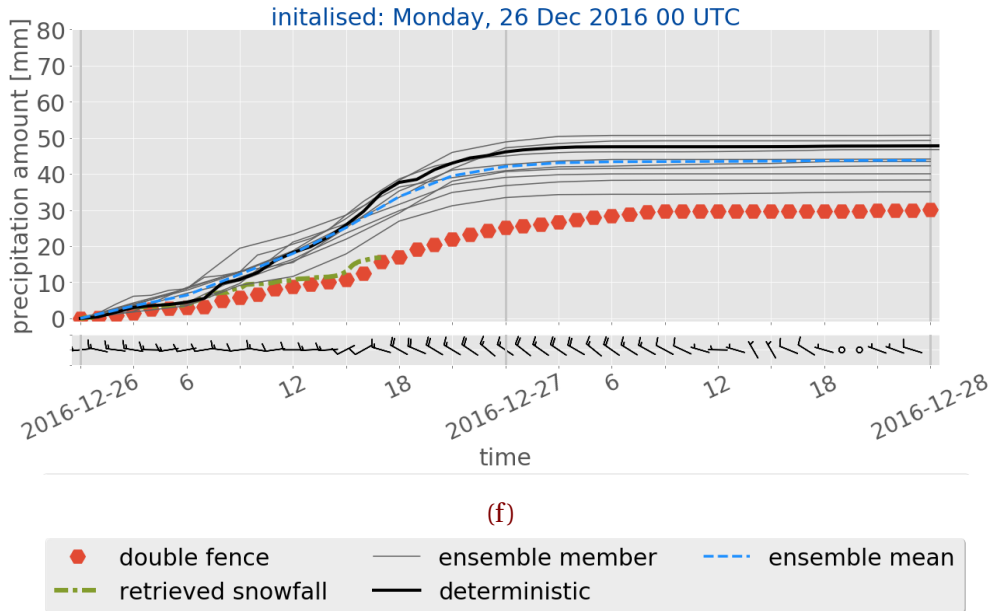


Figure 4.2.4: (Continued from previous page.)



**Figure 4.2.4:** (Continued from previous page.)

The correlation between 48 h double fence observation and ensemble precipitation forecast is presented in Figure 4.1.2a and b. Showing a better agreement for 21 to 23 December 2016 than initialisation on 24 to 26 December 2016. On 21 to 23 December 2016 the slope of the regression line is relatively close to unity, indicating a good agreement between MEPS forecast and the observations by the double fence. The largest disagreement between surface observations and forecasts is seen on 25 December 2016 with a wet bias up to 15 mm (Figure 4.1.4e). The mean absolute error is not larger than 13 mm for the first three days and increases with intensification of the storm up to 19 mm on 24 December 2016.

Initialisations on 24 December 2016 (Figure 4.2.4d) indicate an overestimation of the deterministic surface snowfall prediction already after 13 h forecast time. The deterministic forecast in solid black is much higher and increases faster than the observations. In Figure 4.2.4d at 16 UTC a difference of approximately 15 mm can be seen when compared to the surface measurements. This difference remains almost constantly over the forecast time. Furthermore, all ensemble members seem to overestimate the surface accumulation after 24 h.

Since MEPS performance was better on the previous days one might assume that the

**Table 4.2.3:** Observations (obs.) and forecasted (MEPS) snowfall amounts for the Christmas storm 2016. Difference refers to the percentage difference between MEPS ensemble members and the double fence observation, averaged over all ensemble member for 12 h and 24 h. The average difference is the value over all days.

Day in 2016	12 h accumulation					24 h accumulation				
	Snowfall		Difference	Average difference	Snowfall		Difference	Average difference		
	obs.	MEPS			obs.	MEPS				
	[mm]		[%]				[mm]	[%]		[%]
20 Dec	0.1	0.4	+290.7			0.1	0.4	+302.1		
21 Dec	0.7	5.1	+626.1			17.1	18.5	+8.3		
22 Dec	13.6	13.4	-1.6	+1.3		25.6	31.3	+22.2	+10.8	+32.6
23 Dec	6.3	6.6	+4.2		+134.7	23.3	23.7	+1.8		
24 Dec	14.7	17.7	+20.4	+59.8		24.8	35.9	+44.8	+54.4	
25 Dec	4.3	6.7	+55.1			15.4	23.3	+50.8		
26 Dec	8.8	17.9	+104.0			25.1	42.1	+67.5		

double fence measurement is influenced by surface winds. It shows in Figure 4.2.4d that the 10 min average wind at 13 UTC increases from  $5 \text{ ms}^{-1}$  to  $10 \text{ ms}^{-1}$  (see also Figure 4.1.1i). Wolff [2018] states that the double fence gauge is influenced by wind, and that the double fence gauge underestimates precipitation accumulation within 10 % for winds up to  $9 \text{ ms}^{-1}$ . Table 4.2.3 shows the difference between the observations and ensemble mean MEPS forecast for 12 h and 24 h. As seen in Table 4.2.3, the average difference error decreases with longer forecast time. For 21 to 26 December 2016 the average difference error is +134.7 %. For longer lead times, 24 h, the average difference error is reduced to +32.6 %. The daily percent difference show to be high for the last three days of the 2016 Christmas extreme event. On 21 December 2016 very large difference error (626.1 mm) is shown. This error is related to the small precipitation amount (0.7 mm) observations at Haukeliseter, which is a known difficulty for precipitation forecasts [Müller et al., 2017]. Generally the forecast accuracy decreases with lead time [Kalnay, 2003].

**Table 4.2.4:** Same as Table 4.2.3, just for an under-catchment of 10 % difference by the double fence gauge.

Day in 2016	12 h accumulation					24 h accumulation				
	Snowfall		Difference	Average difference	Snowfall		Difference	Average difference		
	obs.	MEPS			obs.	MEPS				
	[mm]	[%]		[%]		[mm]	[%]	[%]		
20 Dec	0.1	0.4	+251.6			0.1	0.4	+261.9		
21 Dec	0.8	5.1	+553.5			19.0	18.5	-2.5		
22 Dec	15.1	13.4	-11.4	-8.8	+111.2	28.4	31.3	+9.9	-0.3	+19.3
23 Dec	7.0	6.6	-6.2			25.9	23.7	-8.4		
24 Dec	16.3	17.7	+8.4			27.6	35.9	+30.3		
25 Dec	4.8	6.7	+39.6			17.1	23.3	+35.8		
26 Dec	9.8	17.9	+83.6			27.9	42.1	+50.8		

While the cyclone moves closer to Norway, the forecast inaccuracy of the surface precipitation increases. Overestimation occurs around 12 UTC on 25 December 2016. This overestimation of the precipitation amount could be associated with the warm sector evolution at Haukeliseter (Section 4.1.1). Afterwards it shows, with increasing lead time the same accumulation is predicted, but too high compared to the double fence observations. The wind at Haukeliseter was higher than  $10 \text{ m s}^{-1}$  (Figure 4.2.4e) before 12 UTC. A relation between high wind and double fence observation could be possible. Assuming an accumulation underestimation of 10 % would lead to a reduction of overestimation to 40.2 % for 12 h (Table 4.2.4). Table 4.2.4 presents the percentage difference between the double fence and MEPS forecasts. Here, it also shows a decrease in forecast accuracy for precipitation accumulation over 24 h. Table 4.2.4 displays a reduction of over estimation for surface accumulation on 24 to 26 December 2016. The average difference is reduced by 16 %. This shows, even though a 10 % under-catchment of the double fence gauge was present, would MEPS overestimate the surface accumulation (12 h: +43.8 %; 24 h: +39 %).

An overestimation of the surface precipitation is also observed on 26 December 2016. While the surface analysis indicates the passage of an occlusion after 15 UTC (Figure 3.6.2n, 3.6.2p, Section 4.1.1), suggests Figure 4.2.4f an overestimation after 12 h lead time. Again, the MEPS ensemble seem to predict the occurrence of precipitation correctly compared to the double fence, but estimates a too high surface accumulation. The surface wind observation in Figure 4.1.1s suggest also high wind speed up to  $17.5 \text{ ms}^{-1}$  observations on 26 December 2016. The difference error in Table 4.2.3 is +104 % for 12 h accumulation on 25 December 2016. This shows the highest overestimation for the three days (24 to 26 December 2016). The application of the 10 % under-catchment on the double fence observation would still follow an error of 83.6 % (Tables 4.2.3 and 4.2.4). It seems even though the double fence gauge is influenced by wind, the overestimation of surface accumulation by MEPS is still present.

Whereas the spread between the ensemble members is large in the beginning of 24 December 2016, the variability between the members is narrow for 25 and 26 December 2016 for the first 6 h. The variability between the ensemble members can be compared with a box-whisker plot. A box-whisker-plot shows the time evolution of the distribution of the precipitation amount made of ten ensemble members up to 48 h. Since some ensemble member do not have forecast values every hour the box-whisker-plot in Figure 4.2.5 provides information every 3 h. The red line shows the ensemble mean of all ten members and if the distribution is skewed. The short light green, horizontal line is showing the median, the wide vertical box represents the 25th and 75th percentiles, and minimum and maximum values are indicated by the vertical lines, whiskers.

The box-whisker-plot in Figure 4.2.5 displays the distribution of the ten ensemble members for the respective days. All three days with overestimation seem to have different variability. As expected increases the forecast uncertainty with longer forecast time for precipitation amount.

The variability in Figure 4.2.9 show on 25 December 2016 no large variation between the ensemble members (narrow box-whiskers). This day is also the forecast with the smallest wet bias of the three days with overestimation (Figure 4.1.4e). More variation between the ensemble members is shown on 24 and 26 December 2016 after 3 h. As the correlation for precipitation amount in Figure 4.1.2j suggests, the overestimation is not as high as for 24 and 26 December 2016. On 24 and 25 December 2016 the mean error for the surface accumulation is largest with values up to 7 mm for 12 h (Figure 4.1.5e).

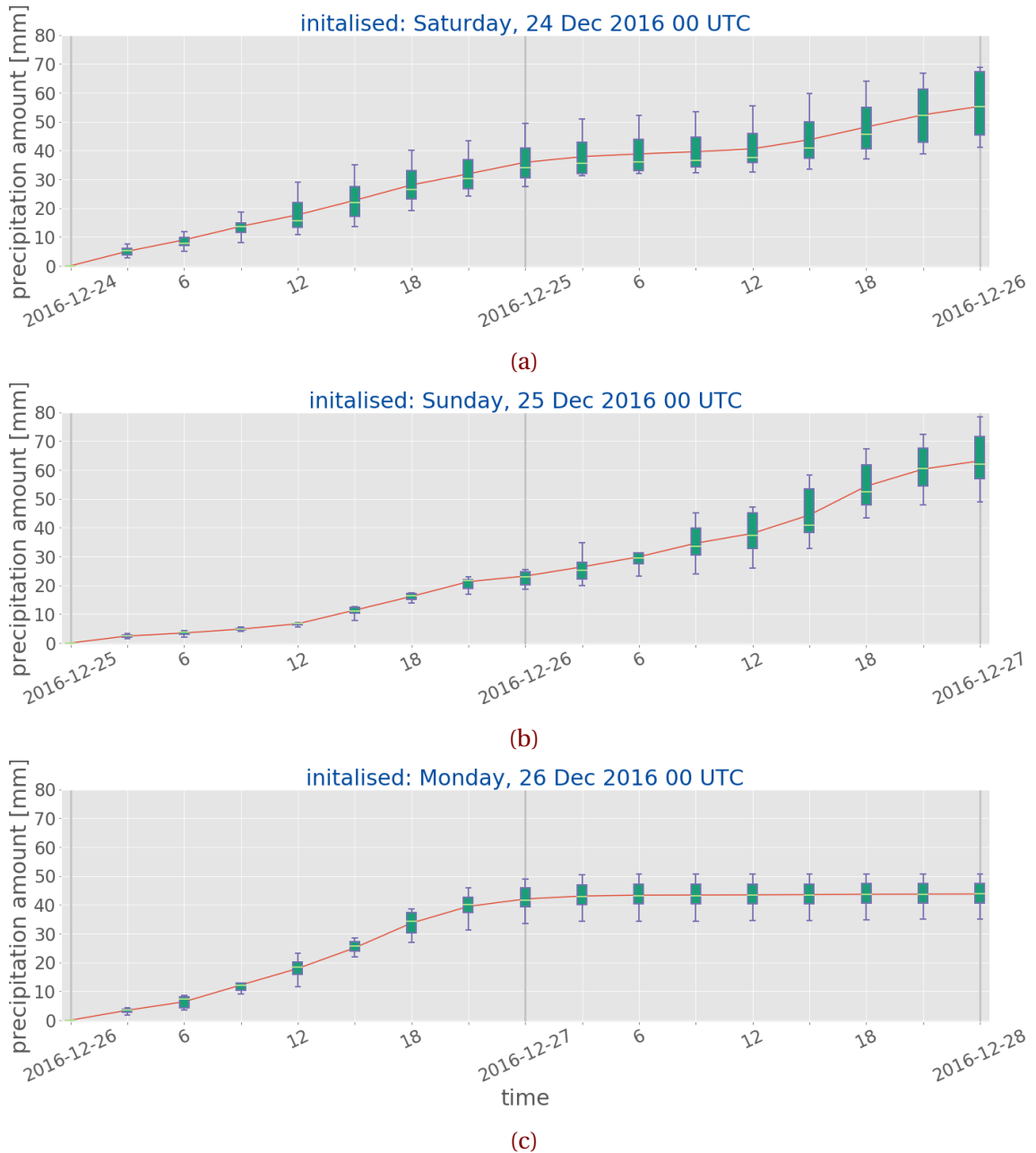


**Figure 4.2.5:** Box-whisker-plot of the ten ensemble members of MEPS. Red line indicating the ensemble mean, lower and upper whisker the 25th and 75th percentile, respectively. Light green shows the median of all members and the box represents the middle 50 % of scores of the precipitation.

Larger variability is already present after 3 h prediction time in Figure 4.2.5a on 24 December 2016. The spread between the ensemble members (shown by the minimum and maximum whiskers) seems to be wide indicating a larger uncertainty about the amount of surface accumulation. The ensemble mean (red line) is always higher than the median, suggesting a positively skewed distribution. After 12 h forecast time, the median is closer to the lower 25th percentile, indicating a negative skewness. Also, all upper whiskers in Figure 4.2.5a are longer than the lower ones, which would follow that the ensemble members vary amongst the most positive quartile and that it is very similar for the least positive quartile group.

I believe that the uncertainty appearing already after 3 h (Figure 4.2.5a) could be associated with a too long spin-up time of MEPS. MEPS usually has a spin-up time of about three hours, on 24 December 2016 this might have been longer as a result of poorer initial conditions [Need a reference here, not stated in Müller et al. \[2017\]](#). It seems, that the initial and boundary conditions for MEPS might have not been perfect for initialisations on 24 December 2016 at 0 UTC. As described in Section 2.5 should the perturbed members always lie relatively close to the observations. For a short time (hours) should the forecast member be close together [[Kalnay, 2003](#)]. The deterministic and perturbed members might not to have stabilised yet and show larger variation in Figure 4.2.5a from early on than e.g. on 25 December 2016. More variability between the ensemble members do not necessarily mean, that a forecast is bad, it only shows the uncertainty of the initial conditions. Important is, that the observations, which are going to be used for the initialisation are within the spread of the ensemble member prediction.

The uncertainty might also have been related to the fact that the large-scale situation got more complex. The precipitation amount associated with the transition of an occluded front on 23 December 2016, after 18 UTC, is higher than on the previous days (Figure 4.1.1j and Figure 3.5.1). During 20 to 21 December 2016, the hourly precipitation around 0 UTC is less intense than on 23 December 2016 (Figure 3.6.2e). High accumulation amount over shorter time followed and could have resulted in a larger variability of the MEPS members (Figure 4.2.5). Another possibility is MEPS might have accounted for additional accumulation around 12 UTC on 24 December 2016 and this showed a stronger increase in accretion in Figure 4.2.4d at 13 UTC. I believe it could be associated to a local resolution effect of MEPS at Haukeliseter, which will be further discussed in Section 4.2.5.

Figure 4.2.5b and c show a smaller ensemble member variability on 25 December 2016 and 26 December 2016 than on 24 December 2016. The box-whiskers are narrower for the first 30 h in Figure 4.2.5b, but slightly larger after 6 h forecast time for initialisations on 26 December 2016. Section 4.1.1 presented a good agreement between observations and forecast of large scale features in terms of pressure, temperature and wind direction. While the occlusion on 26 December 2016 was more intuitive (Figures 4.1.1p to 4.1.1s) than the warm front development on 25 December 2016 (Figure 4.1.1k, l, m, n). The mean error in Figure 4.1.4 for each variable shows to be best on 25 December 2016 (Figure 4.1.5a,b,c, d, and e).

On 25 December 2016 the overestimation started to occur around 13 UTC in Figure 4.2.4e, and may be related to the delayed temperature MEPS forecasted temperature increase in Figure 4.1.1l. As Figure 4.2.5b shows, the variability in the forecast increases after 15 h prediction time. In general, median and mean agree well for the entire period of a 48 h lead time. After 39 h the mean is much higher than the median and closer to the lower 25th percentile in Figure 4.2.5b. It seems, that all ten ensemble members agree well on the prediction and nevertheless MEPS overestimates the surface accumulation. The MEPS surface forecasts on 25 December 2016 suggest that MEPS did not expect the occurrence of a warm front (Figures 4.1.1k to 4.1.1n). However, the surface accumulation prediction could suggest that MEPS expected more precipitation around 12 UTC. Maybe MEPS has expected a weak warm-front passage and therefore more precipitation. The fact that the temperature is rising and therefore the phase is changing from snow to liquid precipitation (Figure 4.1.3) may have led to MEPS expecting more liquid precipitation rather than mixed phase precipitation and hence MEPS predicted more surface accumulation.

Between 15 UTC and 18 UTC on 26 December 2016, the core of the low-pressure system passes over Haukeliseter Figures 4.1.1p to 4.1.1s. The box-whiskers in Figure 4.2.5c indicate a larger variability after 6 h prediction while the precipitation amount forecast is overestimating at 12 UTC. The forecast precipitation amount is similar to the double fence observations, but overestimated. Variability of all ensemble members increases at 6 h lead time, but then decreases again in Figure 4.2.5c.

Since the box-whisker-plot in Figure 4.2.5b and c (25 and 26 December 2016) show less variability in the beginning it is assumed that spin-up time issues are less likely, but not totally excluded. It could be related to an error in the initialisation state, even though it does not show within the variability at the beginning. In Figure 4.2.4e and f, the ensemble

mean agrees well with the deterministic forecast, which is an indication of a symmetrical spread around the deterministic run. Again, the ensemble mean is the best statistical solution over a longer timespan and does not necessarily mean to be the best for an extreme event such as the Christmas storm 2016.

The overestimation of accumulated precipitation during 24 and 26 December 2016 might be related local topography as well as to the complex development of the low-pressure system north-west of Norway on 24 December 2016. Furthermore could it be related to the 10 % under-catchment by the double fence gauge under high wind condition.

According to Müller et al. [2017] strong precipitation events are better predicted with AROME-MetCoOp than with ECMWF. In Section 2.2 it was described, that during 21 to 27 December 2016 56.9 % of the total December 2016 accumulation of precipitation were observed. In December 2014, the 12 h precipitation mean absolute error in AROME-MetCoOp was below 1.5 mm [Müller et al., 2017]. For the 2016 Christmas storm the mean absolute error is not larger than 5 mm for the first 12 h of accumulation on 24 and 26 December 2016 (Figure 4.1.5e). Therefore, the assumption follows that on 26 December 2016 the overestimation might be correlated to the <10 mm problem described by Müller et al. [2017]. The 12 h and 24 h accumulation is presented in Table 4.2.3 for Haukeliseter and shows that 12 h observed accretion was less than 10 mm for 25 and 26 December 2016. The mean error for 12 h accumulation in fact shows a wet bias during 24 and 26 December 2016.

#### 4.2.4 COMPARISON OF SNOW WATER CONTENT IN THE VERTICAL

Frontal boundary passages were observed at the surface several times throughout the extreme storm in December 2016. MEPS is able to predict the large scale features and related surface changes for initialisation more than 24 h before (Section 4.1.1). In winter 2016 three additional instruments were installed to estimate the vertical snow water content at Haukeliseter. This unique approach gives the opportunity to compare the vertical forecasts of SWC to vertical solid precipitation observations.

Previous studies such as Joos and Wernli [2012] motivate to make accurate surface measurements more available to improve mesoscale models.

Passages of occluded fronts and a warm sector were observed on 23, 26, and

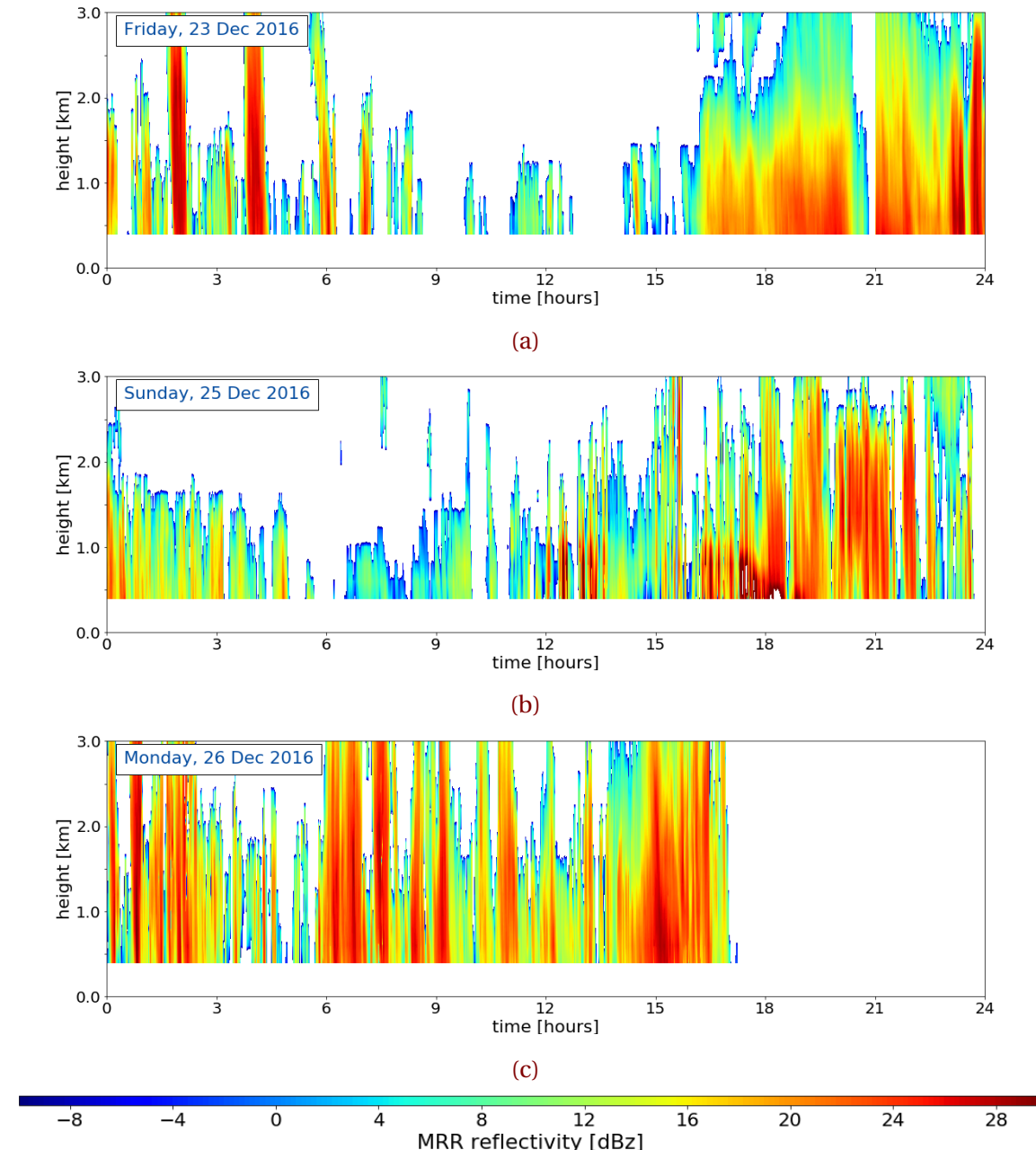


**Figure 4.2.6:** MRR reflectivity for the days when a front or an occlusion passed through at Haukeliseter. dBZ reflectivity according to the colour bar, with weaker precipitation in blue and more intense precipitation in red. **a:** Friday, 23 December 2016, **b:** Sunday, 25 December 2016, and **c:** Monday, 26 December 2016.

25 December 2016, respectively. Figure 4.2.6 shows the reflectivity from the MRR at Haukeliseter for these three days. Figure 4.2.6c presents only values until 17 UTC, because of the temperature change and hence a precipitation shift followed liquid drops freezing on the MRR dish and the signal got attenuated.

More consistent storm structure with higher reflectivity values indicate the transition of the boundaries in Figure 4.2.6. While on 23 and 26 December 2016 the reflectivity did not pass values larger than 28 dBZ shows Figure 4.2.6b high reflectivity values larger than 30 dBZ (compare for approximation Table 2.3.1). These high values indicate the observation of possible liquid precipitation. Images from the MASC were able to verify observed liquid drops during 12 UTC to 21 UTC (Figure 4.1.3).

On 23 December 2016, the surface observations allow to assume that the occluded front passed through between 12 UTC to 21 UTC (Figure 4.1.1f, g, h). The vertical observations at Haukeliseter show intense reflectivity and therefore more intense precipitation after 16 UTC (Figure 4.2.6a). Another occlusion passed through on 26 December 2016 shortly before 15 UTC which lasted until 21 UTC indicated by a more consistent storm structure and high reflectivity in Figure 4.2.6c around 15 UTC. The high reflectivity on both days shows the passage of the occlusion and the associated precipitation. On 23 December 2016, the wind is from the south, upslope (Figure 4.1.1h, Figure 2.1.1c) which led to a more consistent storm structure in Figure 4.2.6a. Figure 4.1.1m and n indicate strong wind observations from the west which led to a consistent, but shorter storm structure in Figure 4.2.6b at 15 UTC on 25 December 2016. The orographic influenced wind and therefore a possible relation to the precipitation will be further assessed in Section 4.2.5.

Figure 4.2.7 presents the reflectivity of the MRR and the snow water content retrieved from the reflectivity as well as the 48 h forecast values. Minutely MRR reflectivity and retrieved snow water content can be seen in Figure 4.2.7a, d, j, and m. Figure 4.2.7b, e, k, n show in the upper panel the hourly averaged values from the retrieved SWC and in the lower panel the ensemble mean of the instantaneous forecast values every hour over all ensemble member. Three hourly averaged retrieved values are then presented in the upper panel of Figure 4.2.7c, f, l, and o, the lower panel are the ensemble mean forecast values every three hours.

Figure 4.2.7e (lower panel) shows the one hourly averaged forecast values over all

ensemble members, neglecting not existing values on 23 December 2016. Forecasts initialised 48 h (22 December 2016) prior predict the consistent storm structure and therefore the passage of the front (Figure 4.2.7b, c). The consistent structure of retrieved snowfall after 16 UTC is predicted for initialisations less than 24 h before the occurrence of the occlusion (Figure 4.2.7d, e, and f). Even the three hourly resolved averaged forecast values show a response on the occurrence of the storm (Figure 4.2.7f, lower panel). The duration of the passage is between 16 UTC to 23 UTC (Figure 4.2.7a to f). MEPS is able to estimate the snow water content for time resolutions of 3 h in Figure 4.2.7c, f.

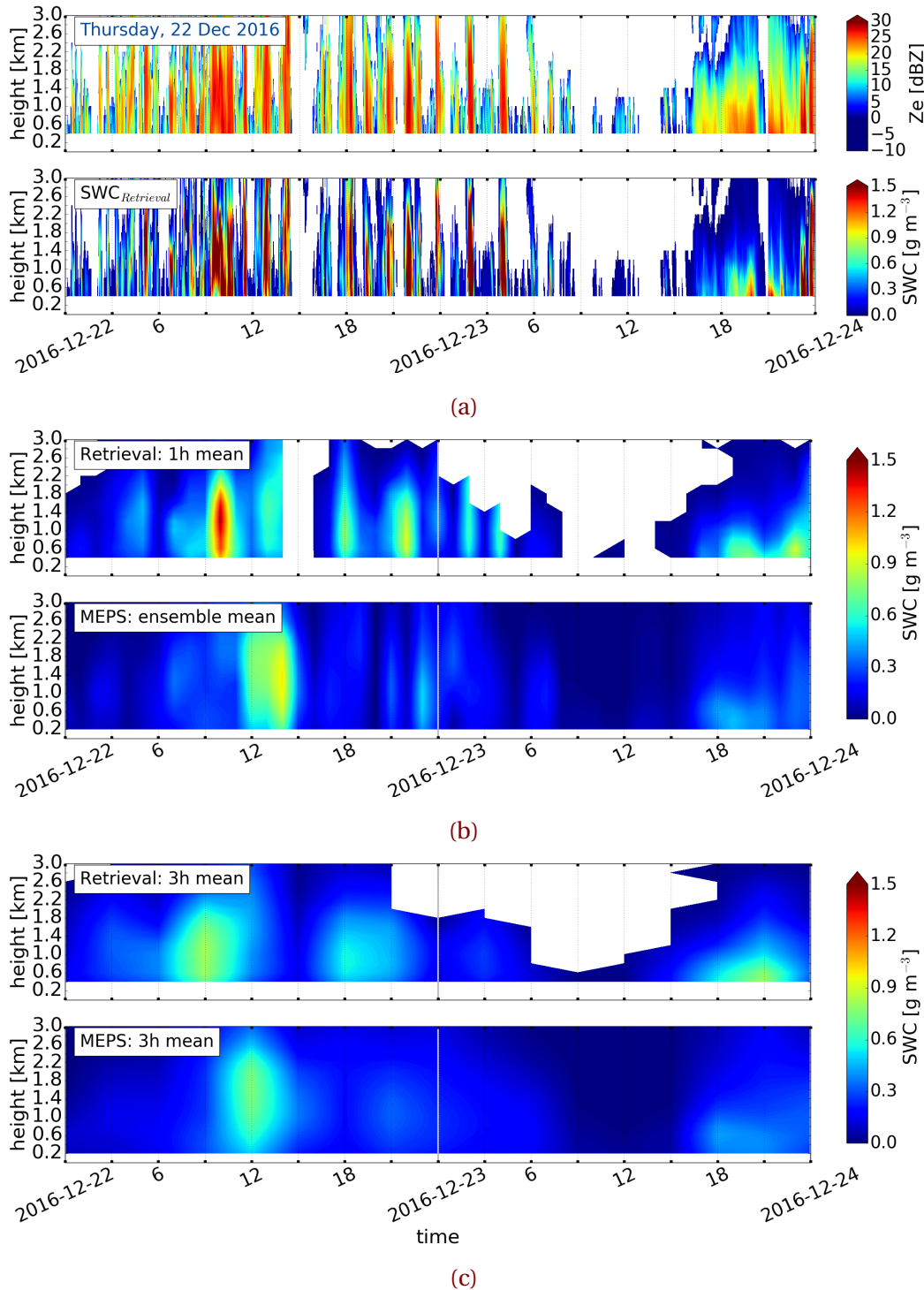


**Figure 4.2.7:** Initialisation on 22 December 2016 at 0 UTC. From top to bottom: (a) MRR reflectivity for 48 h, minutely retrieved SWC. (b) Hourly averaged retrieved SWC, lower panel instantaneous hourly averaged forecast of all ensemble member SWC, neglecting missing values. (c) Three hourly averaged retrieved SWC, lower panel instantaneous three hourly averaged forecast of all ensemble member SWC. *Continued on next page.*

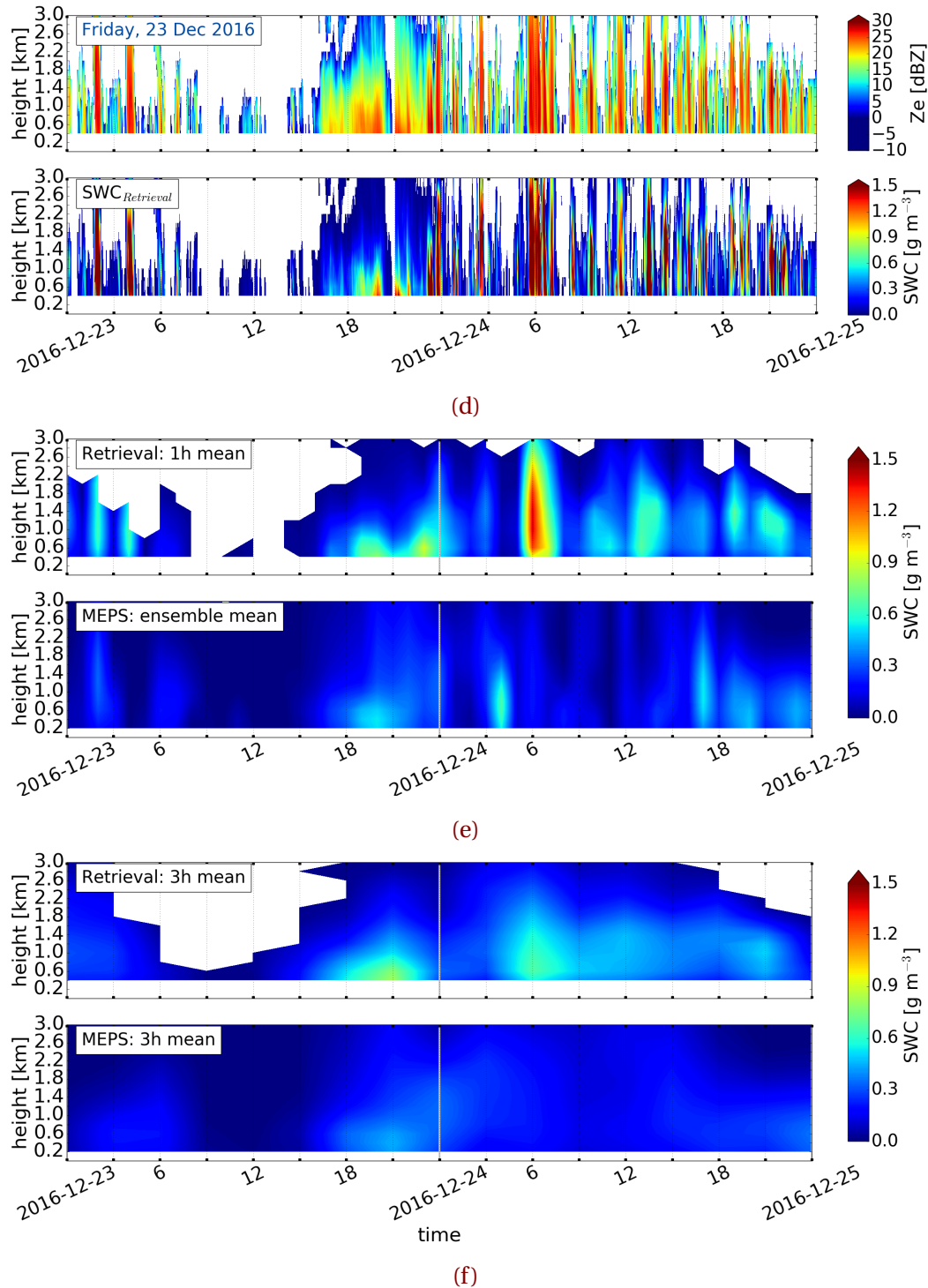


Figure 4.2.7: (Continued from previous page.) Initialisation 23 December 2016 at 0 UTC.

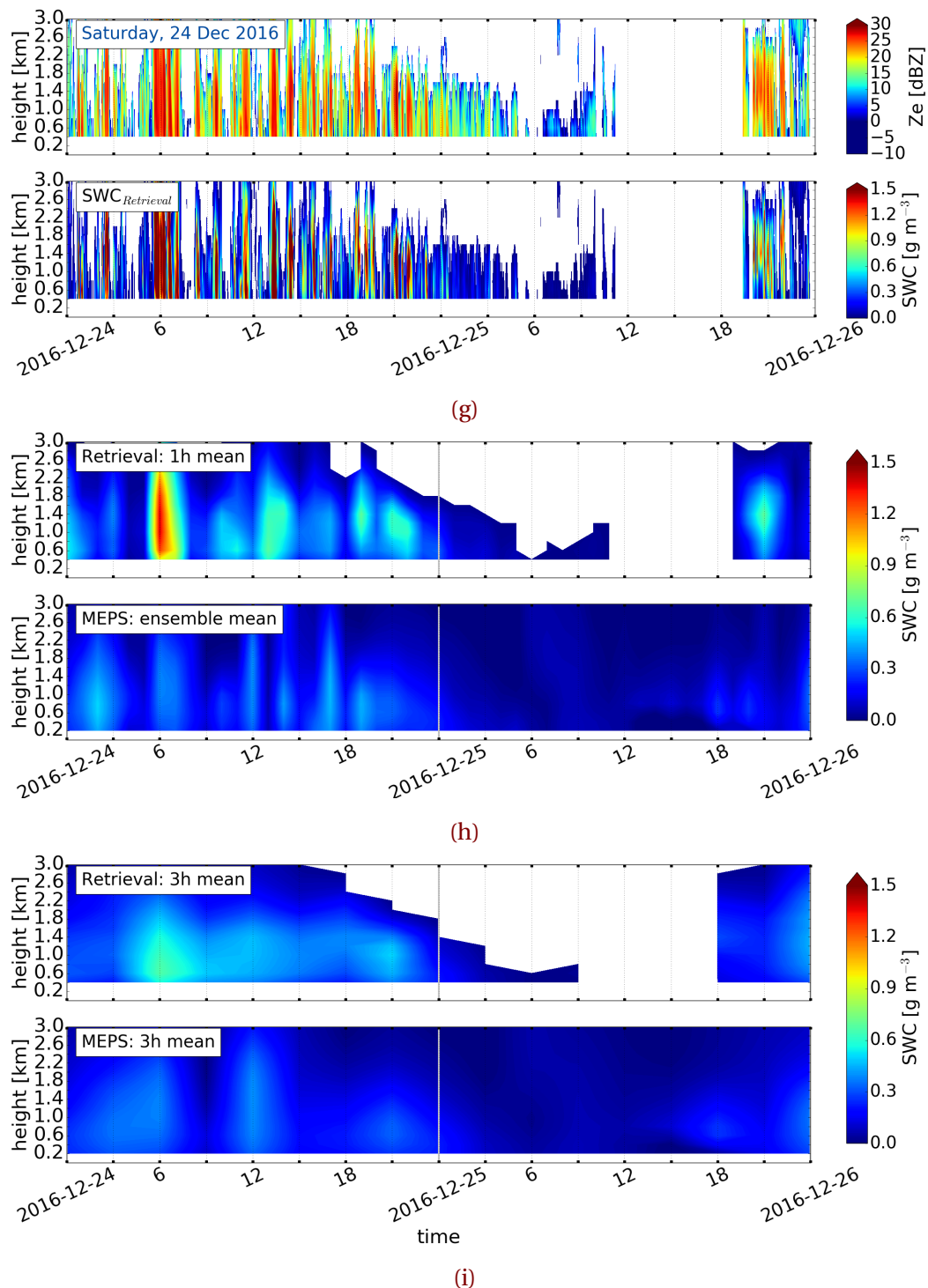


Figure 4.2.7: (Continued from previous page.) Initialisation 26 December 2016 at 0 UTC.

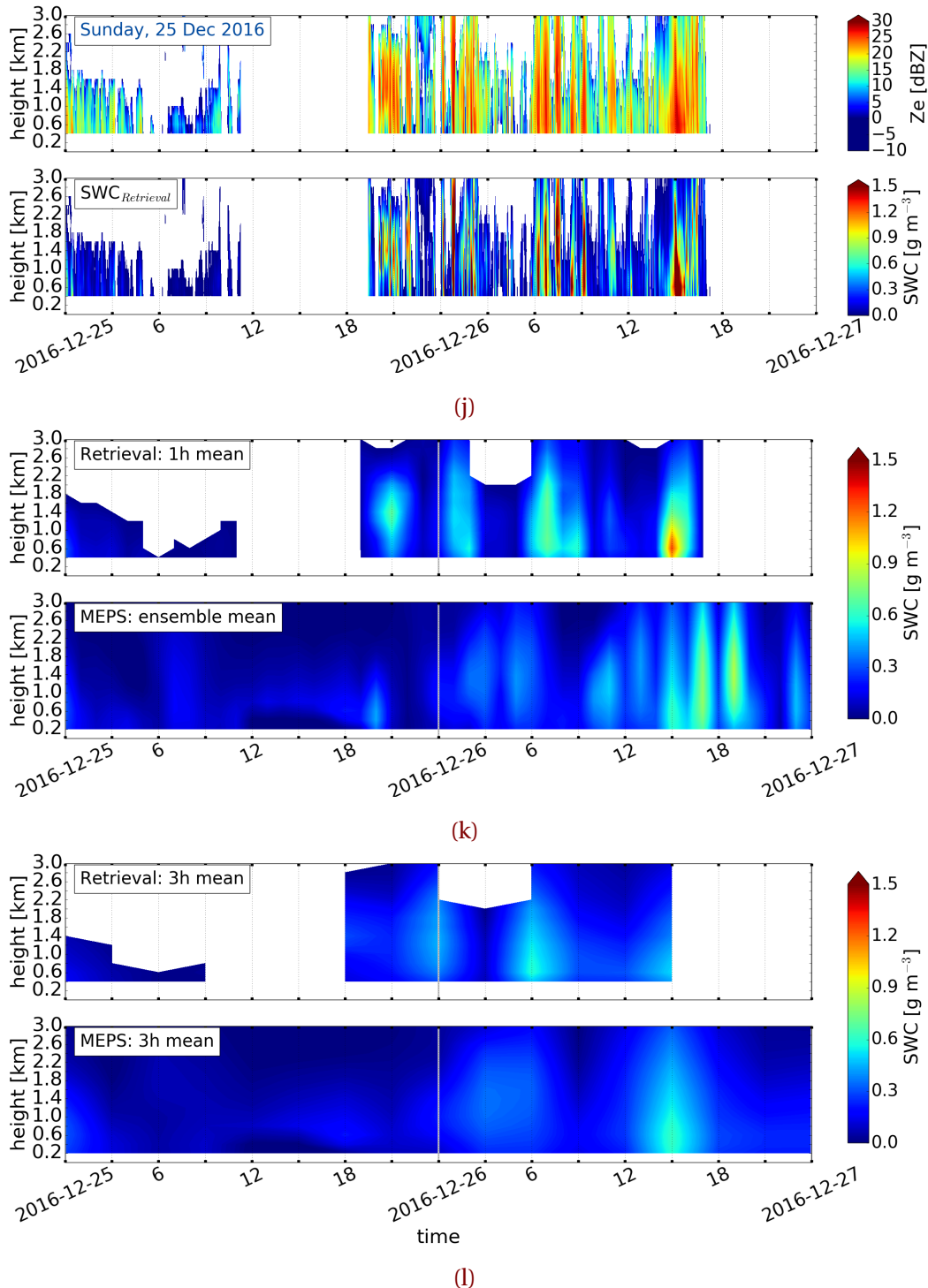


Figure 4.2.7: (Continued from previous page.) Initialisation 25 December 2016 at 0 UTC.

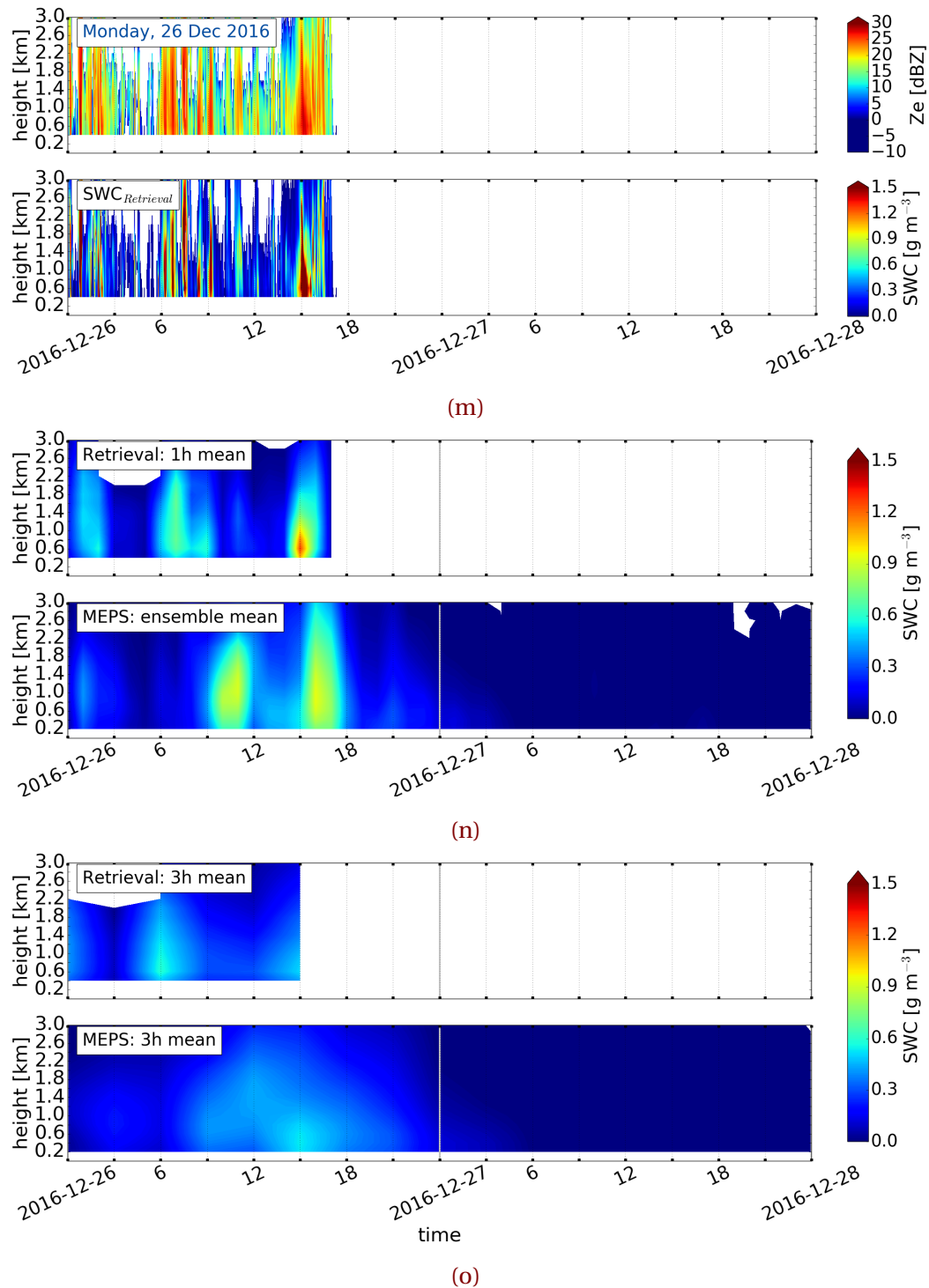


Figure 4.2.7: (Continued from previous page.) Initialisation 26 December 2016 at 0 UTC.

In general, the forecasted instantaneous snow water content amount is weaker than the retrieved values for predictions on 23 December 2016. Hourly averages, only using the deterministic forecast and the first ensemble member show no occurrence of the occlusion passage on either day (??). The variation of each initialisation ensemble member is given in Figure B.2.1 for the respective day In Figure B.2.1b the prediction for the occlusion passage is quite weak for all ensemble members

In the evening of 23 December 2016, the first perturbed ensemble member does not exist and hence little snow water content is predicted for the ensemble means especially for the hourly resolved mean Figure B.1.1b). A comparison with 25 and 26 December 2016 show the same result, when only the deterministic forecast and first perturbed member is used Figure B.1.1e and f.

On 26 December 2016, only retrieves snow water content until the passage of the occlusion is observed (Figures 4.1.1p to 4.1.1t. The average of all ensemble members (Figure 4.2.7n) as well as the three-hourly instantaneous SWC (Figure 4.2.7o) predict the frontal passage. Initialisations already 39 h prior let assume that intense precipitation over a short time will occur (Figure 4.2.7k, l). The variation of all members in Figure B.2.1e and f indicate that almost all perturbed members would have predicted the precipitation around 16 UTC, but the ensemble mean weakens the result. On 25 and 26 December 2016 high predicted SWC values are calculated for the deterministic forecast, than for any other ensemble member. This bias might have led to an overestimation at the surface on 26 December 2016, where the deterministic forecast indicates higher values than the perturbed members (Figure 4.2.4f). But in Figure B.1.1e and f the amount of snow water content is very weak. Better estimations for predicted snowfall amount are displaye for the use of all ten ensemble member with either hourly or three hourly time resolution to creat the ensemble mean. Still, the instantaneous average values of all ensemble members are much weaker than the retrieved SWC.

In the observations on 25 December 2016, patterns of possible liquid precipitation (Figure 4.1.3) related to warm temperatures (Figure 4.1.1l) and high reflectivity (Figure 4.2.6b) are shown, between 12 UTC to 21 UTC. High reflectivity values in Figure 4.2.6b are present around 18 UTC with layer thickness up to 1.2 km. To see if liquid precipitation is predicted, the atmospheric cloud condensed water content and rainfall amount in model levels is summed (Figure 4.2.8). Figure 4.2.8a and b show liquid water content for initialisations on 24 December 2016 or 25 December 2016, respectively. Positive surface temperatures

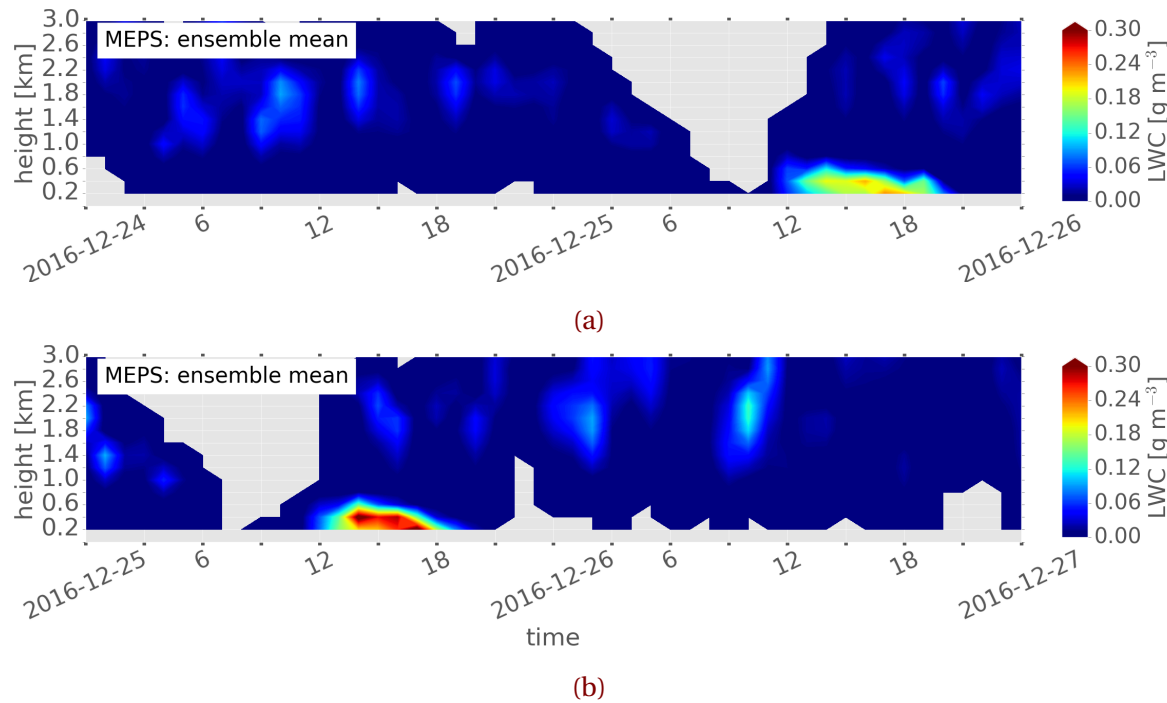


**Figure 4.2.8:** 200m hourly averaged LWC forecast from MEPS with all ensemble members, neglecting missing values. Initialised on 24 December 2016 and 25 December 2016 at 0 UTC. Liquid water content according to the colorbar.

were forecasted between 12 UTC and 21 UTC (Figure 4.1.11). Initialisations more than 24 h prior show already the occurrence of the liquid layer (Figure 4.2.8a). Figure 4.2.8a or b show also a narrow liquid layer thickness up to 800 m.

In Norwegian mountainous terrain this is an important forecast ability, since precipitation change can lead to a high risk for people. The avalanche danger increases with the precipitation change especially during high wind speeds [Hansen et al., 2014]. Since MEPS forecasts the liquid layer correctly in thickness and duration it seems to be a good interaction between the surface model temperature and the temperature assimilation. This follows a high accuracy of MEPS and the positive impact of using a high resolution convective scheme model.

For the first glance operates MEPS well when compared to vertical observations, even though weaker ensemble mean estimates occur compared to the observations. One

**Table 4.2.5:** Interpretation of the coefficient of variation for SWC.

<b>Size of CV [%]</b>	<b>Interpretation variability</b>
0 to <25	negligible
25 to <50	low
50 to <75	moderate
75 to <100	high
100 to $\infty$	very high

possibility to assess the variability of all ensemble member is with the use of the coefficient of variation (CV) described in Section 2.6.4. Figures 4.2.9a to 4.2.9d show the coefficient of variation for SWC.

The grey line in Figure 4.2.9 presents the ensemble mean of the hourly predicted SWC values. The darker the shading in Figure 4.2.9 the smaller the variation of the SWC relative to the mean.

MEPS data does not exist for all ten ensemble members on 23 December 2016. No coefficient of variation is calculated for this day, since only six perturbed members were available. Therefore, the initialisation on 22 December 2016 is used to validate the forecast. The interpretation of the coefficient of variation for SWC is presented in Table 4.2.5.

All ensemble members agree well with the occurrence of the up-slope storm on 23 December 2016 after 15 UTC (Figure B.2.1b). For prediction initialised on 22 December 2016 the verification in Figure 4.2.9a shows little variability below 50 % and show a good agreement on the occurrence of snow precipitation. All ten ensemble members forecast the up-slope to occur after 16 UTC, compare Figure B.2.1b and c. The comparison of only six ensemble members in Figure B.2.1c, let assume that the variability between all ensemble members during the up-slope storm is low, but not as certain as for an initialisation on 22 December 2016 at 0 UTC. The deterministic forecast (EM0) and ensemble member one in Figure B.2.1b indicate peaks of high SWC before 8 UTC. The retrieved SWC on 23 December 2016 had two peaks, one at around 2 UTC and another at 4 UTC. The deterministic forecast, initialised on 22 December 2016 predicted a peak at

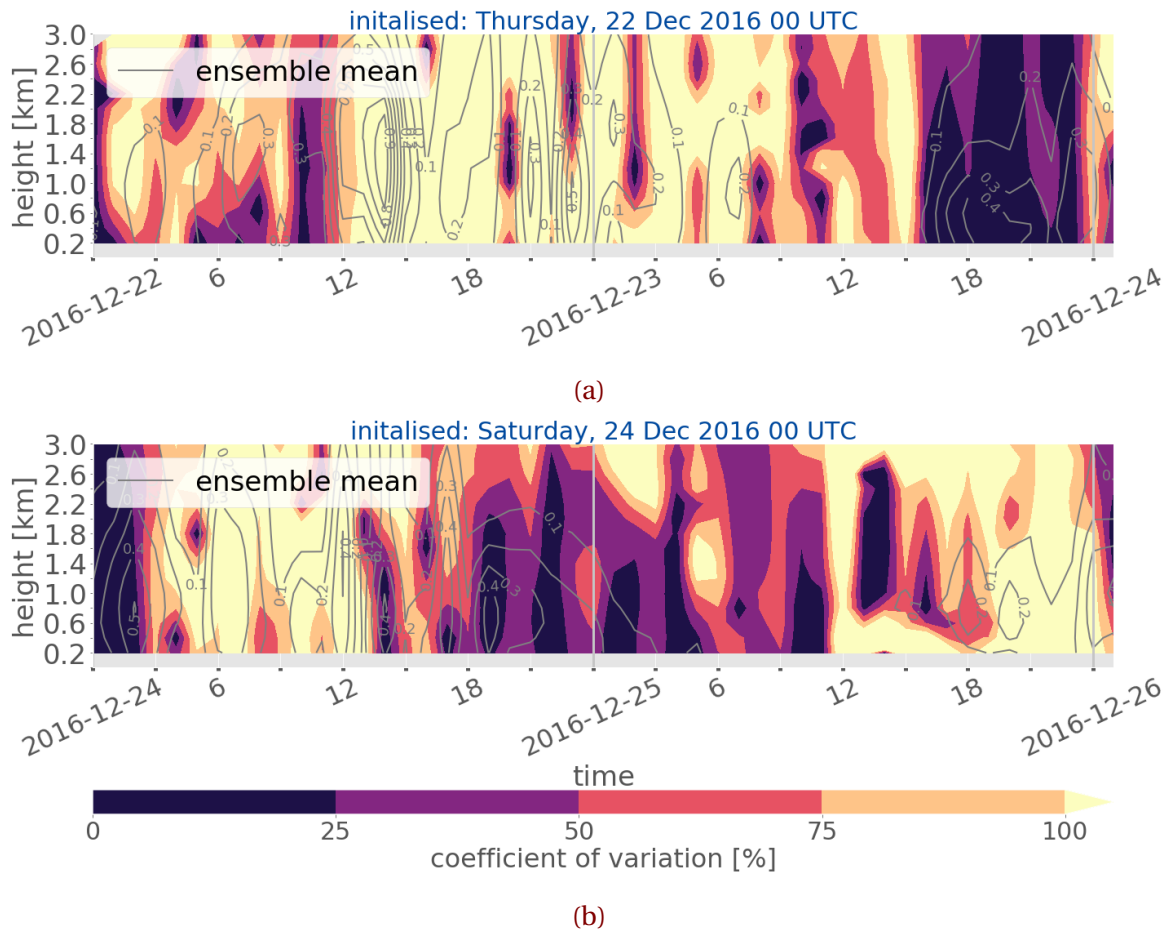


**Figure 4.2.9:** SWC variation of the ten ensemble members of MEPS. The lighter the colour according to the colour bar the higher the variation between the perturbed ensemble members. In grey the ensemble mean of all ten members. For initialisations on 22 and 24 December 2016. *Continued on next page.*

2 UTC, 6 UTC and 8 UTC, where the first perturbed ensemble member (EM1) has a strong SWC at 7 UTC. Overall seems a combination of the deterministic and first ensemble member of the 22 December 2016 initialisation to be a good forecast when comparing to the retrieved SWC in Figures 4.2.7a to 4.2.7d.

A larger variability between the ensemble members is shown for the evolution of the occlusion on 26 December 2016 in Figure 4.2.9d. In general, the 25 December 2016 was a very weak snow storm with strong liquid precipitation observed between 12 UTC and 18 UTC. Initialisations on 25 December 2016 (Figure 4.2.9c) present a lower variability for

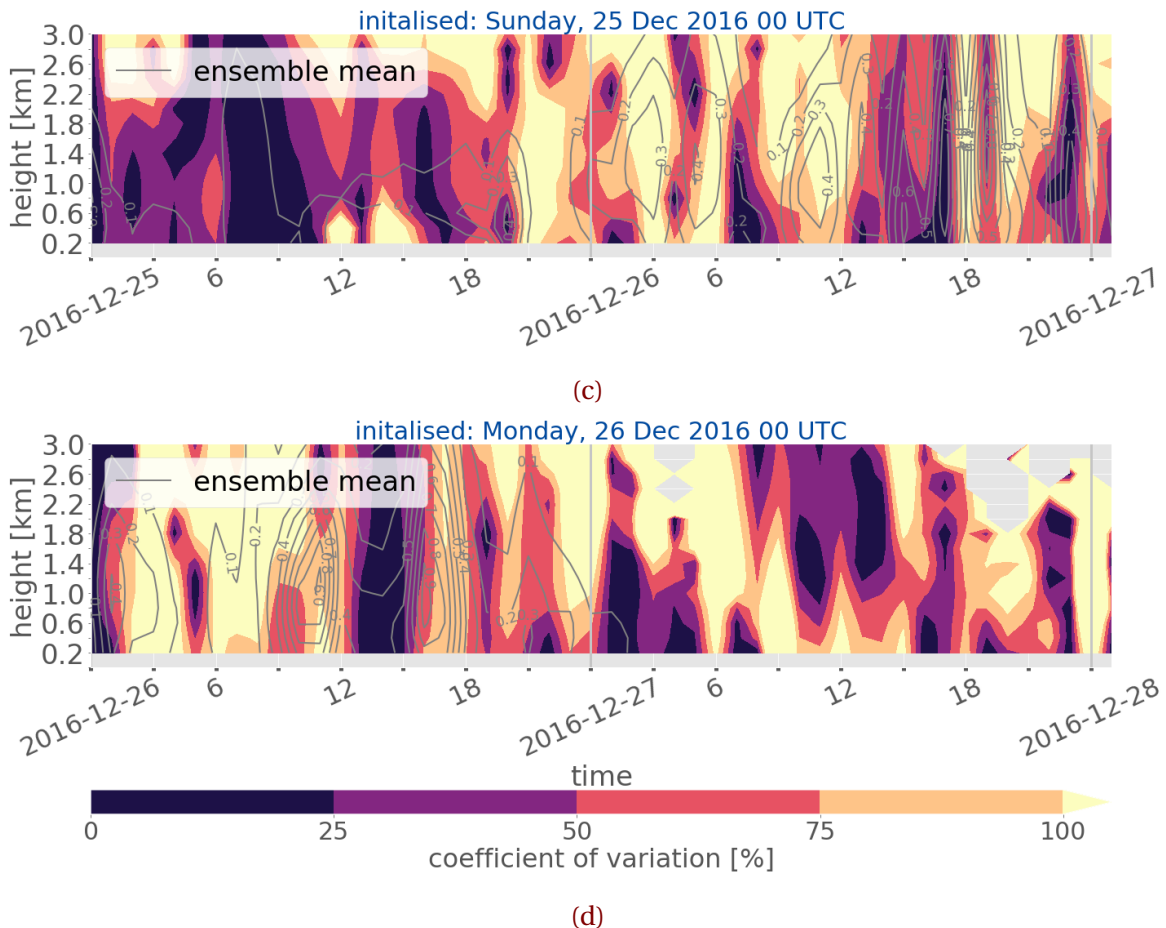


Figure 4.2.9: (Continued from previous page.) Initialisation 25 and 26 December 2016.

the transition after 15 UTC on 26 December 2016 than initialisations less than 24 h prior. Therefore, an increase of variability after shorter time is given rather than long lead time (48 h). Figures 4.2.7g to 4.2.7i and Figures 4.2.7j to 4.2.7l give a low value of predicted SWC in the course of a day. As Figure 4.2.9b indicates is the forecast accuracy very high up to 1.8 km until noon, this is when liquid precipitation was measured. The depth of the liquid layer was up to 0.8 km in Figure 4.2.8a and 4.2.8b. The variation coefficient (Figure 4.2.9b and 4.2.9c) has a large disagreement below 0.8 km, but above the variability is between the members not existing or low. Initialisation on 24 December 2016 show weak snow water content peak in Figure 4.2.7h and i at 18 UTC, which had a moderate variability (Table 4.2.5, Figure 4.2.9b). Afterwards it is very high. Initialisation on 25 December 2016 the forecast variability is low until noon (Figure 4.2.9c). While liquid precipitation was

monitored the variability in the lower layer is first very high and shortly before 18 UTC not existing. A high agreement for the SWC peak at 20 UTC up to 0.8 km exists in Figure 4.2.9c and decreases to be moderate above.

Figure 4.2.7k and l would suggest a continues pulsing of the storm. The two peaks around 18 UTC (Figure 4.2.7k) are predicted with a negligible and moderate variability in ???. The SWC peaks at around 3 UTC and 5 UTC show a very high variability. Figure B.2.1e displays that four out of ten ensemble members would agree with the peaked event around 5 UTC. Whereas the peak at 3 UTC is dominated by the strong predicted SWC of the deterministic forecast, which follows the high variation in Figure 4.2.9c. Initialisation on 26 December 2016 follow that the SWC peak at 1 UTC is related to a moderate variability of the ensemble members. Low forecast accuracy is shown for the SWC between 9 UTC to 12 UTC and the one between 15 UTC to 18 UTC has a low to moderate variability between the members. When looking at Figure B.2.1f might this disagreement be related to the colourful variation of the vertical predicted SWC. There seems to be no agreement between the different members about the incidence of the SWC peaks. The high conflict for the CV before noon is most likely related to the high SWC of the deterministic SWC. Again, this is not a fair comparison since hourly instantaneous values are used and there might be a time delay of half an hour about the development of boundaries which would follow it is not seen in the model forecast.

One question to answer in this work is if the operational model MEPS estimates large scale features correctly. As discussed here and in Section 4.1.1 it seems that the model is able to cover the development of large scale features and its associated precipitation. Even with the intensification of the storm MEPS seem to be able to predict extreme events for vertical snowfall such as the 2016 Christmas extreme event, but might have some issues predicting transitions of frontal boundaries as well as associated precipitation at the surface.

MEPS is also able to distinguish between liquid and solid precipitation in layer thickness and duration for time resolution of one hour. This can be a major advantage since a change in temperature and associated precipitation transformation can lead to high safety issues in the Norwegian mountains, especially during winter. With the knowledge more than 24 h prior can risk notice be send out to the population and rescue teams can prepare in advance. Furthermore, roads and train tracks can be closed to increase the safety.

The here presented results are a first look, trying to compare a mesoscale ensemble member forecast system (MEPS) with vertical in-situ measurement for snowfall.

The next section will go into detail, how the local orography at Haukeliseter may influence frozen precipitation, and how MEPS's representation of the topography may affect it.

#### 4.2.5 OROGRAPHIC INFLUENCE ON PRECIPITATION

The Haukeliseter site is suspended to high wind speeds during the winter. The previous results in Section 4.1.1, 4.2.3, 4.2.4 have shown, that wind plays an important role for the precipitation at Haukeliseter. The mountain plateau is surrounded by higher mountains to the west and more open to the south east (Figure 4.2.10a), this orography seems to influence the vertical precipitation pattern. The correlation between wind speed observations and forecast show an overestimation of predicted wind speed throughout the event (Figure 4.1.1d, i, n and s). Müller et al. [2017] already mentioned the weakness of too strong wind prediction in AROME-MetCoOp, the previous operational deterministic version of MEPS.

Figure 4.2.10b shows the MEPS resolution and its 2.5 km grid cells around the Haukeliseter site. The complex terrain and its representation in MEPS might have followed the overestimation of accumulation. In this thesis the closest grid point to the Haukeliseter measurement site is used. Alternatively, the use of an average of the grid points surrounding the Haukeliseter site could lead to a solution that is closer to the truth and must be evaluated further.

On 21 and 23 December 2016 wind directions from the south-east and south were observed, respectively. As earlier discussed in Section 4.1.1 and 4.2.4 the wind change is associated with the occlusion passage on 23 December 2016 (Figure 3.6.2a and 3.6.2c). The wind direction on 21 December 2016 in Figure 4.1.1c change was also related to the large scale synoptic flow but is not associated to a frontal boundary. A comparison with the large scale weather analysis from ECMWF shows, that the large scale surface wind is from the south-west at 6 UTC on 21 December 2016 (not shown) and has changed to west at 12 UTC (Figure 3.6.1d). The observations at the Haukeliseter site show between 6 UTC and 12 UTC wind from south-east, while the predicted wind direction is from south in Figure 4.1.1c. The local wind direction influenced the precipitation pattern in the vertical on 21 and 23 December 2016, in the matter that a more consistent storm structure was

observed and predicted between 9 UTC to 12 UTC (Figures 4.2.11a to 4.2.11c).

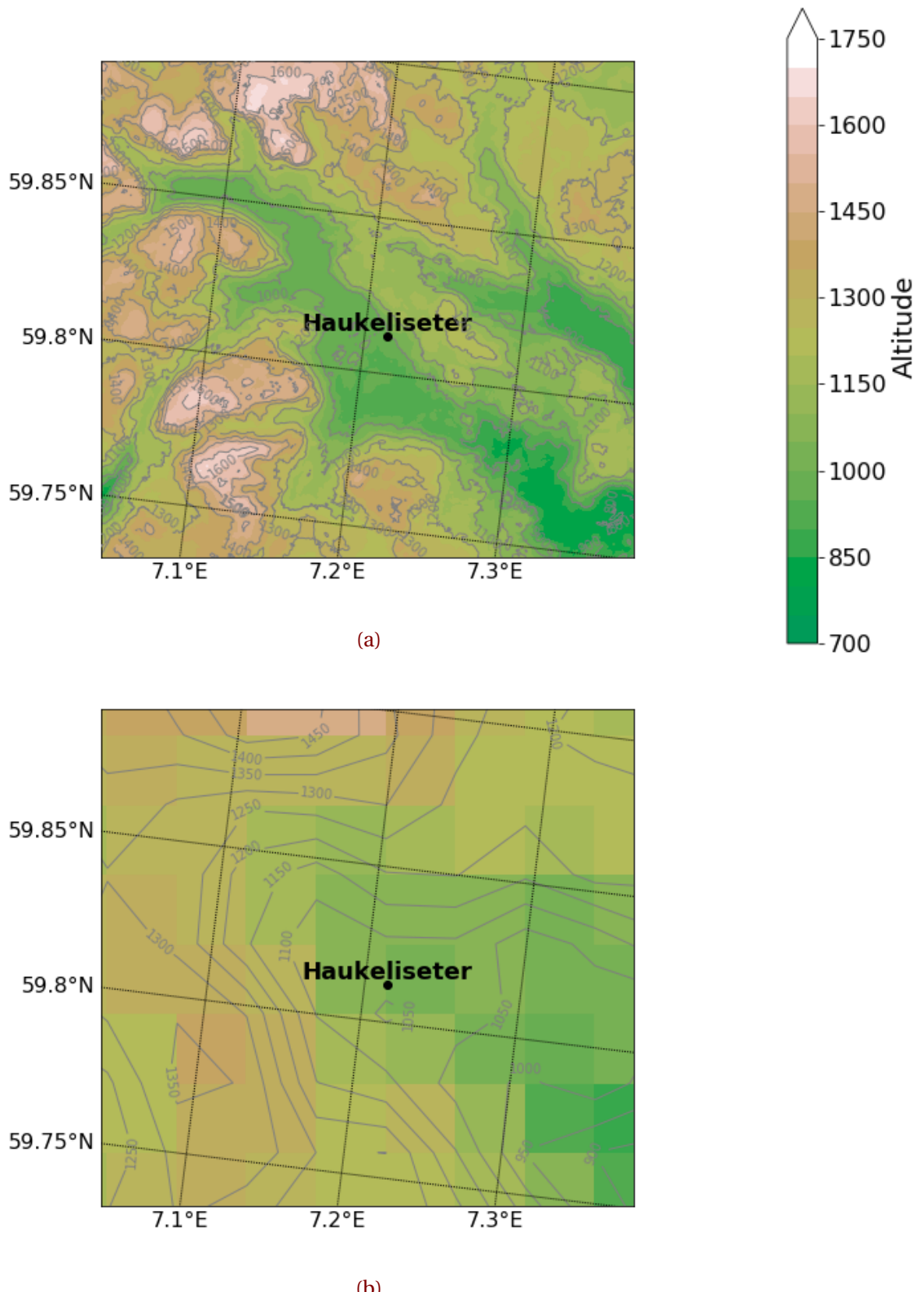


**Figure 4.2.10:** Topography around Haukeliseter. In **a** the DTM 10 Terrain Model (UTM33) from Geonorge [2018]. Contours and shading according to the colorbar. **b:** Representation of the topography around the measurement site Haukeliseter in MEPS. Contours and shading present the elevation of the grid cells.

Both days show a more consistent storm structure with not as intense snow water content than for storm patterns from the west such as on 24 December 2016 (Figures 4.2.7g to 4.2.7i). Figure 4.2.10a presents the local topography around Haukeliseter and Figure 4.2.10b shows the topography resolved by MEPS. MEPS is able to cover some of the complex structure around the site (Figure 4.2.10b), with the higher mountain to the west and the valley to the south-east (Figure 4.2.10a). The forecast model seems to forecast the wind direction overall well, only on 21 December 2016 before 10 UTC is a south-west instead of a south-east wind predicted. It displays that even if the large scale wind is from the south-west the local wind is rather from the south or south-east (Figure 3.6.1d).

Figure 4.1.2f shows a good correlation for west winds, but on the other side, southerly winds seem to be troublesome to predict for MEPS. Figure 4.1.2e indicates an unbalance for south-westerly winds. While south-easterly winds (along the valley) are observed at Haukeliseter predicts MEPS the 10 m wind to be south-westerly.

Figure 4.2.10 shows the comparison between the orography and the resolved topography by MEPS. Observed south-easterly winds are forced along the valley, directed in south-east. MEPS resolves it in the way, that the wind is south-westerly. Figure 4.2.10b displays a high mountain to the west of the station and a small one to the south. 10 m wind predicted by MEPS is predicted to blow between these two elevations.

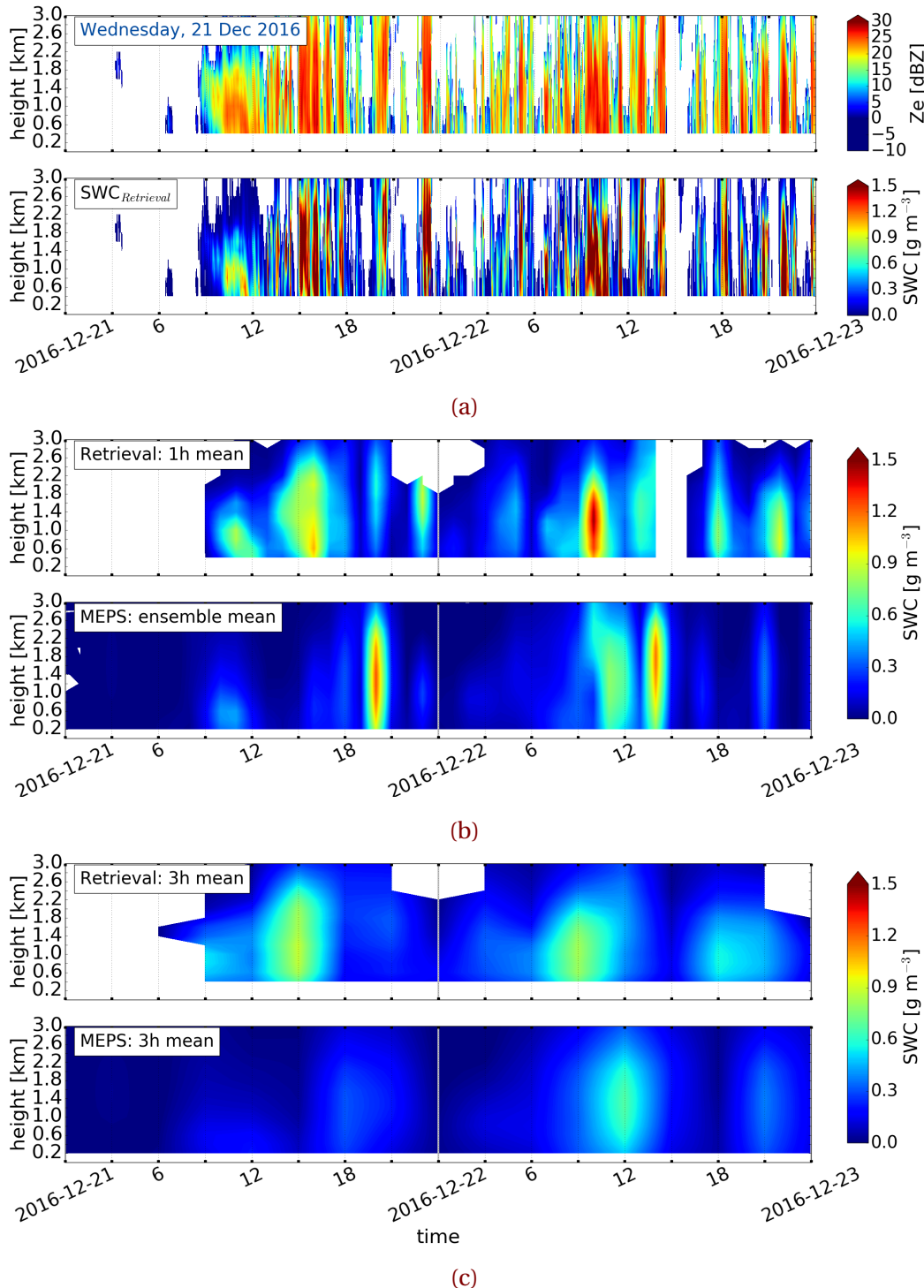


**Figure 4.2.11:** Initialisation 21 December 2016 0 UTC. (a,g) Upper panel: MRR reflectivity for 48 h, lower panel minutely retrieved SWC. (b, h) Upper panel: hourly averaged retrieved SWC, lower panel instantaneous hourly averaged forecast of all ensemble member SWC, neglecting missing values. (c, i) Upper panel three hourly averaged retrieved SWC, lower panel instantaneous three hourly averaged forecast of all ensemble member SWC.

As Figure 4.2.11b indicates is the model able to cover almost the exact timing of the up-slope storm pattern. The variability of each ensemble member is presented in Figure B.2.1a. It shows that almost all ensemble member agree on the occurrence of the storm pattern during 9 UTC to 12 UTC.

Wind from the west and therefore over high mountains (1500 m) always follow a pulsing with more intense vertical precipitation e.g. on 24 December 2016, Figure 4.2.7g and 4.2.7j). This effect might be related to wave breaking at the mountain and result into a pulsing precipitation pattern. More precipitation events need to be studied to understand this effect around the Haukeliseter site. MEPS does not cover all pulses related to west wind during the course of a day. This is related to the short occurrence of the pulses as well as to the time resolution of the forecast values. Since the prediction values exist only every hour the model might miss some of the high pulses 30 min before or after the frozen precipitation.

One outcome of the presented study is that MEPS is able to resolve the local topography and predicts the wind direction correctly. The variability between the ensemble members is smaller for precipitation related to south-easterly winds (Figure 4.2.9a, c, d). It did not cover the south-east wind direction on 21 December 2016 (Figure 4.1.1c), which must be related to the local topography.

It seems more intuitive for the model to force large scale south-westerly flow into south direction rather than the observed wind direction along the south-easterly directed valley. As seen in Figure 4.2.10 the wind must go along the 7.2° longitude, since a higher (1500 m to 1650 m) elevation is to the west and a 1350 m high mountain to the east. True prediction of wind direction leads to the correct estimation of frozen precipitation patterns, such as up-slope (south-easterly wind) and pulsing (west wind).

Section 4.2.3 describes the overestimation of surface snow accumulation during the intensification of the extreme storm. MEPS forecast in Figure 4.2.4d, e, and f show more ground accumulation than it is observed for 24 to 26 December 2016. One approach was to see, if the wind might have had an influence on the surface measurement of the double fence, which did not show to be true, even if 10 % under-catch by the double

fence gauge is assumed (Table 4.2.4). A comparison of the hourly values of MEPS, show neither on 24 nor on 25 nor 26 December 2016 high vertical snow amount compared to the estimated SWC (Figure 4.2.7h, 4.2.7k, and n). Figure B.2.1 shows values of very intense instantaneous snow water content for individual ensemble members, but no prominent sign of overestimation when the surface miscalculation was present.

During 24 to 26 December 2016 the wind was constantly from the west with higher wind speeds observed than during 21 to 23 December 2016 (Figure 4.1.1). Figure 4.1.2e and f indicate a better correlation for the forecasted and observed wind directions when precipitation overestimation occurred (24 to 26 December 2016). During 24 and 26 December 2016, observed wind speeds were higher up to  $18 \text{ ms}^{-1}$  than on the previous days. As Figure 4.1.2g and h present is the correlation between observation and forecasts lower for high wind speeds. The high wind speeds from the west followed a pulsing storm pattern with changing intense and less intense snowfall (e.g. 22 and 24 December 2016, Figures 4.2.7a to 4.2.7c, g, h, i). MEPS is able to forecast the pulsing pattern for initialisations longer than 24 h prior. Since the model estimates the wind direction correctly for west wind and local mountain affects it follows that there seems to be an interaction issue between frozen precipitation and the surface accumulation. Hourly vertical instantaneous values could have led to a misinterpretation of the here presented results. Furthermore, this study presents only a first look for a comparison between observed profiles of precipitation to MEPS forecast for an extreme event.

The ensemble variability in Figure 4.2.9 show that the ensemble members are divided about the existence of the exact precipitation pulsing.

While the wind direction of MEPS has a good agreement, at least for west wind, shows the wind speed larger values over all days (Figures 4.1.2e to 4.1.2h). Although MEPS includes ten perturbed ensemble members the insufficiency of AROME-MetCoOp too high wind prediction in extreme situations is not resolved. As Müller et al. [2017] mentioned are higher wind speeds in general better forecasted in AROME-MetCoOp than in ECMWF, which is an advantage for small scale forecast models. Especially in Norway, where the topography changes from sea to mountains.

## CHAPTER 5: SUMMARY AND OUTLOOK

In this thesis, a case study of an extreme event occurring on 21 to 26 December 2016 has been explored for snowfall. The extreme weather event 'Urd' affected large parts of Eastern, Southern, and Western Norway. During this period, the first low-pressure system developed east of Iceland, and the second cyclone evolved in the western Atlantic. Temperature changes related to the cold and warm fronts, and warm sectors followed observation of snow and liquid precipitation at Haukeliseter.

A sensitivity study of retrieved snow accumulation for different a-priori assumptions was carried out. Snowfall comparisons between double fence gauge observations and MEPS forecast of snowfall amount have been investigated at the WMO measurement site Haukeliseter. Meteorological parameters have been evaluated to see if large scale phenomena such as occlusion passages were observed and predicted by MEPS. Furthermore, a vertical comparison between retrieved profiles of snow water content is compared to 48 h forecasts of MEPS. Wind related topographical influence on precipitation and the resolution of MEPS were examined.

Double fence gauge measurements are considered as one of the best surface measurements for snowfall. Since additional instruments such as a MRR, MASC and PIP were installed at Haukeliseter during winter 2016/2017, a state of the art optimal estimation snowfall retrieval allowed to compare surface observations to vertically retrieved snowfall amounts. Assumptions of a particle model for rimed aggregates, climatological particle size distributions and fall speeds followed the best estimate for surface snowfall accumulation compared to the use of the CloudSat PSD estimate at Haukeliseter. The difference between retrieved snowfall amount and double fence was not larger than  $-5\%$  for 12 h and 24 h snowfall accumulation. The small difference between observation and estimated snowfall shows that it is important to choose a priori assumptions correctly to achieve

reasonable surface estimates precipitation amount at the surface.

AROME-MetCoOp was operational until November 2016 when it got substituted by the ensemble prediction weather forecast model at the Norwegian Meteorological Institute. The change from a deterministic forecast to a ensemble prediction system will help to take into account measurement uncertainties. Since MEPS has just become operational, an unique opportunity is given to do first comparisons between the WMO station Haukeliseter, the additional installed instruments, and the weather forecast model. The closest model grid point to the measurement site Haukeliseter was chosen to answer the research question if MEPS is able to predict large-scale phenomena such as occlusions related to an extreme event. It turns out that the regional forecast model MEPS is capable of predicting changes associated to frontal passages and occlusions. Pressure, temperature, and wind changes associated with passages of fronts were predicted 24 h and 48 h in advance. The correlation between surface observations at the site and the weather forecast model were best for sea level pressure prediction. The mean absolute error for 2 m temperature was never larger than 1 K, but a warm temperature bias occurred on 24 December 2016. **Include in results? Or double check** During the extreme Christmas storm in 2016, overestimations of wind and precipitation accumulation at the surface by MEPS were seen.

In the meteorological analysis an overestimation of surface precipitation accumulation up to 60 % shows during the intensification of the Christmas 2016 extreme event and hence in detail analysed. The average difference between precipitation amount at the surface decreases with increasing lead time for 21 to 26 December 2016. The 12 h precipitation accumulation had a mean absolute error up to 12 mm which is approximately eight times larger than the Norwegian mean of December 2014.

A comparison of the wind influenced under-catchment by the double fence of 10 % showed a small difference error. The surface accumulation was nevertheless overestimated by more than 40 %. Reasons for the prediction of too much precipitation accumulation at the ground could be initialisation errors as well as the use of one grid point instead of using a variable average of surrounding grid points. The results show that MEPS is not able to predict the precipitation correctly during the Christmas 2016 extreme event.

The vertical snowfall measurements can be trusted after it was shown that the retrieved estimated snowfall at the surface is in good agreement with those observed at the double fence gauge.

The one and three hourly ensemble means of MEPS displayed the ability to predict more consistent, up-slope storm patterns. For this type of storm the ensemble variability for initialisations 24 h and 48 h prior occurrence was low. MEPS ensemble members prediction were uncertain about the appearance of pulsing patterns related to westerlies. Greater variability between the ensemble members for pulsing storm patterns is probably related to the temporal resolution of MEPS ensemble forecast data and the short appearance of the pulses, of around 30 min.

In general, the estimated snow water content from MRR profiles is greater than the instantaneous average prediction of snowfall. The deterministic and first ensemble member (1 h resolution) predicted high snow water contents on some days during the 2016 Christmas storm.

On 25 December 2016, MASC images could verify the presence of liquid precipitation during the passage of a warm sector at Haukeliseter. MEPS was able to estimate the occurrence of liquid precipitation 24 h and 48 h in advance. Vertical comparison between reflectivity profiles and modelled liquid water content have shown the prediction of liquid precipitation, both in time and layer thickness. This is an important advantage of a regional weather forecast model, as the change from snowfall to liquid precipitation poses a great risk in Norwegian mountains.

Although MEPS has a horizontal resolution of 2.5km, the representation of the mountainous terrain in Norway might still be an issue. MEPS is able to resolve some of the major orographic patterns, such as high mountains to the west and the south-east of Haukeliseter. Westerlies and their associated pulsing precipitation pattern were correct predicted by MEPS. Forecasts for westerlies during 24 and 26 December 2016 showed a good correlation. In contrast, observed south-east winds were often predicted to be south-westerly wind (not along the mountain valley, SE) during 21 and 23 December 2016. Nevertheless is MEPS able to relate southerly winds with up-slope patterns of precipitation.

This study demonstrates the complex interaction of analysing snowfall extreme events with observations and regional model prediction. The here presented results are a first look for only one extreme storm at one station and further studies have to be done.

## 5.1 OUTLOOK

Only a few studies have addressed similar approaches like the comparison of vertical snowfall prediction to observations, and thus comparison with other work is difficult. Hence, the here presented results motivate to deal more with the subject of vertical snowfall observation and its comparison to regional weather forecast models.

First and foremost it is important to investigate more extreme snowfall events during winter at Haukeliseter. To see if the deviations between surface accumulation and estimated precipitation amount from vertical observations keep as small. Furthermore these results should be compared to different stations in Norway with similar polar tundra climate, to find out if a-priori assumptions can be generalised for the same local climate. More case studies will also help to get a better estimate about the performance of MEPS during extreme winter events. The mean absolute error for 12 h accumulation has shown a great variability, depending on the initialisation time and the intensification of the low-pressure system. This increase in mean absolute error with intensification might be low when compared to other cases.

The previous Chapters have indicated, the regional model MEPS is able to predict larger scale phenomena. This might be related to the outer boundary condition ECMWF or the Christmas 2016 extreme event was more predictable. In general, surface parameters such as wind pressure and temperature were predicted well, only wind speed and precipitation accumulation showed overestimation in MEPS predictions. Wind speed forecasts were higher than observations, this might be related to the representation of the orography in MEPS, or the general overestimation of wind speed already apparent in AROME-MetCoOp.

Sensitivity studies for the outer boundary could help to understand how much ECMWF forecast influence the MEPS prediction for local meteorological effects. ECMWF as boundary condition might not have reached its stabilised state when MEPS was initiated during the event, and could also have led to the overestimation of wind speed and surface accumulation. A comparison between ECMWF forecast and MEPS will verify if that might be the case. Re-analysis data can help to show the uncertainty in the initial and boundary conditions. A re-run with analysis data from ECMWF could possibly improve the original

forecast. It will be interesting to initiate MEPS with all available observations, to see if this has an influence on the overestimation of wind and precipitation accumulation.

Another approach could be to perturb the deterministic forecast in other way. Different perturbations might lead to a better correlation between observation and forecast at the ground. Furthermore, the choice of using the closest grid point to Haukeliseter might not have been the best approach. Using four close by grid points instead of only one could help to verify overestimations of MEPS forecasts compared to observations.

Even though MEPS performed well in the vertical by relating the wind to the storm structure correctly, it will be interesting to investigate the here presented results with a higher time resolution to resolve for the short pulses. Since MEPS overestimates the surface accumulation and the ensemble means show to be in general smaller than the estimated snow water content, the afore mentioned solution help to investigate the overestimation of snowfall at the surface and the relationship between the vertical forecast and surface prediction model.

The local affect of pulsing patterns related to westerlies should be examined. To understand if e.g. wave breaking occurs at the mountain to the west, or if it is an effect of local surface fronts.

It is important to have correct measurements such as the double fence gauge or the MRR-PSD retrieval approach. Correct measurements will help to improve initial conditions for weather forecast models, so that initialisations can start at the true state. Furthermore accurate observations will help to get a greater understanding of vertical snowfall structure. Investigating in more detail microphysical processes within mesoscale storms with vertical measurements of snowfall for extreme events can be a grand improvement for weather and climate prediction.

## REFERENCES

- Barnett, T. P., Adam, J. C., and Lettenmaier, D. P. Potential impacts of a warming climate on water availability in snow-dominated regions. *Nature*, 438(7066):303–309, November 2005. ISSN 1476-4687. doi: [10.1038/nature04141](https://doi.org/10.1038/nature04141). URL <https://www.nature.com/articles/nature04141>.
- Caniaux, G., Redelsperger, J.-L., and Lafore, J.-P. A Numerical Study of the Stratiform Region of a Fast-Moving Squall Line. Part I: General Description and Water and Heat Budgets. *J. Atmos. Sci.*, 51(14):2046–2074, July 1994. ISSN 0022-4928. doi: [10.1175/1520-0469\(1994\)051<2046:ANSOTS>2.0.CO;2](https://doi.org/10.1175/1520-0469(1994)051<2046:ANSOTS>2.0.CO;2). URL [https://journals.ametsoc.org/doi/abs/10.1175/1520-0469\(1994\)051%3C2046:ANSOTS%3E2.0.CO;2](https://journals.ametsoc.org/doi/abs/10.1175/1520-0469(1994)051%3C2046:ANSOTS%3E2.0.CO;2).
- Christensen, M. W., Behrangi, A., L'ecuyer, T. S., Wood, N. B., Lebsack, M. D., and Stephens, G. L. Arctic Observation and Reanalysis Integrated System: A New Data Product for Validation and Climate Study. *Bull. Amer. Meteor. Soc.*, 97(6):907–916, January 2016. ISSN 0003-0007. doi: [10.1175/BAMS-D-14-00273.1](https://doi.org/10.1175/BAMS-D-14-00273.1). URL <https://journals.ametsoc.org/doi/10.1175/BAMS-D-14-00273.1>.
- Colle, B. A., Garvert, M. F., Wolfe, J. B., Mass, C. F., and Woods, C. P. The 13–14 December 2001 IMPROVE-2 Event. Part III: Simulated Microphysical Budgets and Sensitivity Studies. *J. Atmos. Sci.*, 62(10):3535–3558, October 2005. ISSN 0022-4928. doi: [10.1175/JAS3552.1](https://doi.org/10.1175/JAS3552.1). URL <https://journals.ametsoc.org/doi/abs/10.1175/JAS3552.1>.
- Cooper, S. J., Wood, N. B., and L'Eucyer, T. S. A variational technique to estimate snowfall rate from coincident radar, snowflake, and fall-speed observations. *Atmos. Meas. Tech.*, 10(7):2557–2571, July 2017. ISSN 1867-8548. doi: [10.5194/amt-10-2557-2017](https://doi.org/10.5194/amt-10-2557-2017). URL <https://www.atmos-meas-tech.net/10/2557/2017/>.

- Dahlgren, P. A Comparison Of Two Large Scale Blending Methods. page 16, 2013. URL <http://metcoop.org/memo/2013/02-2013-METCOOP-MEMO.PDF>.
- Dando, P. Introducing the octahedral reduced Gaussian grid, June 2016. URL <https://software.ecmwf.int/wiki/display/FCST/Gaussian+grids>.
- Doviak, R. J. and Zrnic, D. S. *Doppler Radar and Weather Observations*. Courier Corporation, 1993. ISBN 978-0-486-45060-5. Google-Books-ID: ispLkPX9n2UC.
- eklima. Norwegian Meteorological Institute, 2016. URL [http://sharki.oslo.dnmi.no/portal/page?\\_pageid=73,39035,73\\_39049&\\_dad=portal&\\_schema=PORTAL](http://sharki.oslo.dnmi.no/portal/page?_pageid=73,39035,73_39049&_dad=portal&_schema=PORTAL).
- Farestveit, E. 80.000 mista radioen under ekstremvêret, December 2016. URL <https://www.nrk.no/hordaland/80.000-mista-radioen-under-ekstremveret-1.13294980>.
- Field, C. B., Barros, V. R., Dokken, D. J., Mach, K. J., Mastrandrea, M. D., Bilir, T. E., Chatterjee, M., Ebi, K. L., Estrada, Y. O., Genova, R. C., Girma, B., Kissel, E. S., Levy, A. N., MacCracken, S., Mastrandrea, P. R., and White, L. L. Summary for policymakers. In: Climate Change 2014: Impacts, Adaptation, and Vulnerability. Part A: Global and Sectoral Aspects. Contribution of Working Group II to the Fifth Assessment Report of the Intergovernmental Panel on Climate Change. Cambridge: Cambridge University Press, page 34, 2014.
- Færaas, A., Rommetveit, A., Duesund, J., and Senel, E. «Urd» har nådd orkan styrke – flytter seg mot Østlandet, December 2016. URL [http://www.yr.no/artikkel/\\_urd\\_-har-nadd-orkan-styrke--flytter-seg-mot-ostlandet-1.13292245](http://www.yr.no/artikkel/_urd_-har-nadd-orkan-styrke--flytter-seg-mot-ostlandet-1.13292245).
- Garrett, T. J., Fallgatter, C., Shkurko, K., and Howlett, D. Fall speed measurement and high-resolution multi-angle photography of hydrometeors in free fall. *Atmos. Meas. Tech.*, 5(11):2625–2633, November 2012. ISSN 1867-8548. doi: [10.5194/amt-5-2625-2012](https://doi.org/10.5194/amt-5-2625-2012). URL <https://www.atmos-meas-tech.net/5/2625/2012/>.
- Garvert, M. F., Woods, C. P., Colle, B. A., Mass, C. F., Hobbs, P. V., Stoelinga, M. T., and Wolfe, J. B. The 13–14 December 2001 IMPROVE-2 Event. Part II: Comparisons of MM5 Model Simulations of Clouds and Precipitation with Observations. *J. Atmos.*

- Sci.*, 62(10):3520–3534, October 2005. ISSN 0022-4928. doi: 10.1175/JAS3551.1. URL <https://journals.ametsoc.org/doi/10.1175/JAS3551.1>.
- Geonor Inc. T-200b All Weather Precipitation – Rain Gauge, 2015. URL <http://geonor.com/live/products/weather-instruments/t-200b-weather-precipitation-rain-gauge/>.
- Geonorge. DTM 10 Terrengmodell (UTM33) - Kartverket - Kartkatalogen, May 2018. URL <https://kartkatalog.geonorge.no/metadata/uuid/dddbb667-1303-4ac5-8640-7ec04c0e3918>.
- Goodison, B. E., Louie, P. Y. T., and Yang, D. WMO Solid Precipitation Measurement Intercomparison: Final Report. Instruments and Observing Methods Rep. 67, WMO/TD-No. 872,. *World Meteorological Organization, Geneva, Switzerland*, page 318, 1998.
- Gowan, T. M., Steenburgh, W. J., and Schwartz, C. S. Validation of Mountain Precipitation Forecasts from the Convection-Permitting NCAR Ensemble and Operational Forecast Systems over the Western United States. *Wea. Forecasting*, 33(3):739–765, June 2018. ISSN 0882-8156, 1520-0434. doi: 10.1175/WAF-D-17-0144.1. URL <http://journals.ametsoc.org/doi/10.1175/WAF-D-17-0144.1>.
- Hansen, B. B., Isaksen, K., Benestad, R. E., Kohler, J., Pedersen, Ø. Ø., Loe, L. E., Coulson, S. J., Larsen, J. O., and Varpe, Ø. Warmer and wetter winters: characteristics and implications of an extreme weather event in the High Arctic. *Environ. Res. Lett.*, 9(11):114021, 2014. ISSN 1748-9326. doi: 10.1088/1748-9326/9/11/114021. URL <http://stacks.iop.org/1748-9326/9/i=11/a=114021>.
- Hansen, B. B., Aanes, R., Herfindal, I., Kohler, J., and Sæther, B.-E. Climate, icing, and wild arctic reindeer: past relationships and future prospects. *Ecology*, 92(10):1917–1923, October 2011. ISSN 1939-9170. doi: 10.1890/11-0095.1. URL <https://esajournals.onlinelibrary.wiley.com/doi/abs/10.1890/11-0095.1>.
- Homleid, M. and Tveter, F. T. Verification of operational weather prediction models september to november 2015. *METInfo Rep*, 16:2016, 2016. URL [https://www.met.no/publikasjoner/met-info/met-info-2016/\\_attachment/download/b0463915-](https://www.met.no/publikasjoner/met-info/met-info-2016/_attachment/download/b0463915-)

- cba0-42ac-8539-4233ae2bf01c:3d71565a27f88085373199a33ab8569151c144e9/  
MET-info-22-2016.pdf.
- Hudak, D., Barker, H., Rodriguez, P., and Donovan, D. The Canadian CloudSat Validation Project. *4th ERAD*, September 2006. URL <http://www.crahi.upc.edu/ERAD2006/proceedingsMask/00165.pdf>. Barcelona, Spain.
- Joos, H. and Wernli, H. Influence of microphysical processes on the potential vorticity development in a warm conveyor belt: a case-study with the limited-area model COSMO. *Q. J. Royal Meteorol. Soc.*, 138(663):407–418, January 2012. ISSN 00359009. doi: [10.1002/qj.934](https://doi.org/10.1002/qj.934). URL <http://doi.wiley.com/10.1002/qj.934>.
- Kalnay, E. *Atmospheric modeling, data assimilation and predictability*. Cambridge University Press, Cambridge, 2003. ISBN 978-0-521-79179-3.
- Kochendorfer, J., Nitu, R., Wolff, M., Mekis, E., Rasmussen, R., Baker, B., Earle, M. E., Reverdin, A., Wong, K., Smith, C. D., Yang, D., Roulet, Y.-A., Buisan, S., Laine, T., Lee, G., Aceituno, J. L. C., Alastraú, J., Isaksen, K., Meyers, T., Brækkan, R., Landolt, S., Jachcik, A., and Poikonen, A. Analysis of single-Alter-shielded and unshielded measurements of mixed and solid precipitation from WMO-SPICE. *Hydrol. Earth Syst. Sci.*, 21(7):3525–3542, July 2017. ISSN 1607-7938. doi: [10.5194/hess-21-3525-2017](https://doi.org/10.5194/hess-21-3525-2017). URL <https://www.hydrol-earth-syst-sci.net/21/3525/2017/>.
- Kulie, M. S. and Bennartz, R. Utilizing Spaceborne Radars to Retrieve Dry Snowfall. *J. Appl. Meteor. Climatol.*, 48(12):2564–2580, January 2009. ISSN 1558-8424. doi: [10.1175/2009JAMC2193.1](https://doi.org/10.1175/2009JAMC2193.1). URL <http://journals.ametsoc.org/doi/abs/10.1175/2009JAMC2193.1>.
- Kulie, M. S., Milani, L., Wood, N. B., Tushaus, S. A., Bennartz, R., and L’Ecuyer, T. S. A Shallow Cumuliform Snowfall Census Using Spaceborne Radar. *J. Hydrometeor.*, 17(4):1261–1279, February 2016. ISSN 1525-755X. doi: [10.1175/JHM-D-15-0123.1](https://doi.org/10.1175/JHM-D-15-0123.1). URL <https://journals.ametsoc.org/doi/abs/10.1175/JHM-D-15-0123.1>.
- Køltzow, M. A. MetCoOp EPS - A convection permitting ensemble prediction system, October 2017.

- L'Ecuyer, T. S. AOS 441 - Satellite and Radar Meteorology. January 2017. URL <https://lecuyer.aos.wisc.edu/aos441>.
- Liu G. Deriving snow cloud characteristics from CloudSat observations. *J. Geophys. Res. Atmos.*, 113(D8), September 2008. ISSN 0148-0227. doi: [10.1029/2007JD009766](https://doi.org/10.1029/2007JD009766). URL <https://agupubs.onlinelibrary.wiley.com/doi/abs/10.1029/2007JD009766>.
- Lorenz, E. N. Atmospheric Predictability as Revealed by Naturally Occurring Analogues. *J. Atmos. Sci.*, 26(4):636–646, July 1969. ISSN 0022-4928. doi: [10.1175/1520-0469\(1969\)26<636:APARBN>2.0.CO;2](https://doi.org/10.1175/1520-0469(1969)26<636:APARBN>2.0.CO;2). URL <https://journals.ametsoc.org/doi/abs/10.1175/1520-0469%281969%2926%3C636%3AAPARBN%3E2.0.CO%3B2>.
- Markowski, P. and Richardson, Y. *Mesoscale Meteorology in Midlatitudes*. John Wiley & Sons, September 2011. ISBN 978-1-119-96667-8. Google-Books-ID: MDeYosfLLEYC.
- Martin, J. E. *Mid-Latitude Atmospheric Dynamics: A First Course*. Wiley, May 2006. ISBN 978-0-470-86466-1.
- Matrosov, S. Y. Modeling Backscatter Properties of Snowfall at Millimeter Wavelengths. *J. Atmos. Sci.*, 64(5):1727–1736, May 2007. ISSN 0022-4928. doi: [10.1175/JAS3904.1](https://doi.org/10.1175/JAS3904.1). URL <https://journals.ametsoc.org/doi/abs/10.1175/JAS3904.1>.
- McCumber, M., Tao, W.-K., Simpson, J., Penc, R., and Soong, S.-T. Comparison of Ice-Phase Microphysical Parameterization Schemes Using Numerical Simulations of Tropical Convection. *J. Appl. Meteor.*, 30(7):985–1004, July 1991. ISSN 0894-8763. doi: [10.1175/1520-0450-30.7.985](https://doi.org/10.1175/1520-0450-30.7.985). URL <https://journals.ametsoc.org/doi/abs/10.1175/1520-0450-30.7.985>.
- Meehl, G. A., Karl, T., Easterling, D. R., Changnon, S., Pielke, R., Changnon, D., Evans, J., Groisman, P. Y., Knutson, T. R., Kunkel, K. E., Mearns, L. O., Parmesan, C., Pulwarty, R., Root, T., Sylves, R. T., Whetton, P., and Zwiers, F. An Introduction to Trends in Extreme Weather and Climate Events: Observations, Socioeconomic Impacts, Terrestrial Ecological Impacts, and Model Projections. *Bull. Amer. Meteor. Soc.*, 81(3):413–416, March 2000. ISSN 0003-0007. doi: [10.1175/1520-0477\(2000\)081<0413:AITTIE>2.3.CO;2](https://doi.org/10.1175/1520-0477(2000)081<0413:AITTIE>2.3.CO;2). URL [https://journals.ametsoc.org/doi/abs/10.1175/1520-0477\(2000\)081%3C0413:AITTIE%3E2.3.CO;2](https://journals.ametsoc.org/doi/abs/10.1175/1520-0477(2000)081%3C0413:AITTIE%3E2.3.CO;2).

- MetCoOp Wiki. Description of MEPS, December 2017. URL <https://metcoop.smhi.se/dokuwiki/nwp/metcoop/>.
- METEK, M. M. G. Micro Rain Radar MRR-2, October 2010. URL <http://metek.de/wp-content/uploads/2014/05/Metek-Micro-Rain-Radar-MRR-2-Datasheet.pdf>.
- Meteo France. The Meso-NH Atmospheric Simulation System: Scientific Documentation, Part III: Physics, January 2009.
- Meteorologene. "Her kommer #Urd! Selve Lavtrykksenteret treffer Møre og Romsdal, men den sterkeste vinden kommer sør for Stad. #SørNorge" 26 December 2016, 9:34am, 2016. URL <https://twitter.com/Meteorologene>.
- Müller, M., Homleid, M., Ivarsson, K.-I., Køltzow, M. A. Ø., Lindskog, M., Midtbø, K. H., Andrae, U., Aspelien, T., Berggren, L., Bjørge, D., Dahlgren, P., Kristiansen, J., Randriamampianina, R., Ridal, M., and Vignes, O. AROME-MetCoOp: A Nordic Convective-Scale Operational Weather Prediction Model. *Wea. Forecasting*, 32(2):609–627, January 2017. ISSN 0882-8156. doi: [10.1175/WAF-D-16-0099.1](https://doi.org/10.1175/WAF-D-16-0099.1). URL <http://journals.ametsoc.org/doi/abs/10.1175/WAF-D-16-0099.1>.
- Newman, A. J., Kucera, P. A., and Bliven, L. F. Presenting the Snowflake Video Imager (SVI). *J. Atmos. Oceanic Technol.*, 26(2):167–179, February 2009. ISSN 0739-0572. doi: [10.1175/2008JTECHA1148.1](https://doi.org/10.1175/2008JTECHA1148.1). URL <https://journals.ametsoc.org/doi/abs/10.1175/2008JTECHA1148.1>.
- Noh, Y.-J., Liu, G., Seo, E.-K., Wang, J. R., and Aonashi, K. Development of a snowfall retrieval algorithm at high microwave frequencies. *J. Geophys. Res.*, 111(D22), November 2006. ISSN 2156-2202. doi: [10.1029/2005JD006826](https://doi.org/10.1029/2005JD006826). URL <https://agupubs.onlinelibrary.wiley.com/doi/abs/10.1029/2005JD006826>.
- Norin, L., Devasthale, A., L'Ecuyer, T. S., Wood, N. B., and Smalley, M. Intercomparison of snowfall estimates derived from the CloudSat Cloud Profiling Radar and the ground-based weather radar network over Sweden. *Atmos. Meas. Tech.*, 8(12):5009–5021, December 2015. ISSN 1867-8548. doi: [10.5194/amt-8-5009-2015](https://doi.org/10.5194/amt-8-5009-2015). URL <https://www.atmos-meas-tech.net/8/5009/2015/>.

- Norwegian Meteorological Institute. MET Norway Thredds Service, 2016. URL <http://thredds.met.no/thredds/catalog/meps25epsarchive/catalog.html>.
- Olsen, A.-M. and Granerød, M. Ekstremværrapport. Hendelse: Urd 26. desember met. info. no. 18/2017 ISSN X METEOROLOGI Bergen, - PDF, September 2017. URL <http://docplayer.me/48734203-Ekstremvaerrapport-hendelse-urd-26-desember-met-info-no-18-2017-issn-x-meteorologi-bergen.html>.
- Palerme, C., Kay, J. E., Genthon, C., L'Ecuyer, T., Wood, N. B., and Claud, C. How much snow falls on the Antarctic ice sheet? *The Cryosphere*, 8(4):1577–1587, August 2014. ISSN 1994-0424. doi: 10.5194/tc-8-1577-2014. URL <https://www.the-cryosphere.net/8/1577/2014/>.
- Palerme, C., Genthon, C., Claud, C., Kay, J. E., Wood, N. B., and L'Ecuyer, T. Evaluation of current and projected Antarctic precipitation in CMIP5 models. *Clim. Dyn.*, 48(1-2): 225–239, January 2017. ISSN 0930-7575, 1432-0894. doi: 10.1007/s00382-016-3071-1. URL <https://link.springer.com/article/10.1007/s00382-016-3071-1>.
- Pedersen, K. and Rommetveit, A. Hva er et «ekstremvær»?, November 2013. URL [http://www.yr.no/artikkelen/hva-er-et-\\_ekstremvaer\\_\\_\\_-1.7890946](http://www.yr.no/artikkelen/hva-er-et-_ekstremvaer___-1.7890946).
- Peel, M. C., Finlayson, B. L., and McMahon, T. A. Updated world map of the Köppen-Geiger climate classification. *Hydrology and Earth System Sciences Discussions*, 4(2):439–473, March 2007. URL <https://hal.archives-ouvertes.fr/hal-00298818>.
- Pinty, J.-P. and Jabouille, P. A mixed-phased cloud parameterization for use in a mesoscale non-hydrostatic model: Simulations of a squall line and of orographic precipitation. pages 217–220. Amer. Meteor. Soc., 1998.
- Putkonen, J. and Roe, G. Rain-on-snow events impact soil temperatures and affect ungulate survival: RAIN-ON-SNOW EVENTS IMPACT SOIL TEMPERATURES. *Geophysical Research Letters*, 30(4), February 2003. ISSN 00948276. doi: 10.1029/2002GL016326. URL <http://doi.wiley.com/10.1029/2002GL016326>.
- Rinehart, R. E. *Radar for Meteorologists: Or You, Too, Can be a Radar Meteorologist*. Rinehart Publications, 2010. ISBN 978-0-9658002-3-5. Google-Books-ID: VqatcQAACAAJ.

- Rutz, J. J., Steenburgh, W. J., and Ralph, F. M. Climatological Characteristics of Atmospheric Rivers and Their Inland Penetration over the Western United States. *Mon. Wea. Rev.*, 142(2):905–921, January 2014. ISSN 0027-0644. doi: [10.1175/MWR-D-13-00168.1](https://doi.org/10.1175/MWR-D-13-00168.1). URL <http://journals.ametsoc.org/doi/abs/10.1175/MWR-D-13-00168.1>.
- Ruud, S., Carr Ekroll, H., Bakke Foss, A., Torgersen, H. O., and Annar Holm, P. To tonn tungt skilt blåste ned da ekstremværet traff Oslo og Østlandet i natt, December 2016. URL <https://www.aftenposten.no/article/ap-2z6wy.html>.
- Schirle, C. Characterization of snowfall at high latitudes using an optimal estimation-based retrieval algorithm. Private Communication, 2018.
- Schwartz, C. S. Reproducing the September 2013 Record-Breaking Rainfall over the Colorado Front Range with High-Resolution WRF Forecasts. *Wea. Forecasting*, 29(2): 393–402, January 2014. ISSN 0882-8156. doi: [10.1175/WAF-D-13-00136.1](https://doi.org/10.1175/WAF-D-13-00136.1). URL [https://journals.ametsoc.org/doi/abs/10.1175/WAF-D-13-00136.1](http://journals.ametsoc.org/doi/abs/10.1175/WAF-D-13-00136.1).
- Skofronick-Jackson, G. M., Kim, M.-J., Weinman, J. A., and Chang, D.-E. A physical model to determine snowfall over land by microwave radiometry. *IEEE Geosci. Remote Sens. Lett.*, 42(5):1047–1058, May 2004. ISSN 0196-2892. doi: [10.1109/TGRS.2004.825585](https://doi.org/10.1109/TGRS.2004.825585).
- Stephens, G. L. *Remote Sensing of the Lower Atmosphere: An Introduction*. Oxford University Press, 1994. ISBN 978-0-19-508188-6. Google-Books-ID: [2FcRAQAAIAAJ](#).
- Stimberis, J. and Rubin, C. M. Glide avalanche response to an extreme rain-on-snow event, Snoqualmie Pass, Washington, USA. *Journal of Glaciology*, 57(203): 468–474, 2011. ISSN 0022-1430, 1727-5652. doi: [10.3189/002214311796905686](https://doi.org/10.3189/002214311796905686). URL <https://www.cambridge.org/core/journals/journal-of-glaciology/article/glide-avalanche-response-to-an-extreme-rainonsnow-event-snoqualmie-pass-washington-usa/2B6E48BD92F0700B7BEA02EF156E203F>.
- Stocker, T. F., Qin, D., Plattner, G.-K., Tignor, M. M. B., Allen, S. K., Boschung, J., Nauels, A., Xia, Y., Bex, V., and Midgley, P. M. Working Group I Contribution to the Fifth Assessment Report of the Intergovernmental Panel on Climate Change. *Cambridge: Cambridge University Press*, page 14, 2013.

- Sun, J. Convective-scale assimilation of radar data: progress and challenges. *Quarterly Journal of the Royal Meteorological Society*, 131(613):3439–3463, 2005. ISSN 1477-870X. doi: 10.1256/qj.05.149. URL <https://rmets.onlinelibrary.wiley.com/doi/abs/10.1256/qj.05.149>.
- Wolff, M. A. WMO Solid Precipitation Intercomparison Experiment (WMO-SPICE), Ch. 4.2.4 Precipitation measurements in areas with high winds and/or complex terrain. unpublished, 2018.
- Wolff, M. A., Brækkan, R., Isaksen, K., and Ruud, E. A new testsite for wind correction of precipitation measurements at a mountain plateau in southern Norway. In *Proceedings of WMO Technical Conference on Meteorological and Environmental Instruments and Methods of Observation (TECO–2010). Instruments and Observing Methods Report*, 2010.
- Wolff, M. A., Isaksen, K., Brækkan, R., Alfnes, E., Petersen-Øverleir, A., and Ruud, E. Measurements of wind-induced loss of solid precipitation: description of a Norwegian field study. *Hydrol. Res.*, 44(1):35–43, February 2013. ISSN 0029-1277, 2224-7955. doi: 10.2166/nh.2012.166. URL <http://hr.iwaponline.com/content/44/1/35>.
- Wolff, M. A., Isaksen, K., Petersen-Øverleir, A., Ødemark, K., Reitan, T., and Brækkan, R. Derivation of a new continuous adjustment function for correcting wind-induced loss of solid precipitation: results of a Norwegian field study. *Hydrol. Earth Syst. Sci.*, 19(2):951–967, February 2015. ISSN 1607-7938. doi: 10.5194/hess-19-951-2015. URL <https://www.hydrol-earth-syst-sci.net/19/951/2015/>.
- Wood, N. B. *Estimation of snow microphysical properties with application to millimeter-wavelength radar retrievals for snowfall rate*. Ph.D., Colorado State University, 2011. URL [https://dspace.library.colostate.edu/bitstream/handle/10217/48170/Wood\\_colostate\\_0053A\\_10476.pdf?sequence=1&isAllowed=y](https://dspace.library.colostate.edu/bitstream/handle/10217/48170/Wood_colostate_0053A_10476.pdf?sequence=1&isAllowed=y).
- Wood, N. B., L'Ecuyer, T. S., Vane, D. G., Stephens, G. L., and Partain, P. Level 2c snow profile process description and interface control document. Technical Report, 2013. URL [http://www.cloudsat.cira.colostate.edu/sites/default/files/products/files/2C-SNOW-PROFILE\\_PDICD.P\\_R04.20130210.pdf](http://www.cloudsat.cira.colostate.edu/sites/default/files/products/files/2C-SNOW-PROFILE_PDICD.P_R04.20130210.pdf).

- Wood, N. B., L'Ecuyer, T. S., Heymsfield, A. J., and Stephens, G. L. Microphysical Constraints on Millimeter-Wavelength Scattering Properties of Snow Particles. *J. Appl. Meteor. Climatol.*, 54(4):909–931, January 2015. ISSN 1558-8424. doi: 10.1175/JAMC-D-14-0137.1. URL <http://journals.ametsoc.org/doi/10.1175/JAMC-D-14-0137.1>.



# APPENDIX A: FORWARD MODEL

## A.1 SCATTERING MODEL

**Table A.1.1:** Branched 6-arm spatial particle with porosities, 2D, mass oriented scattering scheme at 24.0GHz.  $\mathbf{r}$ , particle size of the snow particle;  $\mathbf{m}(\mathbf{r})$ , particle mass;  $\sigma_{\text{bk}}(\mathbf{r})$  and  $\sigma_{\text{ext}}(\mathbf{r})$ , backscattering and extinction cross-section, respectively.

$\mathbf{r}$ [ $\mu\text{m}$ ]	$\mathbf{m}(\mathbf{r})$ [kg]	$\sigma_{\text{bk}}(\mathbf{r})$ [ $\text{m}^{-2}$ ]	$\sigma_{\text{ext}}(\mathbf{r})$ [ $\text{m}^{-2}$ ]
35.27	$1.68529 \times 10^{-10}$	$8.85111 \times 10^{-17}$	$4.85381 \times 10^{-17}$
41.73	$2.79128 \times 10^{-10}$	$2.00612 \times 10^{-16}$	$1.28776 \times 10^{-16}$
47.87	$4.21355 \times 10^{-10}$	$4.792 \times 10^{-16}$	$2.9959 \times 10^{-16}$
53.76	$5.96809 \times 10^{-10}$	$1.02733 \times 10^{-15}$	$6.08871 \times 10^{-16}$
59.45	$8.07074 \times 10^{-10}$	$1.68272 \times 10^{-15}$	$1.09633 \times 10^{-15}$
70.34	$1.3368 \times 10^{-9}$	$5.7444 \times 10^{-15}$	$3.61096 \times 10^{-15}$
80.69	$2.01798 \times 10^{-9}$	$1.0899 \times 10^{-14}$	$6.93961 \times 10^{-15}$
90.63	$2.85939 \times 10^{-9}$	$2.244 \times 10^{-14}$	$1.42249 \times 10^{-14}$
100.20	$3.86421 \times 10^{-9}$	$3.7814 \times 10^{-14}$	$2.73019 \times 10^{-14}$
109.50	$5.04313 \times 10^{-9}$	$7.05869 \times 10^{-14}$	$5.36211 \times 10^{-14}$
118.60	$6.40785 \times 10^{-9}$	$1.16874 \times 10^{-13}$	$9.74644 \times 10^{-14}$
127.40	$7.94266 \times 10^{-9}$	$1.67227 \times 10^{-13}$	$1.56602 \times 10^{-13}$
144.50	$1.15894 \times 10^{-8}$	$3.41952 \times 10^{-13}$	$4.19048 \times 10^{-13}$
160.90	$1.60002 \times 10^{-8}$	$7.30397 \times 10^{-13}$	$1.05187 \times 10^{-12}$

*Continued on next page*

Table A.1.1 Continued from previous page

<b>r</b> [μm]	<b>m(r)</b> [kg]	$\sigma_{\text{bk}}(\mathbf{r})$ [m <sup>-2</sup> ]	$\sigma_{\text{ext}}(\mathbf{r})$ [m <sup>-2</sup> ]
176.80	$2.122\,78 \times 10^{-8}$	$1.136\,38 \times 10^{-12}$	$2.003\,59 \times 10^{-12}$
192.30	$2.731\,47 \times 10^{-8}$	$2.053\,33 \times 10^{-12}$	$3.635\,31 \times 10^{-12}$
236.50	$5.081\,03 \times 10^{-8}$	$5.941\,38 \times 10^{-12}$	$1.525\,6 \times 10^{-11}$
278.10	$8.261\,54 \times 10^{-8}$	$1.577\,15 \times 10^{-11}$	$4.319\,27 \times 10^{-11}$
317.70	$1.231\,71 \times 10^{-7}$	$3.687\,19 \times 10^{-11}$	$9.719\,16 \times 10^{-11}$
355.80	$1.730\,12 \times 10^{-7}$	$6.460\,05 \times 10^{-11}$	$1.890\,57 \times 10^{-10}$
392.60	$2.324\,39 \times 10^{-7}$	$1.291\,91 \times 10^{-10}$	$3.524\,6 \times 10^{-10}$
428.20	$3.015\,77 \times 10^{-7}$	$1.752\,6 \times 10^{-10}$	$5.673\,93 \times 10^{-10}$
463.00	$3.812\,42 \times 10^{-7}$	$3.581\,77 \times 10^{-10}$	$8.763\,74 \times 10^{-10}$
496.90	$4.712\,65 \times 10^{-7}$	$5.862\,79 \times 10^{-10}$	$1.304\,17 \times 10^{-9}$
530.10	$5.721\,78 \times 10^{-7}$	$8.501\,41 \times 10^{-10}$	$1.886\,2 \times 10^{-9}$
562.60	$6.840\,02 \times 10^{-7}$	$1.045\,66 \times 10^{-9}$	$2.608\,54 \times 10^{-9}$
594.50	$8.070\,74 \times 10^{-7}$	$1.545\,14 \times 10^{-9}$	$3.681\,76 \times 10^{-9}$
625.80	$9.413\,79 \times 10^{-7}$	$1.617\,04 \times 10^{-9}$	$4.485\,78 \times 10^{-9}$
656.60	$1.087\,33 \times 10^{-6}$	$2.107\,09 \times 10^{-9}$	$5.711\,84 \times 10^{-9}$
687.00	$1.245\,46 \times 10^{-6}$	$3.315\,67 \times 10^{-9}$	$7.859\,38 \times 10^{-9}$
717.00	$1.415\,84 \times 10^{-6}$	$3.735\,98 \times 10^{-9}$	$9.508\,17 \times 10^{-9}$
746.50	$1.597\,89 \times 10^{-6}$	$4.405\,91 \times 10^{-9}$	$1.148\,24 \times 10^{-8}$
775.60	$1.792\,14 \times 10^{-6}$	$5.143\,2 \times 10^{-9}$	$1.373\,71 \times 10^{-8}$
804.40	$1.999\,28 \times 10^{-6}$	$4.212\,61 \times 10^{-9}$	$1.596\,03 \times 10^{-8}$
832.90	$2.219\,4 \times 10^{-6}$	$7.087\,5 \times 10^{-9}$	$1.904\,38 \times 10^{-8}$
861.10	$2.452\,55 \times 10^{-6}$	$7.606 \times 10^{-9}$	$2.170\,23 \times 10^{-8}$
888.90	$2.697\,84 \times 10^{-6}$	$9.616\,05 \times 10^{-9}$	$2.524\,76 \times 10^{-8}$
916.50	$2.957\,03 \times 10^{-6}$	$1.201\,08 \times 10^{-8}$	$2.913\,29 \times 10^{-8}$
943.80	$3.229\,22 \times 10^{-6}$	$1.293\,26 \times 10^{-8}$	$3.309\,11 \times 10^{-8}$
970.80	$3.514\,37 \times 10^{-6}$	$1.532\,46 \times 10^{-8}$	$3.825\,95 \times 10^{-8}$
997.60	$3.813\,53 \times 10^{-6}$	$1.326\,87 \times 10^{-8}$	$4.344 \times 10^{-8}$



## APPENDIX B: RESULTS

### B.1 HOURLY AVERAGES ENSEMBLE MEMBER ZERO AND ONE

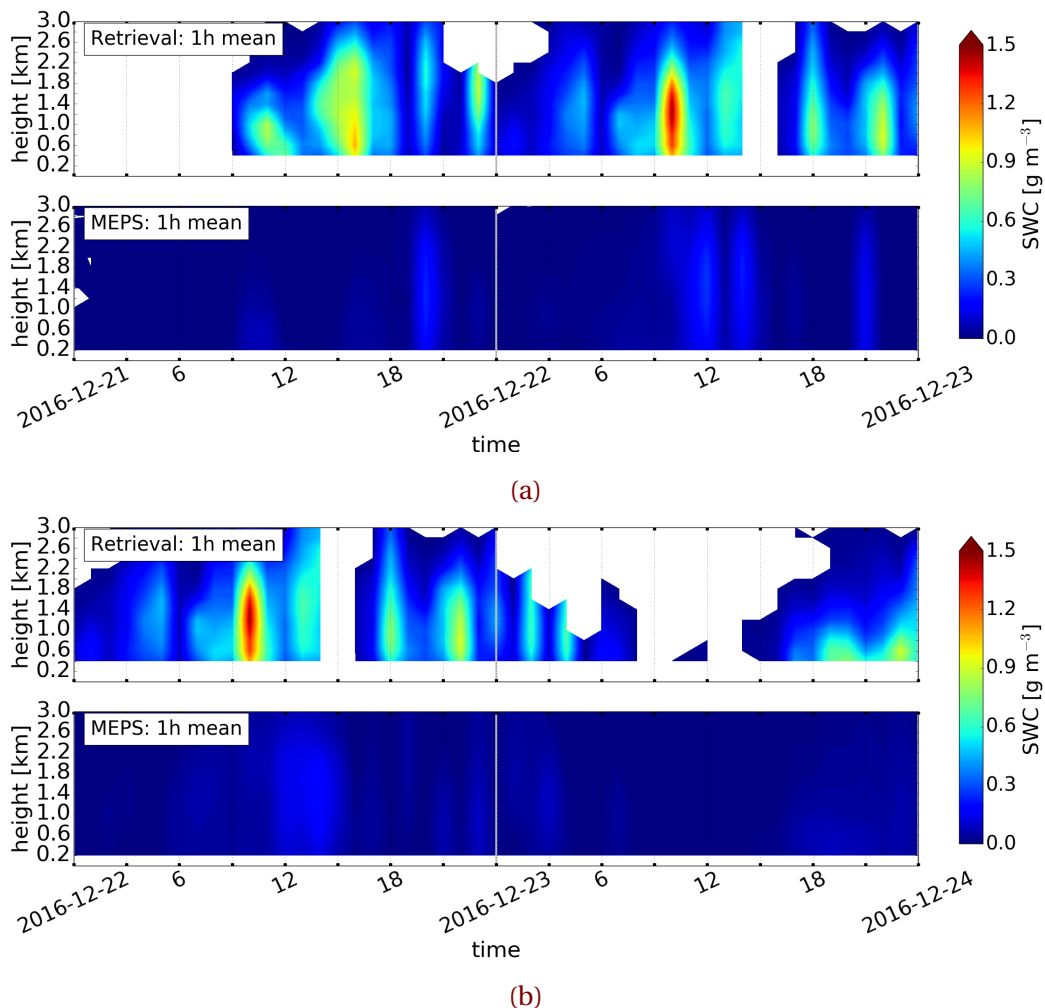
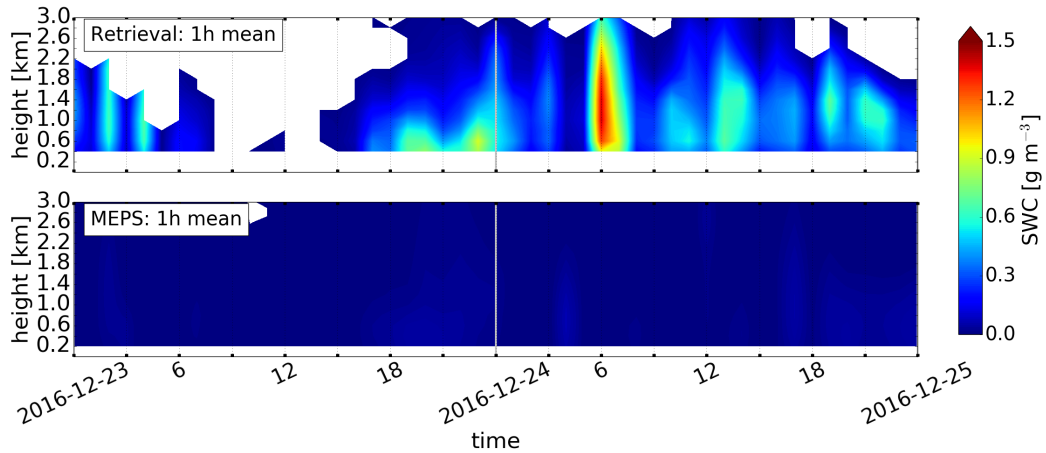
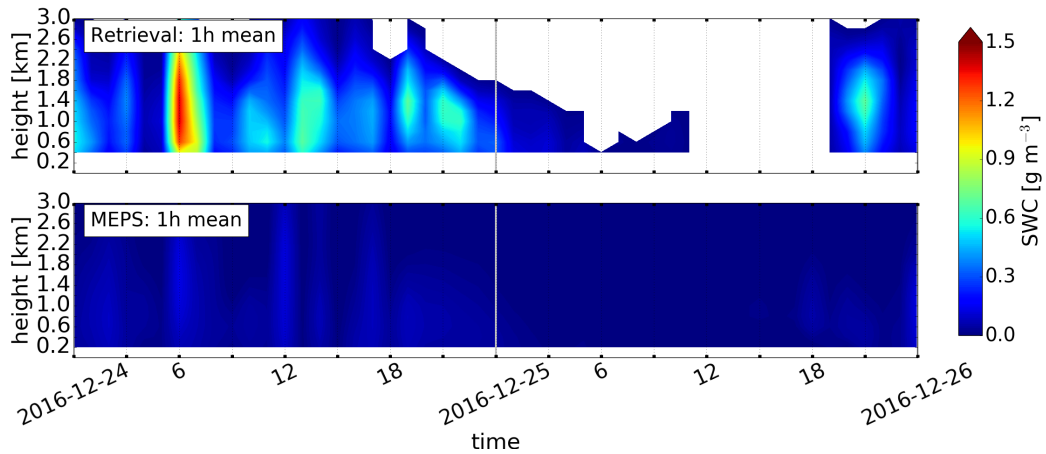


**Figure B.1.1:** Upper panel: hourly averaged retrieved SWC, lower panel instantaneous hourly averaged SWC forecast of deterministic and first ensemble member. Initialised 21 December 2016 and 22 December 2016 at 0 UTC.

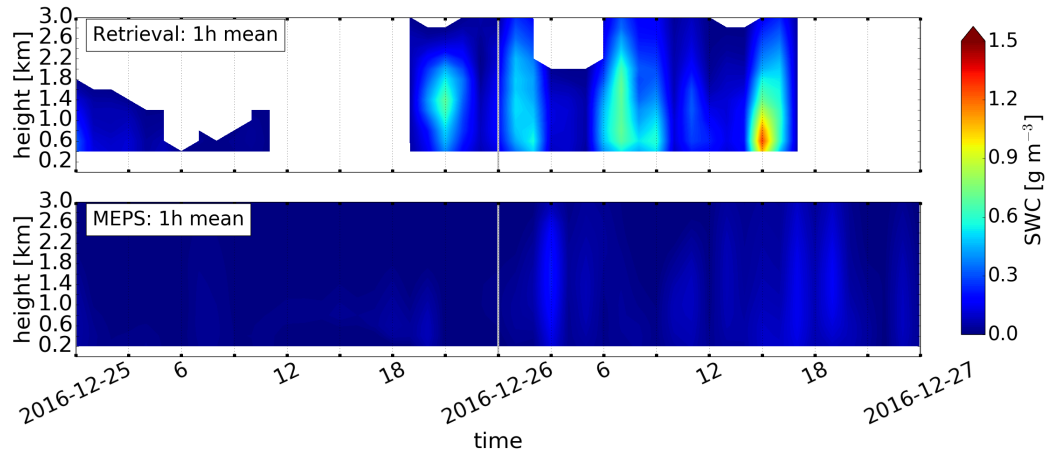


(c)

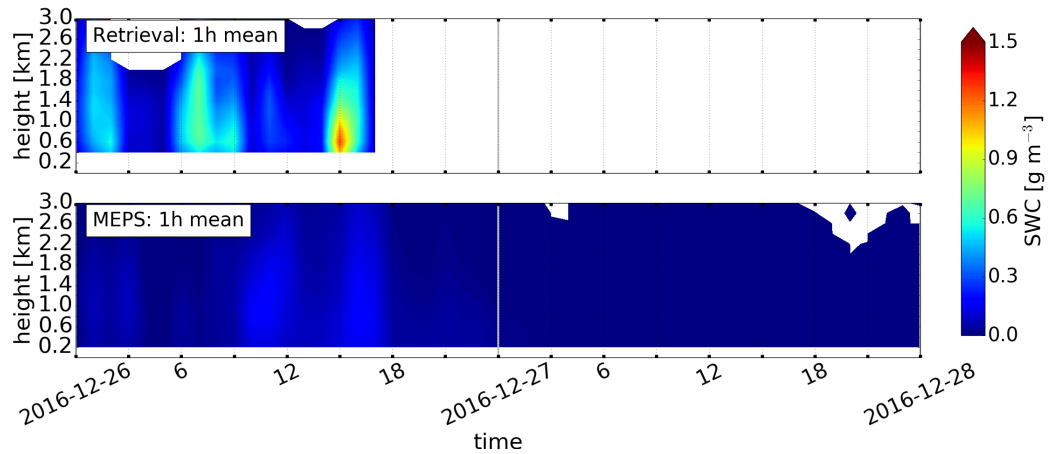


(d)

**Figure B.1.1:** (Continued from previous page.) Initialised 23 December 2016 and 24 December 2016 at 0 UTC.



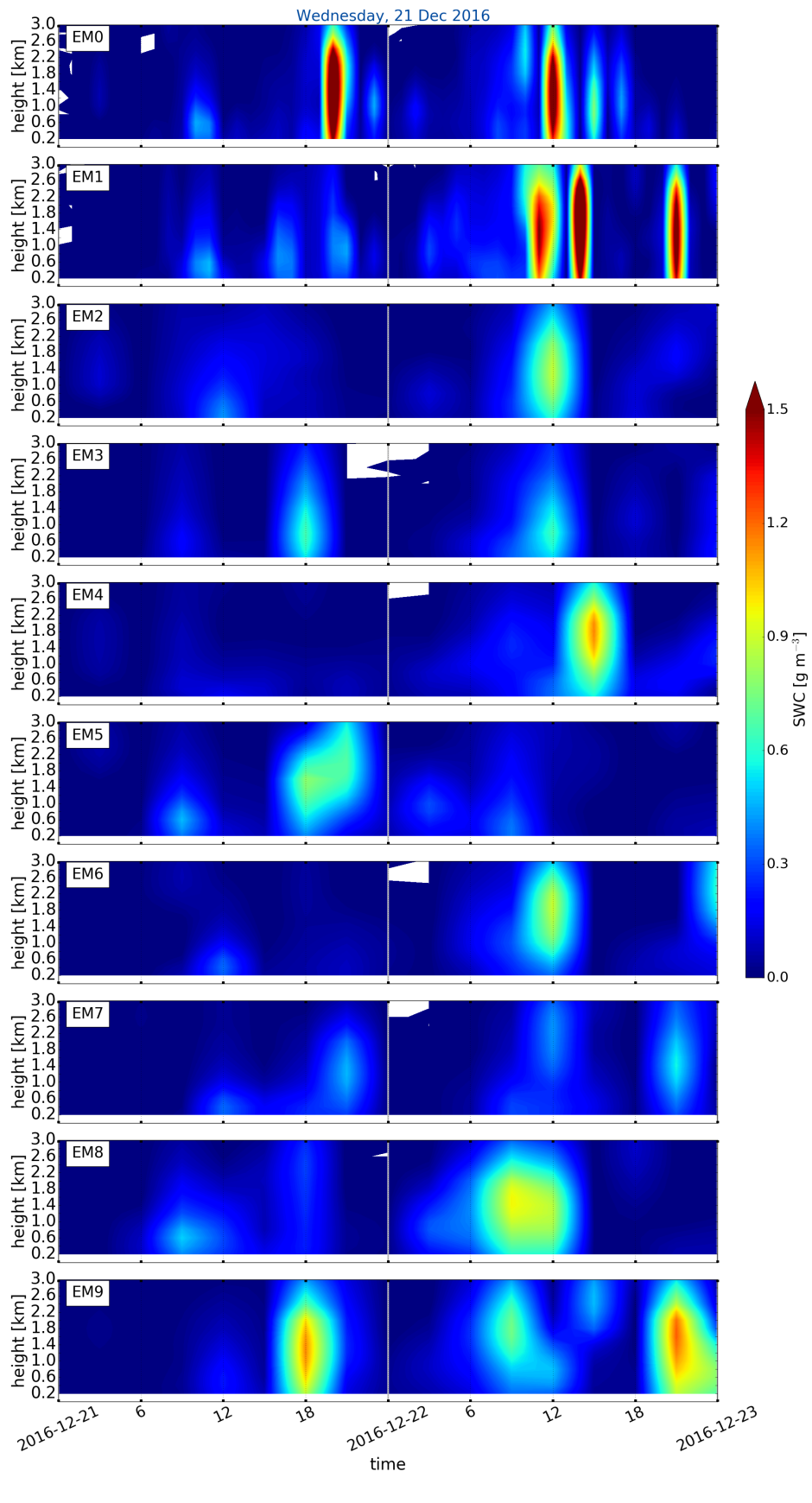
(e)



(f)

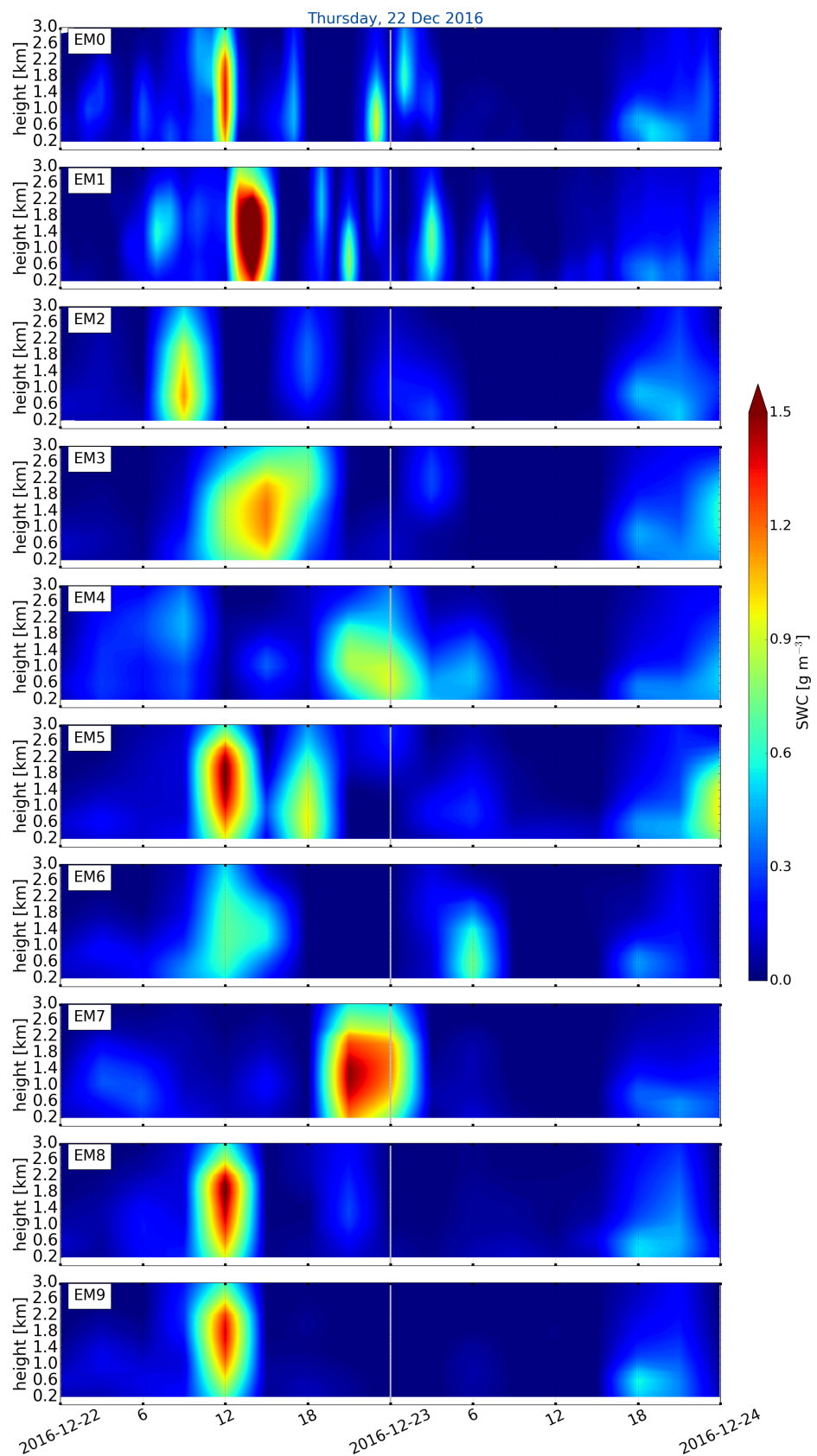
**Figure B.1.1:** (Continued from previous page.) Initialised 25 December 2016 and 26 December 2016 at 0 UTC.

## B.2 VERTICAL SWC - ALL ENSEMBLE MEMBER



(a)

**Figure B.2.1:** Vertical SWC of each individual ensemble member from 0 to 9 forecast for 48 h. Initialised 21 December 2016 at 0 UTC.



(b)

**Figure B.2.1:** (Continued from previous page.) Initialised 22 December 2016 at 0 UTC.

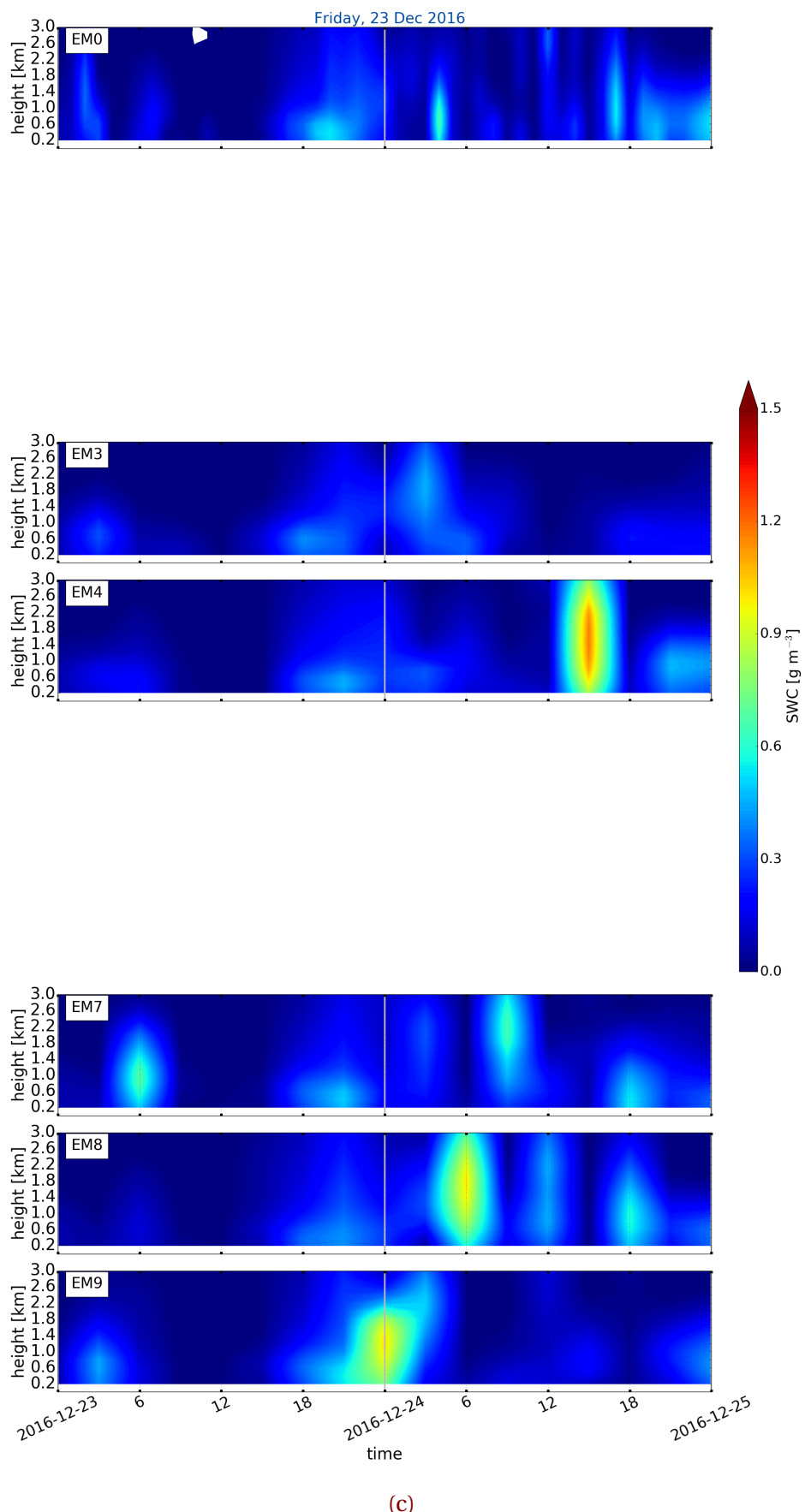
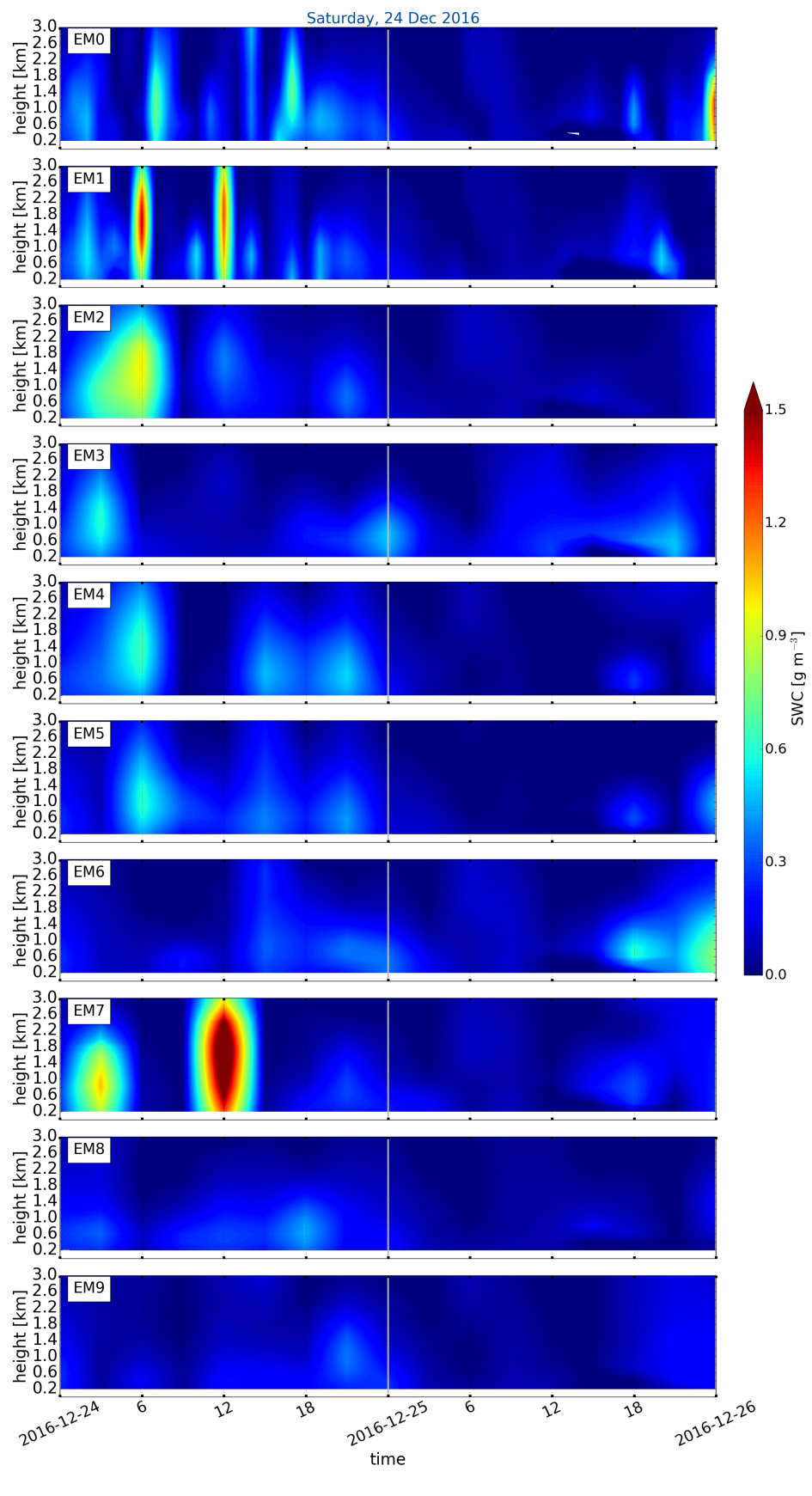


**Figure B.2.1:** (Continued from previous page.) Initialised 23 December 2016 at 0 UTC.



(d)

**Figure B.2.1:** (Continued from previous page.) Initialised 24 December 2016 at 0 UTC.

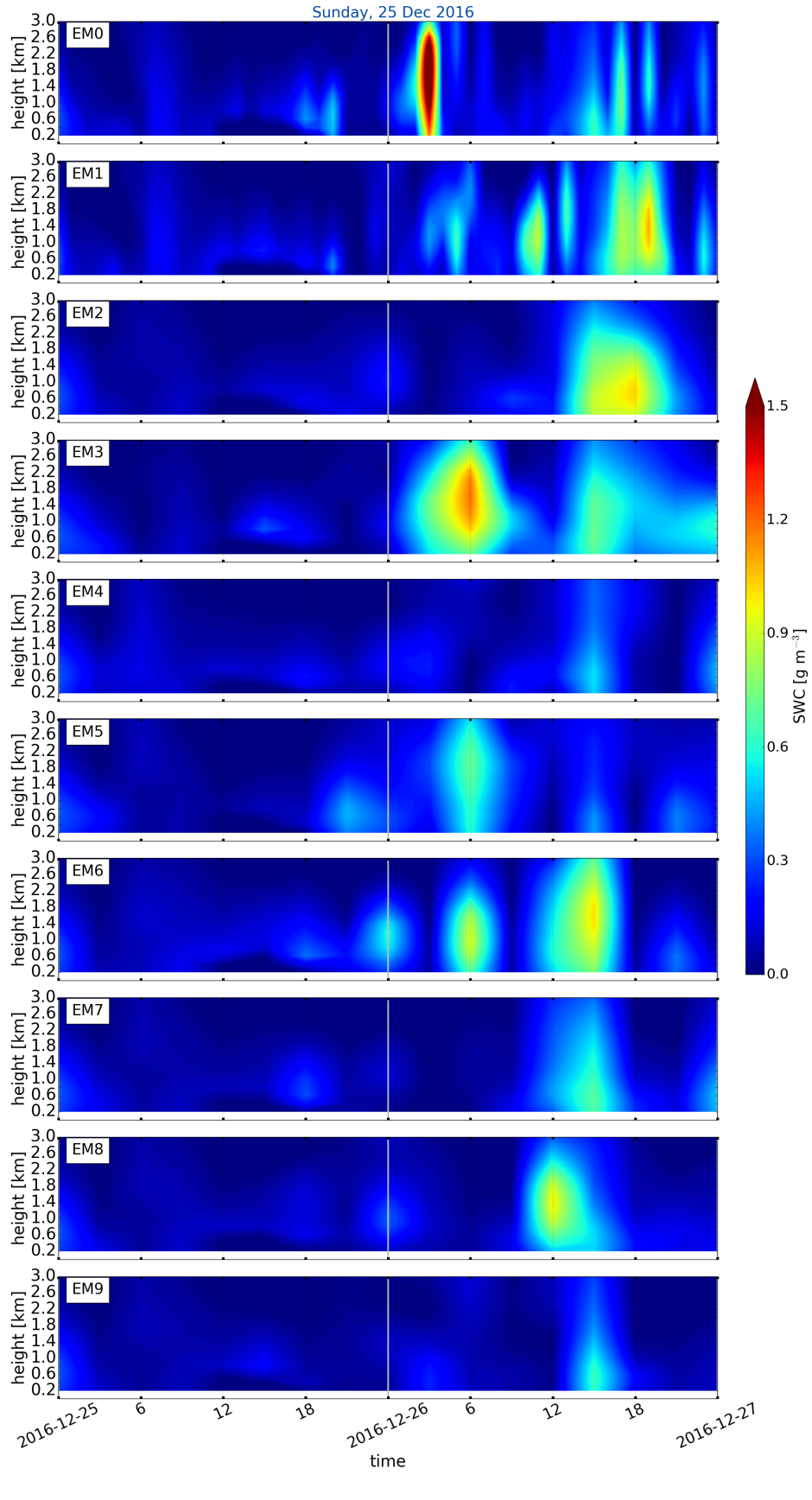
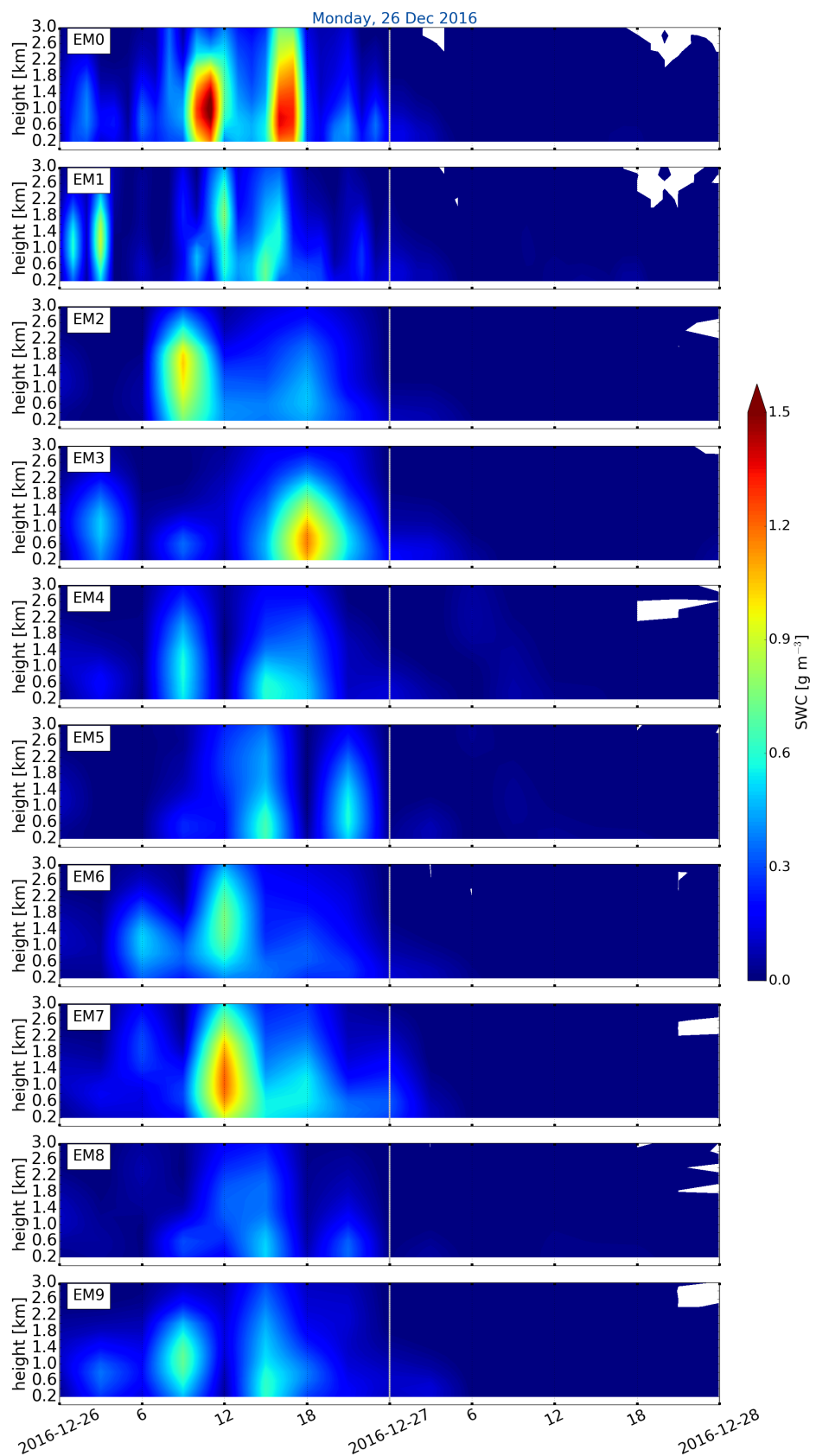


Figure B.2.1: (Continued from previous page.) Initialised 25 December 2016 at 0 UTC



(f)

**Figure B.2.1:** (Continued from previous page.) Initialised 26 December 2016 at 0 UTC.



## DECLARATION

I hereby declare that except where specific reference is made to the work of others, the contents of this thesis is made independently. I have explicitly marked all material which has been quoted either literally or by content from the used sources.

Furthermore, I certify that this research thesis or any part of it has not been previously submitted for a degree or any other qualification at the University of Oslo or any other institution in Norway or abroad.

Franziska Hellmuth

Oslo, June 2018